Adaptive Functional Magnetic Resonance Imaging

by
Seung-Schik Yoo

B.S., Biomedical Engineering, The Johns Hopkins University, 1994
M. of Business Administration, University of Massachusetts, Boston, 1999

Submitted to the Department of Nuclear Engineering and
Harvard-M.I.T. Division of Health Science and Technology
in Partial Fulfillment of the Requirements for the Degree of
Doctor of Philosophy in the field of Radiological Science

at the

MASSACHUSETTS INSTITUTE OF TECHNOLOGY

February, 2000

Author..
Department of Nuclear Engineering
Harvard-M.I.T. Division of Health Science and Technology
January, 25, 2000

Certified by...
Lawrence P. Panych
Assistant Professor of Radiology, Harvard Medical School
Thesis Supervisor

Certified by...
David G. Cory
Associate Professor of Nuclear Engineering
Thesis Reader

Accepted by...
Sow-Hsin Chen
Professor of Nuclear Engineering
Chairman, Department Committee on Graduate Students

Adaptive Functional Magnetic Resonance Imaging

by
Seung-Schik Yoo

Submitted to the Department of Nuclear Engineering and
Harvard-M.I.T. Division of Health Science and Technology
on January 27, 2000 in partial fulfillment of the
requirements for the degree of
Doctor of Philosophy in the field of Radiological Science

Abstract

Functional MRI (fMRI) detects the signal associated with neuronal activation, and has been widely used to map brain functions. Locations of neuronal activation are localized and distributed throughout the brain, however, conventional encoding methods based on k-space acquisition have limited spatial selectivity. To improve it, we propose an adaptive fMRI method using non-Fourier, spatially selective RF encoding. This method follows a strategy of zooming into the locations of activation by progressively eliminating the regions that do not show any apparent activation. In this thesis, the conceptual design and implementation of adaptive fMRI are pursued under the hypothesis that the method may provide a more efficient means to localize functional activities with increased spatial or temporal resolution.

The difference between functional detection and mapping is defined, and the multi-resolution approach for functional detection is examined using theoretical models simulating variations in both in-plane and through-plane resolution. We justify the multi-resolution approach experimentally using BOLD CNR as a quantitative measure and compare results to those obtained using theoretical models. We conclude that there is an optimal spatial resolution to obtain maximum detection; when the resolution matches the size of the functional activation.

We demonstrated on a conventional 1.5-Tesla system that RF encoding provides a simple means for monitoring irregularly distributed slices throughout the brain without encoding the whole volume. We also show the potential for increased signal-to-noise ratio with Hadamard encoding as well as reduction of the in-flow effect with unique design of excitation pulses.

RF encoding was further applied in the implementation of real-time adaptive fMRI method, where we can zoom into the user-defined regions interactively. In order to do so, real-time pulse prescription and data processing capabilities were combined with RF encoding. Our specific implementation consisted of five scan stages tailored to identify the volume of interest, and to increase temporal resolution (from 7.2 to 3.2 seconds) and spatial resolution (from 10 mm to 2.5-mm slice thickness). We successfully demonstrated the principle of the multi-resolution adaptive fMRI method in volunteers performing simple sensorimotor paradigms for simultaneous activation of primary motor as well as cerebellar areas.

Thesis Supervisor: Lawrence P. Panych
Title: Assistant Professor of Radiology, Harvard Medical School

Table of Contents

Chapter 4. Multi-resolution Detection of Functional Activation: Theoretical Examination

Chapter 5. Multi-resolution Detection of Functional Activation: Experimental Data

Chapter 6. Functional MRI using Spatially-selective RF encoding

Chapter 7. Real-time Adaptive Functional MRI

7.2 Materials and Methods

7.3 Results

Chapter 8. Discussions and Conclusions

Acknowledgements

I would like to take this opportunity to acknowledge my thesis supervisor, Professor Lawrence P. Panych, for his guidance and mentorship during my graduate study. I feel I am very lucky to have him as my advisor. I owe so much to him. His instruction helped me to become an endeavoring research scientist. I also thank his wife, Dr. Chandlee Dickey for her kind words and smile.

I extend my thanks to Dr. Guttmann. He has been a good friend, a mentor, and a keen critic on my thesis work. Without him, submitting this thesis would have been quite a difficult task. I would also like to thank Professor David Cory. He taught me about radiological sciences and was also a persistent supporter of my thesis and work. I really appreciate his help and advice. Professor Rosen, who paved the way for functional MRI, helped me to set my vision on functional MRI as well as advised me through HST program. Dr. Wible, an inspiring neuroscientist, helped to introduce me to the world of neuroscience. I was very fortunate to have them in the thesis committee.

Professor Jolesz always was a good supporter of my work, and I thank him for his supportive words. I also would like to thank Drs. Rivkin, Weiler, Mulkern, and Waber at Children's Hospital for their support. Dr. Rivkin especially allowed me to concentrate on writing my thesis at times when I was supposed to dedicate more time to his research. I should not fail to acknowledge Drs. Tung and Horowitz at Johns Hopkins Medical School, and Dr. Muller at FDA, who helped me to initiate my career in the field of medical research.

I acknowledge my colleagues, Drs. Saiviroonporn, Zhao, Cavanaugh, Kacher, Kyriakos, Zengingonul and Venkatesh at Brigham and Women's Hospital for their friendship and support. My graduate life would have been much less fun without them. In particular, Dr. Bernard, the director of the MIT nuclear reactor, pampered and guided me through the qualifying exam. My colleagues at MIT and HST, Drs. Justo, Tang, Ju, Liu, Sha and Seto are great scientists and fun-friends to be with. They were always supportive even though I was rarely on campus. Professor Yip, Zhou and Chen were always available for help and guidance. Ms. Gwinn, Egan at MIT and administrative staffs at Brigham, Ms.Valk, Roth, Holub and Kelly, were eager to help me with administrative problems. I will remember their help and appreciate it.

I would also like to dedicate this thesis to my late sister, Sung-Min, who, I believe, is watching over me. I also thank my sister, Sung-Hee, who motivated me to come to U.S. about 9 years ago, for her strong support. I owe everything else to my parents, Hyon-Joon Yoo and Yoo-Wan Sung. They nurtured me and supported me incessantly in all aspects of my life. I dare endeavor to be the greatest parents as they are. There are no words to describe how much I am thankful for their support. Last, but not least, I dedicate this thesis to my dearest wife, Seh-Eun, my daughter Jung-Yeon and my family-in-laws. Seh-Eun endured nine long months as a wife of a graduate student and as a mother-to-be while I had to concentrate on my thesis and research. Seh-Eun has helped and encouraged me to stay on course. I also thank all her family for their strong support.

Chapter 1
Introduction to Adaptive fMRI and Magnetic Resonance Imaging

1.1 Introduction

Functional magnetic resonance imaging (fMRI) was developed in the early 1990s capitalizing upon the ability to detect local changes in cerebral blood volume (CBV), cerebral blood flow (CBF) and oxygenation level during neuronal activation ([1]-[7]). It has since achieved a prominent place in methods for mapping brain function. Functional MRI enables non-invasive visualization of brain function, without resorting on the use of radioactive or exogenous contrast agents. With good temporal and spatial resolution, functional MRI has been used in numerous neuro-scientific studies including somatotopic cortical mapping ([8]-[10]) and the investigation of high-order cognitive processes such as working memory and decision making ([11]-[15]). Functional MRI has also had a direct impact on clinical applications. These include functional mapping of cortical areas for the planning of neurosurgery ([16]-[19]) as well as elucidating the neural difference of people with psychiatric /cognitive disorders such as schizophrenia and learning disability [20,21].

The most common and widely used method for eliciting functional signal is based on the detection of the blood oxygenation level dependent (BOLD) variation during neuronal activation using imaging sequences that are sensitive to the local changes in magnetic susceptibility. BOLD contrast in cortical tissue is small, typically on the order of between 1% and 6% at 1.5 Tesla [22]. In a typical fMRI experiment, multiple sets of images are acquired over the course of several control and stimulation periods and the small BOLD change due to activation is detected using statistical methods ([23]-[25]). In general, acquiring the data from the whole brain is important because the area of brain activation is not always known a priori, nor is it necessarily confined to a single slice of the imaging volume. In particular, high-order functional tasks involving multiple locations throughout the brain necessitate the acquisition of functional information from the whole brain. Accordingly, fMRI demands rapid acquisition of data often covering the whole brain volume and with a high signal-to-noise-ratio (SNR) to overcome the inherently low contrast.

In various situations, high spatial (sub-millimeter in-plane resolution and slice thickness of 5-7 mm) or temporal resolution (sub-second) has been used in data acquisition. For example, high-resolution characterization of somatotopic functions ([8]-[10]) as well as distinguishing adjacent, yet spatially-resolvable high-order cognitive areas [26] have been studied with sub-millimeter spatial resolution. High spatial resolution is also desirable in neurosurgical planning to distinguish the 'salvageable' eloquent areas of interest from a tumor or other targets of surgical intervention [16, 18, 19]. Sub-second temporal resolution has been necessary to study the event-related fMRI signal [6, 27, 28] and to model hemodynamic response during event-related tasks ([29]-[34]).

Previous fMRI studies conducted with high temporal or spatial resolution have been limited to a few selected locations. Such strategies involved repeated imaging of a single section [2, 7, 29, 31, 33, 34, 35] or a slab of regularly spaced sections [28, 31, 32, 36]. In choosing the volume of interest (VOI) for these studies, *a priori* decisions about the location of activation were made based on anatomic data acquired prior to the functional imaging session.

In order to achieve high spatial and/or temporal resolution in regions of functional activation, an 'adaptive' MRI method based on spatially selective radio frequency (RF) encoding is proposed. The goal of this thesis is to develop such an *adaptive fMRI* method using RF encoding. The basic idea of the adaptive approach in fMRI is that the regions of activation, however they are distributed throughout the brain, can be selectively detected dynamically in multiple stages at progressively higher resolution, ignoring quiescent regions and "zooming" only into the regions of activation. This thesis draws mainly on previous work in the development of non-Fourier based adaptive approaches by Panych *et al.* [40] and applies these approaches for fMRI.

Adapting data acquisition protocols based on prior knowledge has been applied previously to optimize k-space acquisition for functional and other experiments. These include among other methods the key-hole and RIGR (Reduced-encoding Imaging with Generalized-series Reconstruction) techniques [37,38]. In the key-hole method, a full set of k-space data is first acquired, and then, only the lower frequency portion of the dynamic data is updated [37]. In RIGR, dynamic images are obtained by combining a reduced set of dynamic data with a priori high-resolution data via a novel constrained image reconstruction algorithm [38]. Other adaptive approaches also have been investigated using the Karhunen-Loeve decomposition [39]. These Fourier-based methods do not provide the spatial selectivity necessary if one wants to dynamically encode localized brain locations in any encoding basis other than the Fourier basis. Non-Fourier based wavelet-encoding [40] and encoding by singular value decomposition (SVD) [41] were proposed to provide the flexibility necessary for adaptive methods. These methods use RF encoding which features spatial selectivity and one is not limited to acquiring data in k-space. An important feature of RF encoding is that non-Fourier basis functions generated by RF encoding can be updated dynamically, adapting to changes in the field-of-view.

A development of the concept and implementation of *adaptive fMRI* with RF encoding suggests the following advantages. One advantage is that adaptive imaging may provide a more efficient method of localization of brain activity in fMRI studies by increasing the temporal or spatial resolution of fMRI data. For example, by encoding with spatially selective excitation applied in the through-plane direction, areas of functional activation can be selectively resolved by applying a multi-staged adaptive algorithm that eliminates slices where no activation is evident. Therefore, in later imaging stages, in-plane resolution or temporal resolution could be increased in the remaining slices. Another advantage of the adaptive approach using spatially-selective encoding is that signal-to-noise ratio may be improved over the conventional multi-slice method by appropriate choice of encoding such as Hadamard encoding.

The main contribution of the thesis is that the non-Fourier adaptive approach was implemented and applied for the first time in functional MRI. Hadamard encoding to increase the SNR was also implemented for the first use in functional MR. This thesis also provides the first systematic justification and optimization of the multi-resolution approach in functional MRI. We believe that variations of the method can potentially be used for other applications such as contrast detection and bolus tracking. In addition to the main contributions of the thesis, an inflow-reducing method, incorporated with the RF encoding scheme, was implemented and shown to be effective.

This thesis consists of eight chapters. Chapter 1 contains a brief introduction to MRI, including an overview of common encoding techniques in MRI. In Chapter 2, the fundamentals of functional MRI will be addressed in terms of its physiological basis, functional contrast generation, and experimental methods. The basics of RF encoding are presented in Chapter 3. The limitations and justification of the adaptive multi-resolution zooming approach in terms of functional detection will be addressed theoretically in Chapter 4. An experimental examination of the multi-resolution approach is included in Chapter 5. RF encoding applied to functional MRI is presented in Chapter 6. Chapter 7 describes an implementation of real-time adaptive fMRI. The last chapter discusses important findings from theoretical studies and experimental sessions, and summarizes some directions for future work.

1.2 Magnetic Resonance Imaging

1.2.1 Physics of NMR: The Signal Source

When a material containing nuclei with a net magnetic moment is placed in a magnetic field, interaction with the magnetic field results in splitting of nuclear spin states and their associated energy states. This interaction is referred to as the Zeeman interaction. For a nucleus with spin quantum number I, there are $(2I+1)$ different possible nuclear spin states when exposed the magnetic field (B_o in Fig. 1.1). As illustrated in Fig. 1.1, for a spin 1/2 nucleus (when I=1/2) such as ${}^1_1H$, I_z takes the value of -1/2 (spin up) or +1/2 (spin down). In this case, the energy created by the Zeeman interaction (ΔE) is given by;

$$\Delta E = \gamma \hbar B_o, \tag{1.1}$$

where $\hbar$ is Plank's constant ($h/2\pi$), and γ is the gyro-magnetic ratio that relates the magnetic moment of the nucleus to its angular momentum. (For example, γ of ${}^1_1H$ is equal to 42.58 MHz/Tesla).

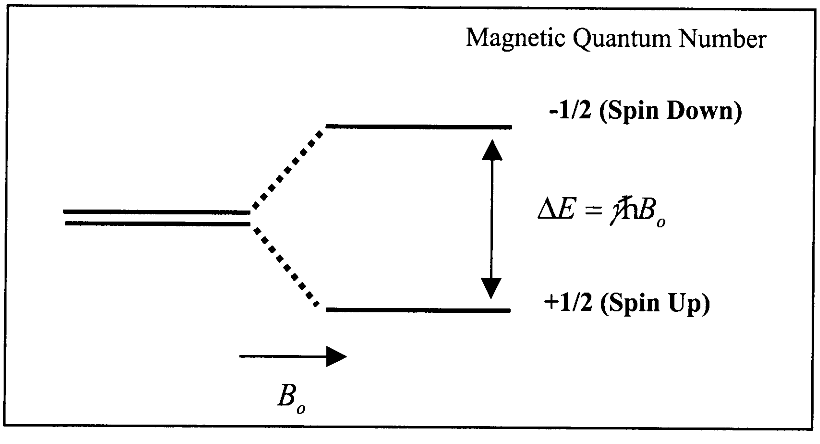

Figure 1.1 Schematic illustration of Zeeman interaction for a spin 1/2 nucleus (I=1/2) with an external magnetic field, B_o. The magnetic moment can have two states (i.e. 1/2 and -1/2), and the energy difference between them is $\Delta E = \gamma \hbar B_o$.

The resonance frequency, ω_o, due to the Zeeman interaction is known as the Larmor frequency, and is equal to the product of the magnetic field B_o and the gyro-magnetic ratio γ;

$$\omega_o = \Delta E / \hbar = \gamma \hbar B_o / \hbar = \gamma B_o . \qquad (1.2)$$

From Eq. 1.2, and given the gyro-magnetic ratio, $\gamma / 2\pi = 42.58 MHz / Tesla$, the resonance frequency for ${}^1_1H$ at 1.5T is in the radiofrequency range.

The ratio of populations of down and up-spin states is determined by thermal interactions with surrounding lattice, and is derived from Boltzmann's equation as follows [42].

$$\frac{n_{down}}{n_{up}} = e^{-\Delta E / kT} , \qquad (1.3)$$

where k is Boltzmann's constant (1.38 x 10^{-23} J/K) and T is temperature. From Eq. 1.3, at normal room temperature, the ratio is close to 10^{-6}.

1.2.2 MR Signal: Excitation, Precession, and Relaxation

Strictly speaking, the theoretical framework to explain the NMR phenomena involves quantum statistical mechanics, however, for simple behavior, the quantum mechanical description of nuclear resonance can be replaced by classical equations governing the procession of a magnetization vector interacting with static and time-variant magnetic fields [113]. The bulk magnetization in a volume of material, due to the Zeeman interaction, can be modeled as a magnetization vector $\overrightarrow{M}$. $\overrightarrow{M}$ represents a magnetic moment that experiences a torque ($\vec{\Gamma}$) from any external magnetic field $\vec{B}$, as is described by Eq. 1.4, and illustrated in Fig. 1.2.

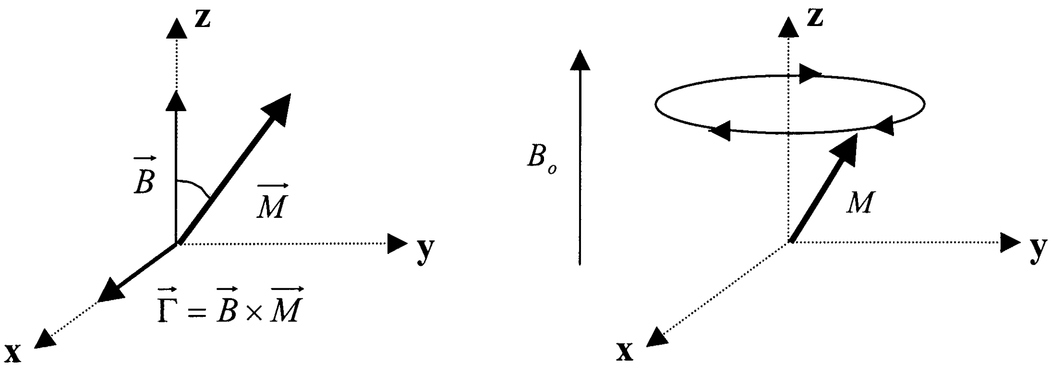

Figure 1.2 A schematic representation showing the direction of torque when the magnetization vector $\vec{M}$ is in an external magnetic field $\vec{B}$ (left). The torque experienced will cause a clockwise movement of $\vec{M}$, rotating at the Larmor frequency, ω_o.

$$\vec{\Gamma} = \vec{M} \times \vec{B} \tag{1.4}$$

Under torque, the magnetic moment $\vec{M}$ rotates at an angular rate defined by the gyro-magnetic ratio as described by Eq. 1.5;

$$\frac{d\vec{M}(t)}{dt} = \gamma \cdot \vec{\Gamma}(t). \tag{1.5}$$

Combining Eq. 1.4 with Eq. 1.5, the time-varying behavior of the magnetic moment $\vec{M}$ between external field $\vec{B}(t)$ and $\vec{M}(t)$ is represented as;

$$\frac{d\vec{M}(t)}{dt} = \gamma \cdot \vec{M}(t) \times \vec{B}(t). \tag{1.6}$$

Equation 1.6 is solved, assuming the initial condition of $\vec{M}$ being tipped away from the direction of $\vec{B}$ by the angle α. The solution is given by Eq. 1.7. The magnetization vector $\vec{M}(t)$, where $\vec{M} = (M_x, M_y, M_z)$, can be represented by both a longitudinal component along the z axis, $M_z(t)$, and a transverse component rotating in the *xy* plane, $M_{xy}(t)$, where $M_{xy}(t) = M_x(t) + iM_y(t)$. M_o represents the equilibrium magnitude of the magnetization vector.

$$M_x(t) = M_o \sin\alpha \cos(\omega_o t + \phi),$$
$$M_y(t) = M_o \sin\alpha \sin(\omega_o t + \phi), \qquad (1.7)$$
$$M_z(t) = M_o \cos\alpha.$$

Let us define a frame of reference where the x and y axes rotate at the Larmor frequency around the z axis. In this rotating frame of reference, when the magnetization vector, $\vec{M}$, placed in a radio-frequency (RF) magnetic field at the Larmor frequency perpendicular to the z axis, $\vec{M}$ is rotated away from the z axis according to Eq. 1.6. This process is called 'excitation' or 'nutation'. Figure 1.3 illustrates the process. If the magnetic field, $\vec{B_1}$, is oriented as shown, $\vec{M}$ rotates about $\vec{B_1}$ in the clockwise direction. The angle of rotation α, is called the nutation flip angle, and is equal to $\alpha = -\gamma\|\vec{B_1}\|\Delta t_{rf}$ for a constant magnitude of $\vec{B_1}$ and time duration of the RF excitation, Δt_{rf}.

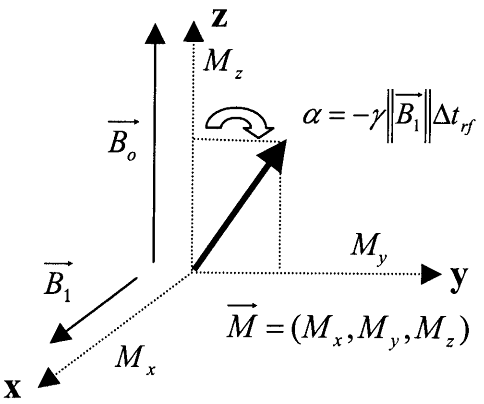

Figure 1.3 A schematic drawing of the process of excitation in the rotating frame of reference by the RF pulse represented by $\vec{B_1}$. The flip angle, α, is a function of strength and duration of the RF pulse.

In equilibrium, $\vec{M}$ is parallel to the direction of the static magnetic field $\vec{B_o}$. When perturbed from their equilibrium position, the magnetization vectors in a sample will eventually relax to the initial unexcited states if there is no additional excitation. There are two distinct types of relaxation. One is the rate at which nuclei exchange energy with the surrounding lattice (Spin-Lattice Relaxation). The other type of relaxation is a loss of phase coherence (Spin-Spin Relaxation). The constants describing the spin-lattice relaxation and spin-spin relaxation processes are referred as T_1 and T_2 respectively.

The process of excitation and relaxation of the magnetization vector can be summarized by the Bloch equation obtained by adding a relaxation factor to Eq. 1.6 ;

$$\frac{d\overrightarrow{M}(t)}{dt} = \gamma \cdot \overrightarrow{M}(t) \times \vec{B}(t) - \Re\{\overrightarrow{M}(t) - \overrightarrow{M}_o\}. \tag{1.8}$$

$\vec{B}(t)$ in (1.8) accounts for both the static and the RF fields ($\vec{B}(t) = \vec{B}_o + \vec{B}_1(t)$) and $\Re$ is a relaxation matrix incorporating the T_1 and T_2 time constants;

$$\Re = \begin{bmatrix} 1/T_2 & 0 & 0 \\ 0 & 1/T_2 & 0 \\ 0 & 0 & 1/T_1 \end{bmatrix}. \tag{1.9}$$

The rotating magnetization vector induces current in a coil tuned to the Larmor frequency of the specific nuclei. The detected signal magnitude is proportional to the magnitude of the transverse magnetization vector because the coil is oriented to detect the changes in transverse magnetization. The aggregates of freely precessing magnetization vectors induce a time-dependent signal referred to as the free-induction-decay (FID). The amplitude of the FID decreases over time due to loss in signal coherence. The envelope of the FID in a perfectly uniform magnetic field is represented by the decay constant T_2. The inhomogeneous nature of the physical magnetic field due to imperfection in the main magnet field or other variations resulting from susceptibility-effects due to the local field inhomogeneity [42], causes additional loss in coherence. The relaxation constant including these effects is T_2*.

1.2.3 Imaging and Encoding

In order to obtain a spatial mapping of the signal sources in the sample volume after excitation, magnetic field gradients are applied to produce linear changes in the static magnetic field across the sample. Typically these linear gradients (units of Gauss/cm) are applied to the three orthogonal directions, and each coil can be energized individually or in combination so that a magnetic field gradient can be created along any arbitrary direction. With these gradients, the local Larmor frequency, $\vec{\omega}(\vec{r})$, is given a slight offset that is proportional to the spatial location $\vec{r}$;

$$\vec{\omega}(\vec{r}) = -\gamma(\overrightarrow{B_o} + \vec{G}\cdot\vec{r}), \qquad (1.10)$$

where $\vec{r} = (x, y, z)$ and $\vec{G} = (G_x, G_y, G_z)$.

Equation 1.10 implies that when a gradient is applied, the spatial location along a line of the signal sources can be determined from the frequency. The next sections describe how these gradients are used in conjunction with RF excitation to encode images. We will use the example of a simple gradient echo MR sequence.

Slice Selection

If a gradient is applied in a given direction to produce a linear variation in the Larmor frequency (Fig. 1.4), and the sample is simultaneously irradiated with an RF pulse that has a finite bandwidth ($\Delta\omega$ in Fig. 1.4), the only excited spins will be within a single 'slab' or 'slice' of $\Delta Z = \Delta\omega / \gamma G_z$ that is perpendicular to that direction. Changing the carrier frequency varies the location of the slice profile whereas changing the duration of the RF pulse or the amplitude of the slice-select gradient changes the slice thickness. Time-varying gradient and RF pulses can be used to produce specialized excitation profiles for slice or volume selection [43].

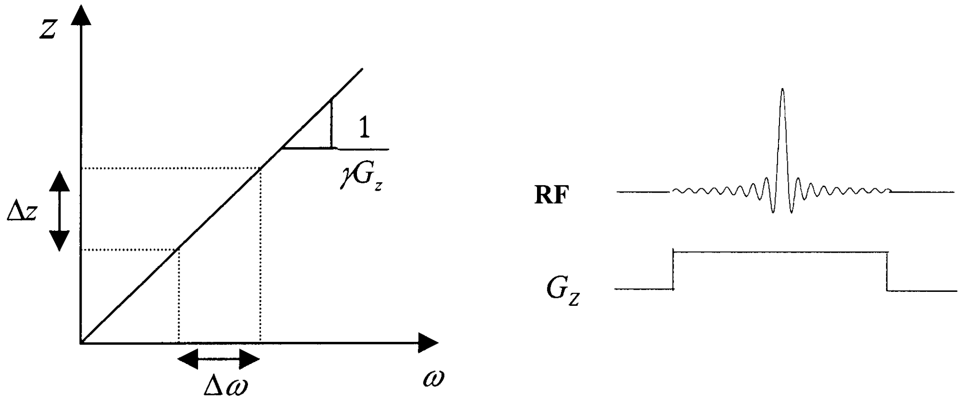

Figure 1.4 Illustration of the mapping of a finite bandwidth RF pulse $(\Delta\omega)$ to the corresponding spatial width (Δz) of spins that are excited when applying a linear gradient G_z.

Frequency Encoding

After a slab of volume in the sample is excited, assuming a homogeneous field, all magnetization vectors in the slice will initially resonate at the same frequency. We define a signal density function within the excited sample as $\rho(x,y)$ and assume a magnetic field gradient in the x direction ($G_x = \partial B_z / \partial x$). Let us model the signal from a small volume at location $x = x_o$ and $y = y_o$ as $\rho(x_0, y_0)e^{-i\gamma G_x x_o t}$. The complex exponential term $e^{-i\gamma G_x x_o t}$ accounts for the precession due to the magnetic gradient G_x at location x_o. The signal $s(t)$ detected (in the rotating frame of reference) from the whole volume is,

$$s(t) \propto \iint \rho(x,y)e^{-i\gamma G_x x t}dxdy\,. \tag{1.11}$$

Equation 1.11 implies that the detected signal is proportional to the sum of signal from "columns" of material perpendicular to the x axis, and that each column resonates at a frequency proportional to its position in x, *i.e.,* $\gamma G_x x$. Defining $k = \gamma G_x t$, an inverse Fourier-transform on $s(k)$ produces a function that is proportional to the projection of $\rho(x,y)$ along the x axis. Since the encoding utilizes the frequency for spatial indexing, it is usually referred to as "frequency encoding".

Phase Encoding

The time domain signal $s(t)$ in Eq. 1.11 can be used to obtain one-dimensional spatial information (x direction only) about the sample. An additional encoding method is necessary to provide a 2-dimensional representation of the sample. In order to achieve two-dimensional encoding, a magnetic gradient in the y direction ($G_y = \partial B_z / \partial y$) is applied to modulate the phase of the excited sample $\rho(x, y)$ on multiple excitations while the frequency-encoding gradient is turned on. In order to resolve M elements in the y-direction, M "phase-encoding" steps are applied with increments of ΔG_y made to the gradient amplitude on each step.

On each excitation, a phase encoding gradient is applied with the duration of τ to create a phase offset across the volume (Fig. 1.5). Following application of the phase encoding gradient, N sets of frequency-encoded signals are obtained. For each RF excitation, a different phase encoding gradient amplitude in increments of ΔG_y is applied, and on each of these phase encoding steps, N samples are acquired during a "readout" time at increments of ΔT (Fig. 1.6). The discrete set of sampled signal values $S(n, m)$ is represented as in Eq. 1.12.

$$S(n,m) \propto \iint \rho(x,y) e^{-i\gamma(n\Delta T G_x x + m\tau\Delta G_y y)} dxdy\,, \tag{1.12}$$

where $(-N/2+1) \le n \le N/2$, and $(-M/2+1) \le m \le M/2$.

Substituting $\begin{matrix} k_x = \gamma n \Delta T G_x \\ k_y = \gamma m\, \tau \Delta G_y \end{matrix}$ in Eq. 1.12 and rearranging,

$$S(k_x, k_y) \propto \iint \rho(x,y) e^{-i\gamma(k_x x + k_y y)} dxdy\ . \tag{1.13}$$

$S(k_x, k_y)$ represents a sampling of the Fourier space of $\rho(x,y)$. Therefore, from a two-dimensional inverse Fourier-transform on $S(k_x, k_y)$, we can obtain a discrete estimate or 'image' of $\rho(x,y)$. Here, k_x and k_y are the spatial frequencies (cm^{-1}), and $S(k_x, k_y)$ is referred to as the k-space representation of $\rho(x,y)$. Figure 1.5 illustrates the process of slice selection, frequency and phase encoding.

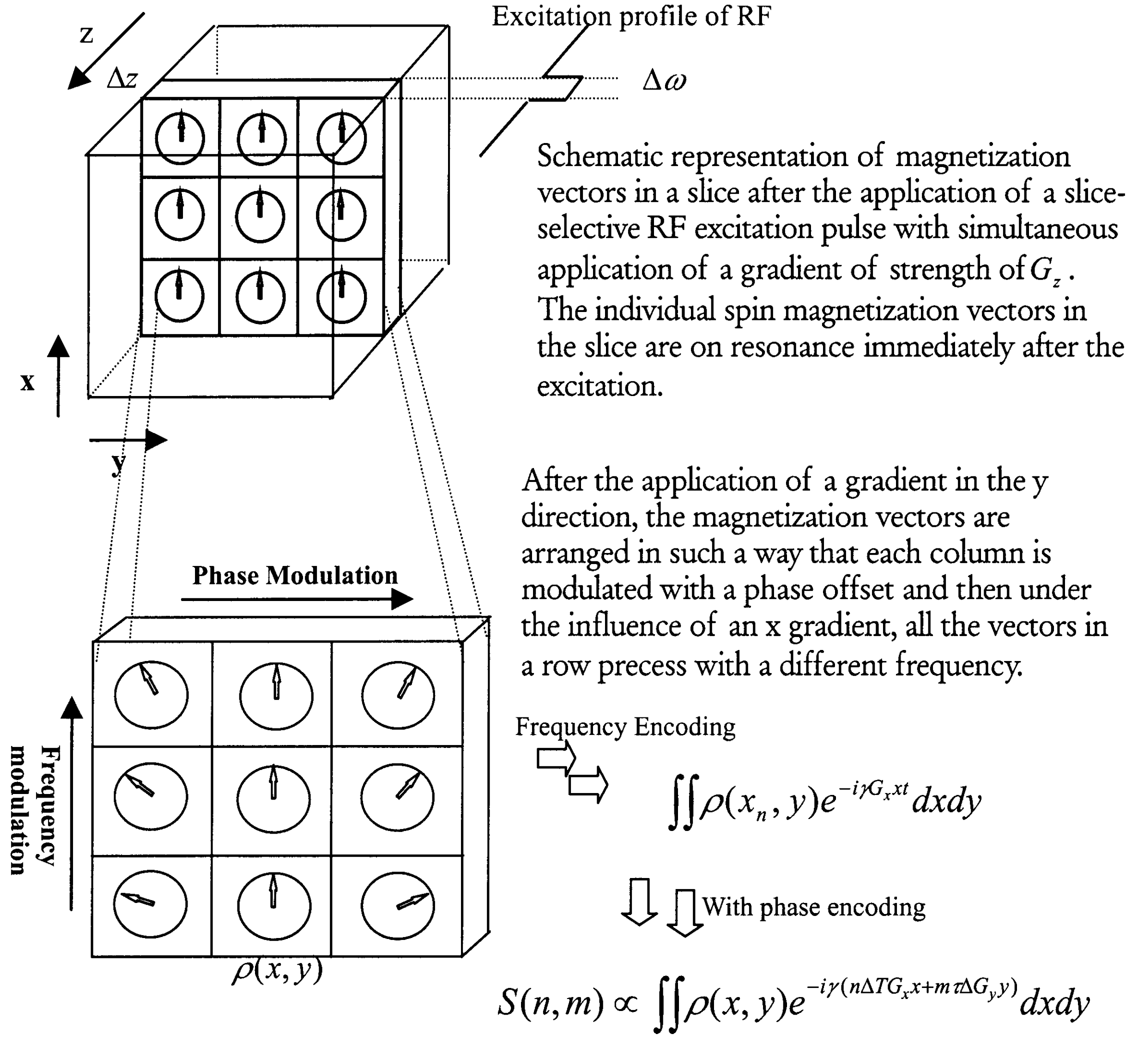

Schematic representation of magnetization vectors in a slice after the application of a slice-selective RF excitation pulse with simultaneous application of a gradient of strength of G_z. The individual spin magnetization vectors in the slice are on resonance immediately after the excitation.

After the application of a gradient in the y direction, the magnetization vectors are arranged in such a way that each column is modulated with a phase offset and then under the influence of an x gradient, all the vectors in a row precess with a different frequency.

$$\iint \rho(x_n, y) e^{-i\gamma G_x x t} dxdy$$

$$S(n,m) \propto \iint \rho(x,y) e^{-i\gamma(n\Delta T G_x x + m\tau\Delta G_y y)} dxdy$$

Figure 1.5 Illustration of the effect of slice selection and frequency/phase encoding to individual magnetization vectors in a sample.

Examples of MR Imaging Sequences

As described in the previous sections, typical MR encoding consists of slice selection followed by phase encoding and frequency encoding. Figure 1.6 shows a schematic timing diagram for a 2D gradient-echo pulse sequence. In this example, the slice selective RF pulse irradiates the sample while a slice-selective gradient (G_z) is applied (from t_a to t_b). Following this, a phase rewinder (negative z gradient) is applied to restore a uniform phase distribution across the selected slice (from t_b to t_c). During the same period, a phase-encoding gradient is applied to give different phase values to the spins at different locations along the y-direction. The phase encoding gradient is varied with increments of ΔG_y after each RF excitation. During the data acquisition period (DAQ from t_d to t_f in Fig. 1.6), G_x is applied to produce a linear variation of frequency along the x-direction. The signal, centered at t_e, is sampled in intervals of ΔT. The magnetization vectors are all in phase at t_e assuming there is no inhomogeneity in the magnetic field. The time interval between the center of the RF pulse and the center of the echo is called the echo time or TE, and the time interval between applications of each RF pulse excitation is called the repetition time or TR.

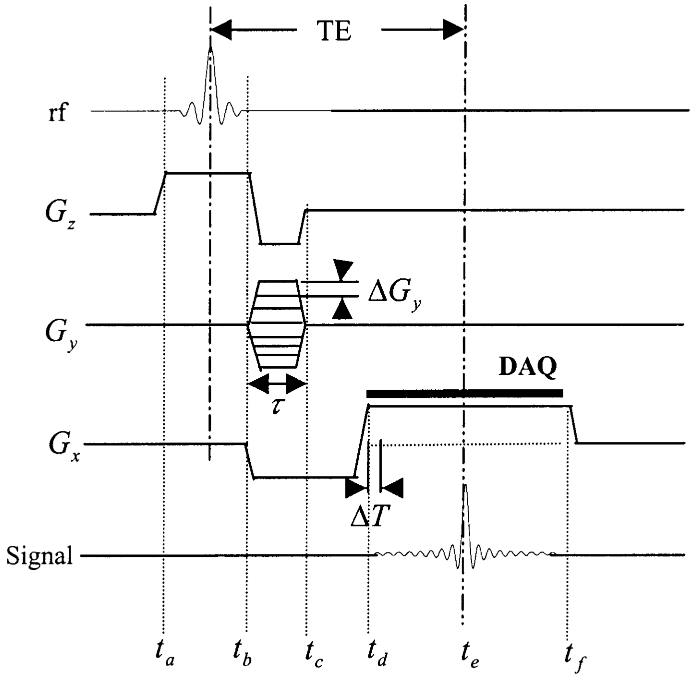

Figure 1.6 Schematic timing diagram of a simple Fourier encoding sequence. The method uses a RF pulse to select the slice in the z direction with G_z. A phase encoding gradient is applied after each RF excitation with the increment of ΔG_y for the duration of τ. The MR signal is sampled while a frequency encoding gradient is applied with sampling every ΔT.

Echo planar imaging (EPI), first proposed by Mansfield [44] and used widely in fMRI, allows for encoding 2 dimensional image data after a single RF excitation. Figure 1.7 shows a schematic timing diagram for a 2D gradient-echo EPI pulse sequence. First a slice is selected with slice-select gradient and RF pulse (from t_a to t_b) followed by a phase-rewinder (from t_b to t_c). After the slice selection, an oscillating gradient G_x and a phase-encoding gradient (G_y) with constant magnitude are applied.

Figure 1.8 illustrates a representation of the filling of k-space by the EPI sequence in Fig. 1.7. The area under the oscillating G_x and a constant G_y determine the location of sampling -points k_x and k_y respectively (see Eq. 1.13). In the interval between t_c and t_d, k_x is increased to its maximum. At time t_e, the area under the G_x waveform is zero, and therefore $k_x = 0$. At $k_x = 0$, a gradient echo is formed since the spins have maximum phase coherence with respect to action of G_x. With application of a negative value of G_x, k_x reaches the minimum. G_x is increased again and at $k_x = 0$, another echo is generated at time t_f. Since a constant magnitude of G_y is applied, k_y increases with equal proportion. The effect of the oscillating G_x is the generation of gradient echoes in alternating gradient reversal periods, τ_o (where τ_o is equal to the time interval between t_e and t_f). EPI with ultra-fast gradient switching, due mainly to its ability to encode a slice with a single RF excitation, is widely used for functional MRI.

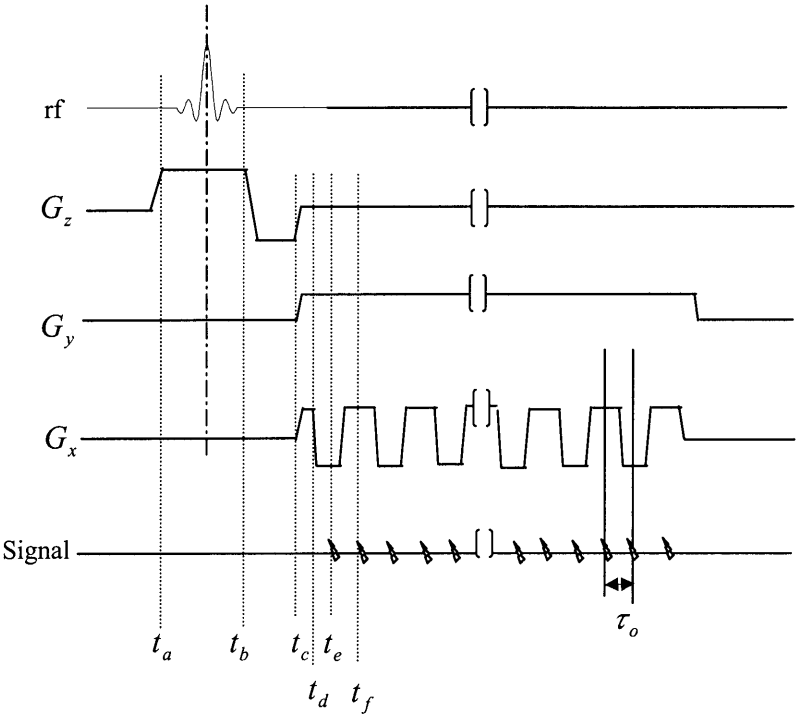

Figure 1.7 Schematic timing diagram of gradient-echo planar imaging (EPI) sequence. The method uses a RF pulse to select a slice in the z direction with G_z. A gradient G_x is oscillated after a single RF excitation and a constant phase encoding gradient G_y is applied. The MR signal sampled fills the entire 2D k-space of a slice.

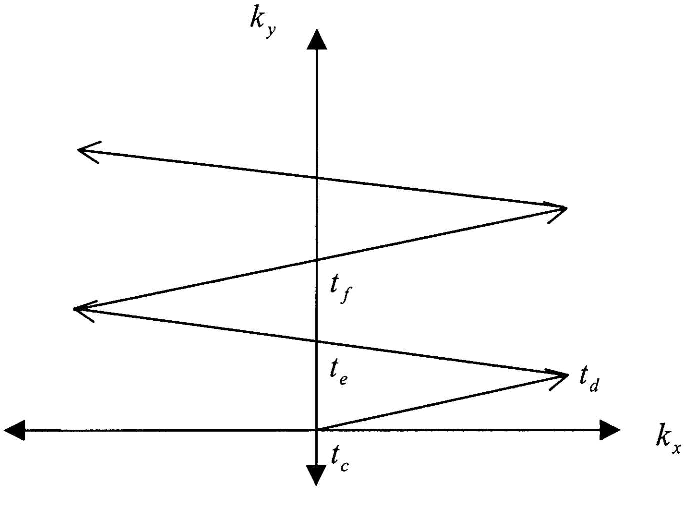

Figure 1.8 Representation of filling of k-space by the EPI sequence shown in Fig. 1.7.

1.2.4 MR Signal and Contrast

MR Signal

The magnitude of the MR signal is dependent upon multiple factors such as the choice of TE, TR, and flip angle as well as the relaxation constants, T_1, T_2 and T_2* of the sample. Let us represent the longitudinal magnetization at time n as M_z^n (see Fig. 1.9). The magnetization before and after the RF excitation are M_Z^{n-} and M_Z^{n+} respectively.

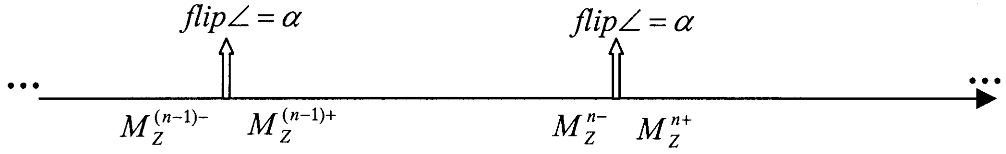

Figure 1.9 The longitudinal magnetization vector times before and after each excitation (arrow) of flip angle α.

M_Z^{n-} can be derived from the Bloch equation such that [42];

$$M_Z^{n-} = M_o(1-e^{\frac{-TR}{T1}}) + M_Z^{(n-1)+}e^{\frac{-TR}{T1}} = M_o(1-e^{\frac{-TR}{T1}}) + \cos\alpha M_Z^{(n-1)-}e^{\frac{-TR}{T1}} \tag{1.14}$$

In the steady state, $M_z^{n-} = M_z^{(n-1)-}$, and Eq. 1.14 can be written as;

$$M_z = M_0(1-e^{\frac{-TR}{T1}}) + \cos\alpha \cdot M_z e^{\frac{-TR}{T1}} = \frac{M_0(1-e^{\frac{-TR}{T1}})}{1-\cos\alpha \cdot e^{\frac{-TR}{T1}}} \tag{1.15}$$

where M_z is the longitudinal magnetization vector before excitation in the steady state and α is the flip angle by which the longitudinal magnetization vector is tilted away from the z axis (Fig 1.3).

Considering the signal detection in the transverse plane and the effect of TE (time of echo: defined in Fig. 1.6) and T_2* in gradient echo sequences, the signal magnitude (S) is given as,

$$S \propto N(H) e^{-TE/T2^*} \sin\alpha \frac{M_o(1-e^{\frac{-TR}{T1}})}{(1-\cos\alpha \cdot e^{\frac{-TR}{T1}})}. \qquad (1.16)$$

where $N(H)$ is density of ${}_1^1H$ of the sample.

From Eq. 1.16, we identify three components of the signal in gradient echo sequences. The first component is the density of ${}_1^1H$ in the sample. The second component depends on the ratio of TE time to T_2^* ($e^{\frac{-TE}{T2^*}}$). The third component is modulated by the effective TR period, flip angle and the T_1 of the tissue ($M_z^n = \frac{M_0(1-e^{\frac{-TR}{T1}})}{1-\cos\alpha \cdot e^{\frac{-TR}{T1}}}$). The TE time to generate the maximum T_2^* weighted contrast can be shown to be at $TE \approx T_2^*$[45]. In order to maximize the contribution from the second factor for a fixed TR, the equation $\frac{d}{d\alpha}(\frac{1}{1-\cos\alpha \cdot e^{\frac{-TR}{T1}}}) = 0$ is solved with respect to α. The resulting angle α_E is referred to as the Ernst angle [42].

$$\alpha_E = \text{Ernst angle} = \cos^{-1}(e^{\frac{-TR}{T1}}). \qquad (1.17)$$

Equations 1.16 and 1.17 are important for maximizing the BOLD functional signal with respect to the temporal and spatial resolution and will be used in later chapters.

MR Contrast

The relaxation constants, T_1 and T_2, as well as ${}_1^1H$ density are different from one tissue to another (as illustrated in Table 1.1)[42], and difference in these constants result in different signal magnitude causing contrast between tissues. Based on Eq. 1.16, which describes the MR signal magnitude for gradient echo sequences, the MR signal contrast between two different spin-bearing samples depends on the choice of TE and TR.

Tissue	T_1 (msec)	T_2(msec)	Relative ^1_1H density
White matter	510	67	0.61
Gray matter	760	77	0.69
CFS	2650	280	1.00

Table 1.1 Relaxation constants for selected tissues at 1.5T, and relative ^1_1H density with respect to ^1_1H density of CFS.

For example, if a small TE is used (< < 10 msec), the contribution from the term $e^{\frac{-TE}{T2^*}}$ in Eq. 1.16 is relatively small compared to the signal difference caused by the differences in T_1 of tissues if a relatively short TR is used (T_1-weighted). If a large TR is used (TR > > 2000msec), the contribution from differences in T_1 is small, and TE can be chosen so that the signal contrast is weighted toward the difference in T_2* (T_2*-weighted). If TR is long and TE is short, the difference in signal magnitude is weighted primarily by the difference in ^1_1H density (proton weighted).

Chapter 2
Fundamentals of Functional MRI

2.1. Introduction

Functional MRI is an imaging technique that relates brain anatomy to the corresponding neural function. The challenge is to determine which parts of the brain are active during the performance of a certain function by measuring signals associated with the neuronal activities in brain. In the past, cognitive neuroscientists have relied on studies of laboratory animals and patients with localized brain injuries to gain insight into brain function ([46]-[48]).

Functional imaging of the human brain has been performed by detecting radiation decay of single photons emitted from radioisotope-labeled pharmaceutical agents in Single Photon Emission Computer Tomography (SPECT) or the radiation due to pairs of photons created by annihilation of positron-electron-pairs in Positron Emission Tomography (PET). However, these techniques are invasive due to the need to inject radioactive isotopes [50, 51]. Non-invasive techniques such as EEG (ElectroEncelphaloGraphy) and MEG (Magneto-Encelphalo-Graphy) have been used to map the source of electrical and magnetic fields associated with neuronal activation in high temporal resolution. However, the inverse solution for source localization is inherently inaccurate [52, 53], and spatial resolution of the methods is low, on the order of a centimeter [52].

Functional MRI (fMRI) can be used to detect the intrinsic signal changes caused by blood oxygenation level, local cerebral blood flow (CBF) and cerebral blood volume (CBV) during neuronal activity in the brain. fMRI enables the examination of human cortical function without the use of radioactive contrast agents and with reasonable temporal and spatial resolution. In the following sections, we review the contrast mechanisms and basic physiological foundations of functional MRI along with the current MR sequences and methods used.

2.2. Contrast in fMRI

2.2.1 Physiological Basics in Neuronal Activation

From functional studies such as direct action potential measurement and optical imaging using an infrared light source [54,56], neuronal activity is found to take place with delays in the range of 100's of milliseconds between stimulus presentation and neuronal response for most of the brain regions [52]. Functional MRI detects changes in the perfusion-state modulated by the neuronal activity of the brain. Hemoglobin, the oxygen-carrier in blood, acts as a shuttle to deliver oxygen after binding to the oxygen. Hemoglobin bound to the oxygen is called oxygenated-hemoglobin (also known as oxyhemoglobin) whereas the oxygen-depleted form of hemoglobin is called deoxygenated-hemoglobin (deoxyhemoglobin). The concentration of local oxyhemoglobin and deoxyhemoglobin is determined by cerebral blood flow (CBF), cerebral blood volume (CBV), and local oxygen consumption [55,56].

During neuronal activation, neuronal cells require extra energy, and their oxygen consumption increases. Oxygen supplies are provided to neuronal cells via perfusion and diffusion, however, the exact physiological mechanism is still unclear [34, 55, 56]. Increase in oxygen consumption leads to an increase in local CBF. As CBF increases, the local tissue and vascular compliance in the brain determine the local CBV. The supply of oxygen eventually overcompensates for the initial increase in oxygen consumption. As a result, there is an increased concentration of oxygenated hemoglobin with respect to the deoxygenated hemoglobin (hyperoxemia) [56].

2.2.2 Contrast Mechanisms in Functional MRI

Exogenous paramagnetic contrast agents such as gadolinium or dysprosium compounds have been used to relate changes in CBF and CBV to signal contrast in MRI. These contrast agents are paramagnetic and create a local magnetic inhomogeneity, which results in a local phase variation. If there is significant phase variation within a voxel, there will also be significant amount of phase-cancellation within a voxel [55,59]. This intravoxel-dephasing results in loss of signal in T_2* weighted imaging sequences.

By injecting a bolus of these paramagnetic contrast agents into the bloodstream, changes in CBV and CBF during neuronal activity can be measured. For example, according to the work of Rosen et al. [4], an intravenous administration of a bolus contrast agent, induces transient reduction in T_2 or T_2* weighted signal and changes in intravascular concentration of the contrast agents can be estimated by the signal reduction. By integrating the concentration-time curve and normalizing to the integrated arterial input data, CBV has been estimated. CBF is quantified from the change in CBV normalized to the estimated mean-transit time of contrast agents in the region. However, injected contrast agents have to be cleared from the blood stream before the new sets of data are obtained, therefore, repeated data acquisition is limited. In addition, the injection of exogenous contrast agents is an invasive procedure.

An approach that does not depend on the injection of exogenous contrast agents is spin labeling, [57]. Water protons from in-flowing arterial blood can be labeled using spin-saturating RF pulses. From Echo Planar imaging and signal targeting with alternating RF (EPISTAR), maps of changes in CBF can be created by subtracting two sets of data acquired alternatively with and without a 180° inversion applied to the proximal region of arteries. However, the technique is limited to the imaging of one slice per scan. This mechanism, detecting activation via changes in cerebral blood flow, is referred to as flow-related enhancement (FRE).

2.2.3 BOLD Contrast

Local changes in the state of oxygenation can also be detected by the Blood Oxygenation Level Dependent (BOLD) contrast mechanism. The basis of the BOLD technique is that deoxyhemoglobin acts as an endogenous paramagnetic contrast agent and therefore, changes in its local concentration lead to the variation in T_2 or T_2* weighted MR images ([55],[58]-[62]). As hemoglobin (Hb) becomes deoxygenated, it becomes more paramagnetic than the oxygenated Hb and thus creates a magnetically inhomogeneous environment. The signal increase in T_2 or T_2* weighted images acquired during cortical activation reflects a decrease in deoxyhemoglobin content, *i.e.*, an increase in blood oxygenation. The blood hemoglobin paramagnetism decreases with brain activation and the local CBV increases. The resulting decrease in tissue blood magnetic susceptibility differences leads to less intra-voxel dephasing within cortical tissue and hence increased intensity level in appropriately weighted images [55]. Because BOLD contrast does not require the injection of contrast agents and multi-slice acquisitions are possible, it is most widely used for fMRI today [62].

Blood oxygenation level dependent (BOLD) contrast varies according to the type of sequence used in the experiment. Gradient-echo sequences are most sensitive to the changes in local T_2* whereas spin-echo sequences are most sensitive to the T_2 variations associated with BOLD effects.

Gradient Echo Sequences

Similar to the case where an exogenous paramagnetic contrast agent is present, the susceptibility difference results in local inhomogeneity due to BOLD effect and creates a phase variation of blood with respect to the surrounding tissue. If this phase variation is distributed over the size of a voxel, there can be a significant amount of phase-cancellation within the voxel (intravoxel-dephasing), resulting in the loss of intensity in T_2*-weighted images. Based on the magnitude of MR signal described in Eq. 1.16, the signal contrast (ΔS) between activated and baseline states becomes,

$$\Delta S = S_o e^{-TE \cdot R_2{}^*{}_{BASE}} (e^{-TE \cdot \Delta R^*{}_2} - 1), \qquad (2.1)$$

where R^*_{2BASE} is the transverse relaxation rate ($1/T^*_{2\ BASE}$) in baseline states and ΔR^*_2 is the transverse relaxation rate ($1/T^*_2$) due to the activation. S_0 represents the initial baseline signal. When $TE \cdot \Delta R^*_2 << 1$, the above equation can be approximated as;

$$\Delta R^*_2 \approx -\frac{\Delta S / S_o}{TE}. \qquad (2.2)$$

Since the different dimensions and orientations in the vessel types (vein, venuoles, and capillary), and physiology (such as recruitment and dilations) affect the intra-voxel phase dispersion, it is difficult to exactly quantify the phase change due to BOLD activation. However, mathematical models suggested that the degree of contribution from the larger vessels ($\Delta R^*_2 = \text{-}3.4\,\text{s}^{-1}$) is greater than from the capillary-based tissue ($\Delta R^*_2 < \text{-}1\,\text{s}^{-1}$) [61]. Gati et al. investigated the percentage change due to BOLD effect, and estimated ΔR^*_2 for the both vessel and tissue [22], which agreed well with the theoretical value by Boxerman et al [61]. According to their work, up to ~18% of signal change is expected in the vessel whereas only ~2% is expected from the tissue at 1.5 T. Using high magnetic field environment at 4.0T, Menon *et al.* [56] reported that a large portion of the signal changes that accompany photic stimulation comes from capillary-containing tissues that are not visible in lower field. In gradient-echo experiments at 1.5T, the dominant source of signal is from the draining veins [62, 63].

Spin-Echo Sequences

The BOLD contrast obtained with spin-echo sequences is considerably smaller than that obtained using gradient echo sequences [65,67]. The BOLD contrast elicited by changes in the transverse relaxation rate, ΔR, in spin-echo sequences is smaller than changes due to ΔR^* with gradient-echo sequences by a factor of ~0.3 at 1.5T[65]. However, in spite of the smaller changes in transverse relaxation rate, spin-echo sequences are a serious alternative for fMRI experiments because, unlike gradient echo sequence where the dominant source of signal is from the large draining veins, BOLD contrast arising from the spin-echo sequences more likely reflects change of oxygenation in microvessels such as capillaries [60,63],

It has been shown that spin-echo sequences are sensitive to the BOLD effect due to the random motion of water molecules in the extravascular space [65,66]. The presence of magnetic field gradients at the interface between blood vessels and surrounding tissue will result in MR signal loss [55,61]. Several biophysical models accounting for these factors predict that resulting transverse relaxation rate, ΔR, in spin-echo sequences are more sensitive to regions around vessels of small radius (dimension similar to capillary diameter in the order of 2-7 μm) than regions associated with large vessel radius [55,64,65].

Spatial and Temporal Characteristics

The neuronal activation is known to occur at the site of single or groups of neurons that are responsible for certain functional sub-units and these sub-units overlap each other to form functional units [56, 68]. For instance, the functional subunit for ocular dominance is determined by an area (Ocular Dominant Columns), typically 5-10mm in length and 0.8-1.2mm on a side, however, the functional unit *as a whole* may extend to centimeter long columns [56]. Similar observations have been reported for the study of somatotopy in hand motor-area with overlapping areas of sub-units responsible for the movement of individual digits [10] and for study of bilingual generation with overlapping areas for different languages [26]. The minimum detectable size of functional activity at 1.5T is well under a millimeter, based on the various studies where data was acquired at high spatial resolution [26,60,63].

In terms of the temporal characteristics in BOLD activation, images can be collected in a very short time using fast imaging sequences therefore, high temporal resolution is possible in principle. The hemodynamic response, on the order of 2 to 3 seconds, lags behind the time of neuronal activity. However, in spite of the delay in hemodynamic response, high temporal resolution is desirable to resolve the sequential involvement from the multiple cortical areas and the associated hemodynamic responses [34, 69, 70].

Field Strength

The magnitude of BOLD contrast is dependent on the field strength. The stronger the magnetic field, the greater is the BOLD signal contrast due to the greater intra-voxel dephasing which scales with field strength [22,55]. However, chemical shift and other susceptibility-related effects also result in more serious image distortion, demanding a greater attention to field shimming and distortion correction [42].

Flow-related Effects

The functional MR signal may contain both flow-related and BOLD components [71]. The signal coupled with the venous side of the capillary bed may remain deoxygenated before being diluted by the larger pool of venous blood. Thus, in addition to the brain parenchyma, image locations distant from the actual activated location may also show intensity changes. Blood flow changes, which do not relate to neuronal activation may appear, therefore, due to the continuous connectivity in vasculature. These so-called in-flow effects complicate the precise anatomical localization of brain activation [71]. Due to the long TR period usually associated with single-shot EPI, there is generally much less sensitivity to the in-flow effect. However, for monitoring a single slice where a short TR is required for high temporal resolution, the single-shot EPI method will also be susceptible to in-flow effects. Volume encoding is an option for in-flow suppression but general volume-encoding methods suitable for functional MRI entail long scan times [72, 73].

2.3 Overview of an fMRI Experiment

2.3.1 Experimental Design and Procedures

A functional MRI experiment is designed to detect signal contrast generated by neuronal activities associated with task paradigms. Although there are variations in experimental design, fMRI experiments generally consist of several common steps. The first step is to identify the hypothesis to be tested (Sample hypothesis: There is a difference between mean pixel intensity between motor activation and rest states). In the next step, a

BOLD or flow sensitive imaging sequence is employed to detect the activation-related intensity changes and test the hypothesis. Due to low inherent CNR, many images are acquired repeatedly, covering the same volume while the subject performs tasks. For example, as illustrated in Fig.2.1, the alternating control and active epochs are presented with blocks of successive repetitive events ('block-based' design).

The stimuli are presented in a matter such that the time of stimulus presentation with respect to image acquisition is recorded for later analysis. The performance of the subject may also be monitored using devices such as motor recording systems [21]. Once the data is acquired, it is generally reconstructed off-line but analysis may also be done in real-time depending on capabilities of the system [74].

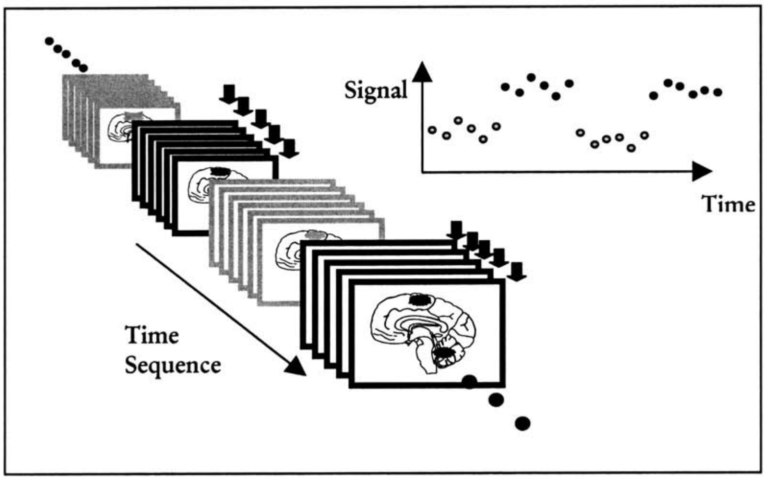

Figure 2.1 Schematic of block-based functional MRI paradigm. The alternating control and active epochs are presented with blocks of successive repetitive events (indicated by arrows). The signal response from the activated region is simulated in the plot.

Another step in a functional MRI experiment may involve pre-processing of the data for a realignment of all images in the time-series to correct for any bulk head-motion, for normalization of the individual brain morphology to standardized Talairach-Tournoux space [75] or for spatial smoothing [76]. After the preprocessing stage, in order to differentiate the signal between activated and deactivated stages, any of a number of statistical methods are applied to extract the spatial and temporal information of the activation with respect to the cognitive tasks used in the experiment. Such methods include simple subtraction [34], cross correlation [20], student's T test [21], Fourier analysis [77], or the Kolmogorov-Smirnov method [78].

During the scan session, bulk motion of the head may result in the misregistration of the anatomical locations and generates inaccurate information regarding functional activation. To immobilize the head during the imaging session, a bite-bar or air cushion can be used. If 3D image sets are acquired, motion correction algorithms can be applied by calculating rotational and translational motion-related vectors, and transforming the data accordingly [79, 80]. In spite of these corrective measures, motion may still introduce misregistration of images. Therefore, the active participation of the subjects and patients for immobility during the scan session is generally necessary.

In functional MRI, the signal fluctuations that are not associated with the task-related signals affect the quality of functional mapping ([81]-[83]). The major contributors to these signal fluctuations are cardiac, respiratory, and cardiac-induced CSF pulsation [77,82]. Strictly speaking, these signal fluctuations, observed to be spatially covariant [78], should not be identified as 'noise' because they derive from deterministic process. However, throughout the thesis, we refer to these signal fluctuations as 'physiological noise', because they are not task-related signals.

The exact quantification of the physiological noise component is difficult because it originates from the complex interactions between tissue and cardiac/respiratory variables as well as other unknown factors [24, 28, 76]. Several methods to reduce the physiological noise have been proposed. Navigator echoes have been used to monitor cardiac and respiratory cycles so that the cardiac and respiratory components can be removed retrospectively [81]. Other retrospective-filtering approaches combined with monitoring of key vital signs during the functional session have been used [82, 83]. Spin-echo based sequences [59,65] have been shown to be affected less by physiological noise. It is hypothesized that rapidly flowing spins associated with cardiac pulsation may not be refocused and, therefore, will not contribute to signal fluctuations.

2.3.2 Data Acquisition Methods

Functional MRI requires repeated imaging of a single volume of interest to compensate for the inherently low BOLD contrast-to-noise. The area of activation in the brain is not always known a priori, nor is it necessarily confined to a single slab of imaging plane, making it necessary to observe multiple slices simultaneously. Whole volume coverage of the brain also offers advantages over single slice acquisition when correcting for head-motion during the session, or for avoiding 'inflow' artifact (See section 2.2.3).

The majority of functional MRI experiments utilize gradient-recalled echo-planar sequences (EPI, Chapter 1), permitting excellent temporal resolution and full coverage of the brain. Although EPI requires special hardware for the fast gradient switching, the speed, excellent T2* contrast, and insensitivity to in-flow, make gradient-recalled echo-planar sequences the primary tool for functional MRI.

Fast methods other than multi-slice gradient-recalled EPI have also been developed for fMRI such as ES (echo-Shifted) FLASH, PRESTO (Principles of Echo Shifting with a Train of Observation), and MUSIC (Multi-slice Interleaved Excitation Cycles)[72,84,85]. In these methods, TR is made shorter than TE, by interleaving excitations, thus volume coverage is achieved in a reasonable time period. Echo Volume Imaging (EVI) has also been proposed to enhance the advantage of EPI sequence with true volume encoding (the through-plane direction is also phase-encoded) [86]. Functional MRI using key-hole k-space acquisition [37] or single-shot half k-space EPI [35] have been used to reduce k-space acquisition requirements (see Section 1.1) and to increase the temporal resolution.

Spin-echo sequences such as asymmetric spin echo [78] or the fast spin echo sequence [65] have also been used in fMRI. As discussed in Section 2.2.3, spin echo sequences are sensitive toward to the BOLD signal component in smaller vessels and diffusion in brain parenchyma. In addition, they are less sensitive to pulsatile flow-artifact and less sensitive to macroscopic field distortion due to poor shimming or tissue/air interfaces. Although the intrinsic BOLD contrast is less than obtained using gradient echo sequences, the sensitivity to micro-vasculature and a relative immunity from the susceptibility-related signal loss make the spin-echo sequences a serious alternative for functional MRI studies. Spin-echo techniques have not been widely used, however, due to low BOLD contrast-to-noise [59,61].

2.3.3 Event-Related Design

The range of task designs used in fMRI include both event-related (ER-fMRI) designs, which are used to detect changes due to a single impulse event (Fig 2.2) and the block-based designs where the events are presented in blocks of time (Fig 2.1) [12, 28, 87, 88, 89]. ER-fMRI is useful where the traditional block-based design can not be easily used. Such cases include, for example, the study of working-memory paradigms such as recollection and familiarity [14, 90] where stimuli must necessarily be applied randomly as single events. ER-fMRI avoids possible contamination of working-memory events which may be introduced if repetitive memory cues are given in 'block'.

ER-fMRI began from the observation that a significant response can be elicited even when a very brief duration of stimuli is presented [30, 91]. The analysis of ER data is done assuming a linear system where a neural impulse input is convolved with the intrinsic hemodynamic response function to generate a reference waveform for correlation analysis. Several cases of departure from linearity have been reported, especially when the period of each events is less than a second, however, the linearity assumption has been shown to be valid in most cases ([90]-[92]). The detailed information and knowledge about the hemodynamic response which constitutes the basis for event-related fMRI is not clear, and is the subject of many investigations [11, 12, 92].

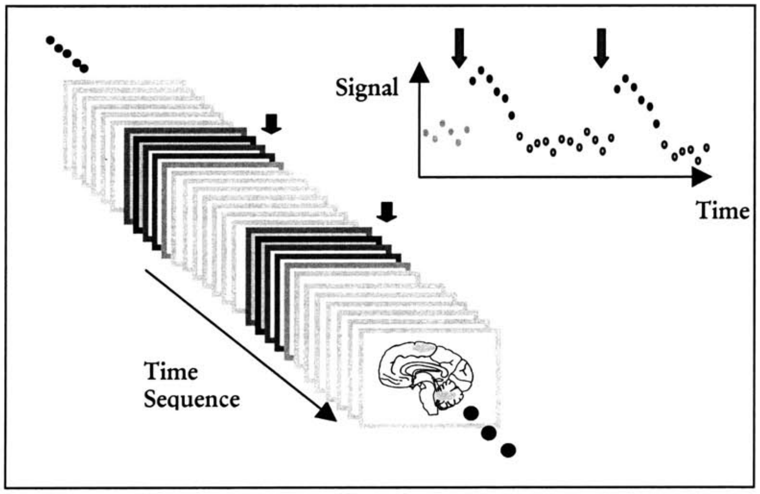

Figure 2.2 Schematic of an event-related functional MRI paradigm. Unlike the block-based design in Fig 2.1, where the task is given in blocks of same type of trials, the impulse of single type of event (in arrows) is presented. The signal response from the activated region is simulated in the plot.

Chapter 3
Spatially-selective RF Encoding

3.1 Introduction

RF encoding based on spatially selective excitation is not limited to acquisition of data in k-space and, therefore, offers greater flexibility for spatial encoding than that is offered by conventional Fourier encoding. For example, the wavelet-encoding method was proposed for adaptive updating of the encoding scheme during dynamic imaging [40]. Encoding by singular value decomposition (SVD) has also been implemented for dynamic imaging where the SVD of the image matrix is used to update the encoding basis [41]. In this chapter, the fundamentals of RF encoding and image decoding which are central to the proposed adaptive fMRI method will be described in terms of a useful matrix representation. Effects due to the imaging point-spread-function (PSF) in RF encoding are also investigated and an analysis of SNR is presented.

3.1.1 RF Selective Excitation

As described in Section 1.2.2, the dynamic interaction between the B_1-field generated by a RF pulse and the magnetization vectors in the sample is described by the Bloch equation (Eq. 1.8). Assuming the laboratory frame of reference and relaxation matrix $\Re$, from Eq. 1.8, and Eq. 1.9, we obtain the following set of differential equations;

$$\frac{dM_x}{dt} = \gamma M_y (B_o - \omega / \gamma) - \frac{M_x}{T_2},$$
$$\frac{dM_y}{dt} = \gamma M_z B_1 - \gamma M_x (B_o - \omega / \gamma) - \frac{M_y}{T_2}, \tag{3.1}$$
$$\frac{dM_z}{dt} = -\gamma M_y B_1 - \frac{(M_z - M_o)}{T_1}.$$

According to the small flip angle approximation [94], when the flip angle is small (i.e.,$\leq 30^o$), the longitudinal magnetization, M_z, is approximately constant (*i.e.* $\frac{dM_z}{dt} = 0$). If the duration of the RF pulse is considerably smaller than T_1 and T_2, the effect from relaxation can be ignored so that $\frac{M_x}{T_2} = 0$ and $\frac{M_y}{T_2} = 0$. Thus, for the transverse component of the magnetization, $M_{xy}(t) = M_x(t) + iM_y(t)$, assuming an initial condition of $M_z = M_o$ and a constant magnetic gradient, G, applied in the x direction during the RF excitation, the following is obtained [43],

$$\frac{dM_{xy}}{dt} = -i\gamma G \cdot x \cdot M_{xy} + i\gamma B_1(t) M_o \ . \tag{3.2}$$

Solving Eq. 3.2,

$$M_{xy}(x) = i\gamma Mo \int_0^T B_1(t) e^{-i\gamma G \cdot xt} dt \,. \tag{3.3}$$

From Eq. 3.3 we see that the spatial profile of excitation, $M_{xy}(x)$, is in the form of a Fourier transform of $B_1(t)$ with respect to time. Therefore, for a constant slice selective gradient, a small flip angle and short RF pulse duration, the profile of the spatially-selective pulse can be approximated by Fourier transformation of the RF pulse shape [43]. Using the small flip angle approximation, it has been shown that RF pulses can be tailored to form virtually any non-Fourier encoding basis by manipulating the phase and the magnitude profile of the RF pulse [43].

3.1.2 Matrix Representation of RF encoding

Drawing on the work of Panych et al [93], we use a matrix representation to describe the RF encoding-decoding processes based on a linear response model. The matrix representation provides a simple and elegant means of generating RF pulse definitions and analyzing the MR signal response. For simplicity, let us represent the multi-dimensional MR encoding technique as separate 1-dimensional operations in each dimension. We define $s(x)$ as a one-dimensional MR signal density distributed in space. We also define $\Phi(x)$ as a function that is centered at x=0 and has a spread of Δx, which will serve as a sampling or point-spread-function (PSF). We then define a spatially selective set of basis functions, $\{\Phi_m(x)\}$,

$$\Phi_m(x) = \Phi(x - m\Delta x), \tag{3.4}$$

where $m = 0,1,2,\ldots\ldots, M-1$, and $\Delta x = FOV/M$, and M is the number of volume elements along the FOV. Thus, $s(x)$ can be represented by the expansion,

$$s(x) \cong \sum_m s_m \Phi_m(x). \tag{3.5}$$

The set of coefficients $\{s_m\}$ can be thought of as a discrete estimate of $s(x)$.

During imaging, a spatially-dependent weighting function or 'encoding function', $t_n(x)$, is applied by manipulation of the phase and magnitude of the RF pulse. These encoding functions can also be represented in terms of the basis in Eq. 3.4 so that,

$$t_n(x) = \sum_{m=0}^{M-1} T_{nm} \Phi_m(x) \tag{3.6}$$

where T_{nm} is an element of an N x M encoding matrix $\overline{\overline{T}}$. For example, if a 8-level Hadamard matrix is used to generate encoding functions, the set $\{t_n(x)\}$ is the result of a matrix-vector multiplication of the n^{th} row elements of $\overline{\overline{T}}$ with corresponding functions in $\{\Phi_m(x)\}$. Thus, in this example, each eight-element row in $\overline{\overline{T}}$ is a discrete representation of a Hadamard encoding function. In Fourier encoding, each $t_n(x)$ is a complex exponential function, and $\Phi_n(x)$ is a sinc-like function.

Given the above definitions, the acquired signal, $y_n(x)$, obtained using an encoding function, $t_n(x)$, is;

$$y_n = \langle s(x), t_n(x) \rangle = \langle s(x), \sum_{m=0}^{M-1} T_{nm} \Phi_m(x) \rangle = \sum_{m=0}^{M-1} T_{nm} \langle s(x), \Phi_m(x) \rangle = \sum_{m=0}^{M} T_{nm} s_m \qquad (3.7)$$

where $\{ s_m \}$ are the coefficients of the expansion in Eq. 3.5.

Equation 3.7. can also be represented in matrix form,

$$\bar{y} = \bar{\bar{T}} \bar{s}, \qquad (3.8)$$

where $\bar{y} = [y_0 y_1 y_2 ...... y_{N-1}]^T$ and $\bar{s} = [s_0 s_1 s_2 ...... s_{N-1}]^T$.

According to Eq. 3.8, the estimate, $\bar{s}$, of spin density of the sample, $s(x)$ can be decoded from a set of measurements by matrix inversion and matrix-vector multiplication;

$$\bar{s} = \bar{\bar{T}}^{-1} \bar{y}. \qquad (3.9)$$

3.2 Point-Spread Function of RF Encoding

In the previous section, we have shown that imaging information and encoding functions can be represented in terms of the point-spread function. The PSF of an encoding basis contains information about the imaging resolution. The PSF, in general, also describes spatial range of information in the image estimate. In Hadamard encoding using RF excitation, the overlap between excitation profile, which can be described by PSF, may cause uneven degree of excitation over time, introducing 'cross-talk' which influences the time course of the MR signal.

Figure 3.1 shows the ideal PSF for Hadamard encoding, the box-shaped function shown on the left of Fig. 3.1a. However, it is practically impossible to excite profiles built from this PSF without the use of extremely long RF pulses (right side of Fig 3.1a). Thus, in practice, the RF pulse duration is truncated, introducing a ringing of the profile of the point-spread-function (Fig 3.1b). An example of a sinc RF pulse, truncated after the first side lobe and windowed with cosine function to reduce the ringing, is shown in Fig 3.1c along with the associated PSF. A box shaped RF pulse minimizes the pulse duration but generates a sinc PSF which has many side lobes (Fig. 3.1d).

Since truncation of a sinc-shaped RF pulse causes ringing or broadening of the PSF, this may result in overlap of adjacent excitations in RF encoding and an uneven temporal pattern of excitation over the volume. This may introduce undesirable fluctuations into the functional signal. The relationship between the excitation profiles and the functional MR signal will be examined in detail in the next section.

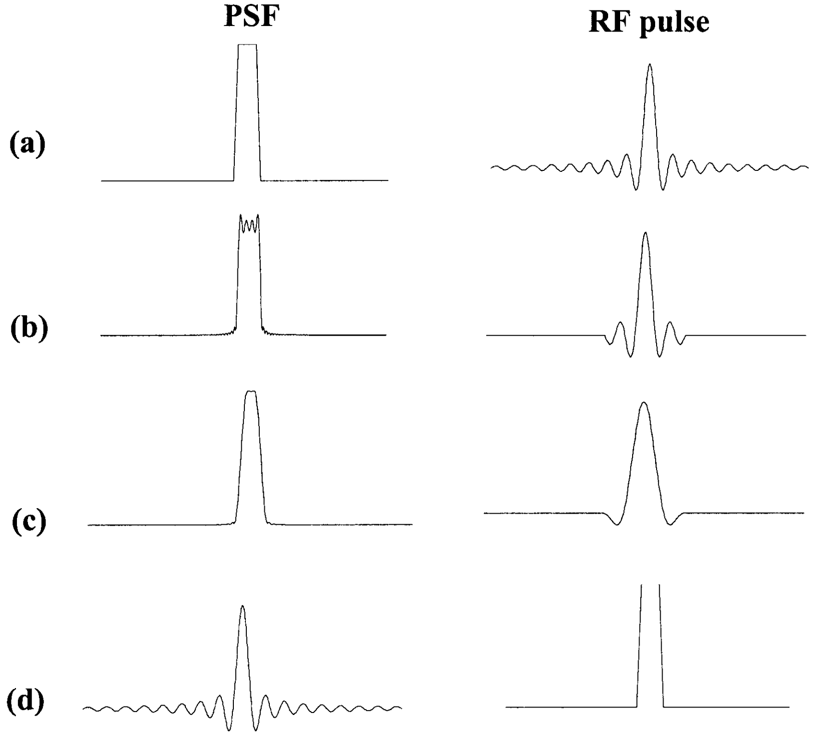

Figure 3.1. Comparison of different point-spread-functions and their RF pulses. (a) Ideal box-shaped PSF and sinc RF pulse, (b) PSF of truncated sinc function, (c) PSF of cosine-windowed sinc at first side-lobe, and (d) PSF of box-shaped RF pulse.

3.2.1 Cross-talk in RF encoding

The illustration in Fig. 3.2 shows an example of how the overlap in RF excitation profile can modulate the effective TR period experienced at different locations. Assume that the spatial profiles of excitation, S1 and S2 as shown in Fig 3.2 are applied alternatively every TR period. At locations A, B, and C, the magnitude of the spatial profile of excitation varies over time, therefore, the flip angle at each location changes as imaging progresses. For example, in the case illustrated in Fig. 3.2, location B will have different steady-state magnitude of M_z due to the shorter TR time to recover the M_z magnetization as compared to the location A (2TR vs. TR). Location C experiences flip angle of $\alpha/2$ in every other TR period. The result is a variable T1-weighting across the field of view.

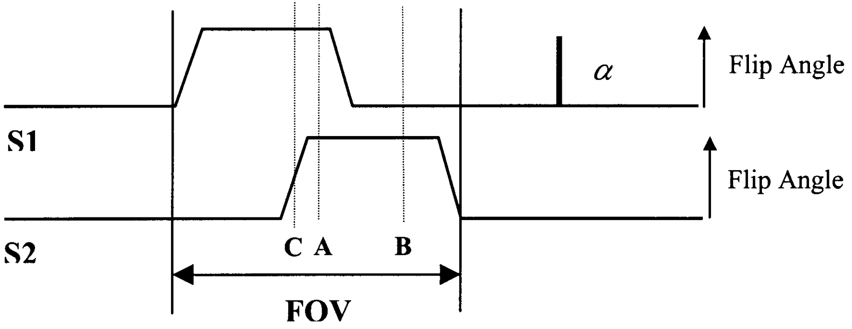

Time	0	TR	2TR	3TR	4TR	5TR	6TR	………
Point A	α	α	α	α	α	α	α	………
Point B	α	0	α	0	α	0	α	………
Point C	α	$\alpha/2$	α	$\alpha/2$	α	$\alpha/2$	α	………

Figure 3.2 Illustration of the spatial cross-talk in RF excitation. The spatial profiles of excitation, S1 and S2 are applied in sequence in time separated by a TR period. The table below indicates the degree of flip angle excitation at each location in time sequence. This will result in uneven level of saturation over the FOV in time.

The spatial overlap of excitation profiles can cause an uneven level of saturation due to the application of different flip angles in time. The effect from the overlap between spatial profiles may be reduced by 'interleaving' the order of excitation to allow for a longer effective TR. However, increasing TR is not practical for volume encoding methods where large portions of the volume are involved on each excitation.

We will illustrate the effect of crosstalk on the signal behavior with Hadamard encoding. Assume 16 Hadamard encoding functions $\{ t_n(x) \}$ are built from the PSF shown in Fig 3.1c. The encoding functions and their magnitude profiles of spatial excitation are shown in Fig 3.3. For true Hadamard encoding, as with Fourier encoding, there should be the same degree of excitation across the FOV for all encodes. However, because of the need to use RF pulses of short duration, the PSF's are overlapped, and there will be temporal variations in the magnitude profile as demonstrated by right column of Fig 3.3. When the profiles are excited in a time sequence, the excitation varies over time for different locations within the FOV, causing signal fluctuations.

As an example, we considered two Hadamard encoding cases. In the first case, Hadamard functions are built from the PSF in Fig 3.1b, and in the second case, they are built from the PSF with less ringing in Fig. 3.1c. We simulated the case where the encoding functions are applied ten times each in sequence (TR of 100 msec, T_1=760 msec). The magnitude of longitudinal magnetization at one location in the FOV was calculated to examine signal fluctuations over time for the two cases. The result is plotted in Fig 3.4 for a location at the center of the FOV where there is maximum signal fluctuation. As expected, there was a periodicity in signal fluctuations with a period of 16 TR due to repetitive excitation with the 16 encoding functions. The signal variation was small, only between 0.12% and 0.4% of the mean signal level. Because it is not correlated with the task paradigm, this merely adds to the base-line noise level, and should not significantly affect the fMRI result. However, there should still be attention to the design of RF pulse profiles to minimize introduction of "RF encoding noise" by reducing overlap between adjacent profiles.

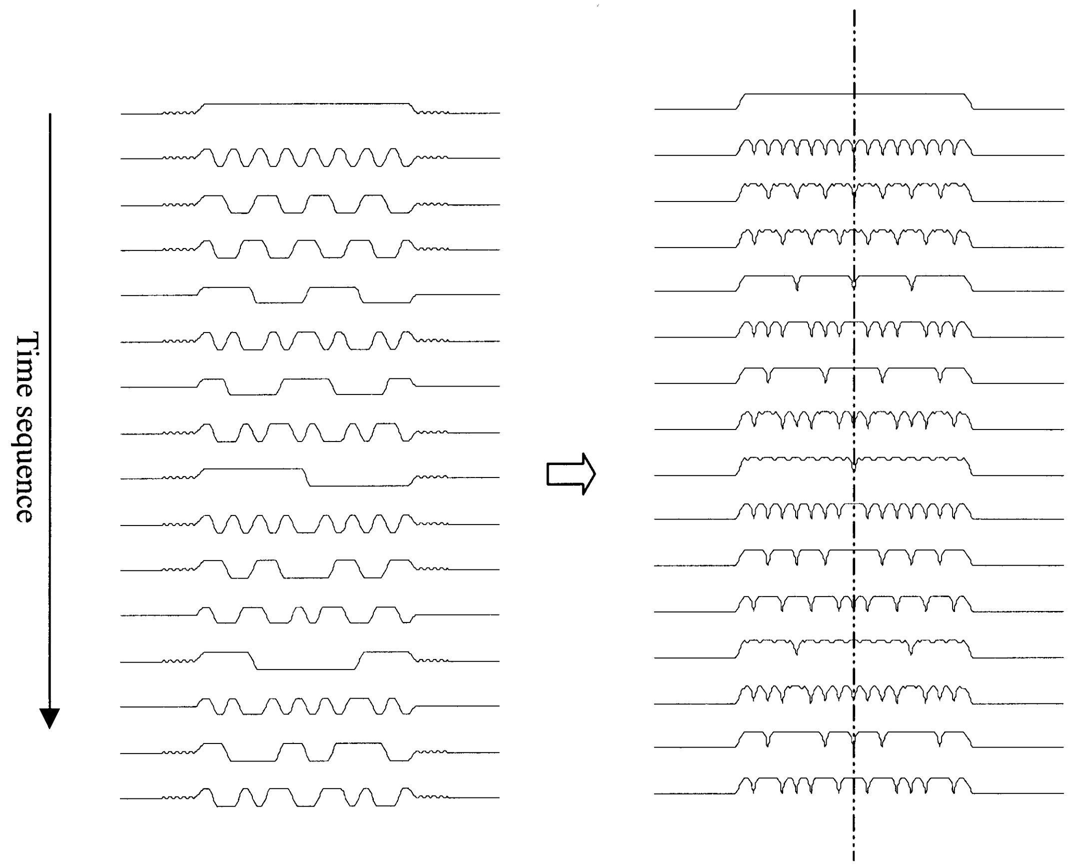

Figure 3.3 The left column shows 16 Hadamard encoding functions where the PSF is as shown in Fig. 3.1c. Right column shows magnitude profiles of the encoding functions. The dashed line indicates the location for which the longitudinal magnetization magnitude was simulated (Fig 3.4).

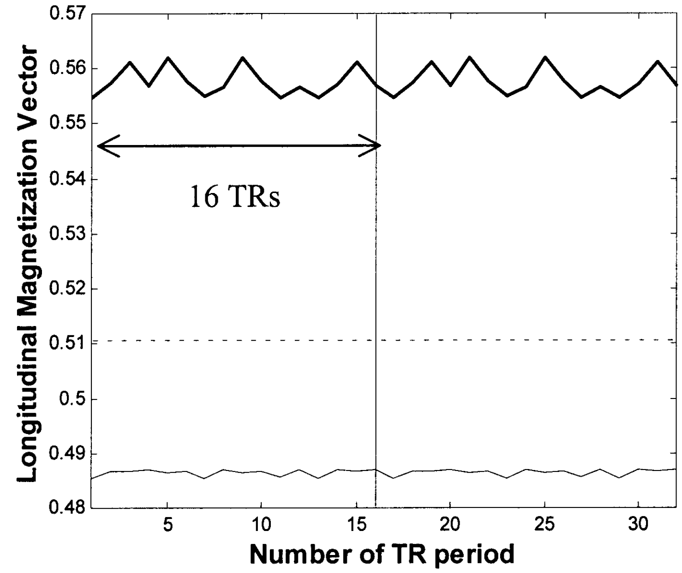

Figure 3.4. Illustration of effect of crosstalk on the magnitude of M_z using 16-Level Hadamard encoding. Hadamard functions were built with two different PSFs (The thick line shows the result for the PSF in Fig 3.1b and the thin line shows result from the PSF in Fig 3.1c). The dotted line is the result assuming perfect Hadamard profiles. The temporal fluctuation of the longitudinal magnetization is due to uneven T_1 weighting.

3.3 RF Encoding for fMRI

3.3.1 Matrix Representation

RF encoding consists of forming combinations of basic volume elements by manipulation of the RF pulse shape. Figure 3.5 indicates some of the basic volume elements that can be selected via RF excitation for non-Fourier encoding. A standard RF slice-select pulse in one direction followed by a selective refocusing in the second orthogonal direction [95,96] can excite lines. Planes can be selected by standard slice-selective technique [97]. Strips are excited using 2D selective RF pulses [98]. After the RF excitation, voxels within each unit volume can be encoded by conventional Fourier methods of phase and frequency encoding.

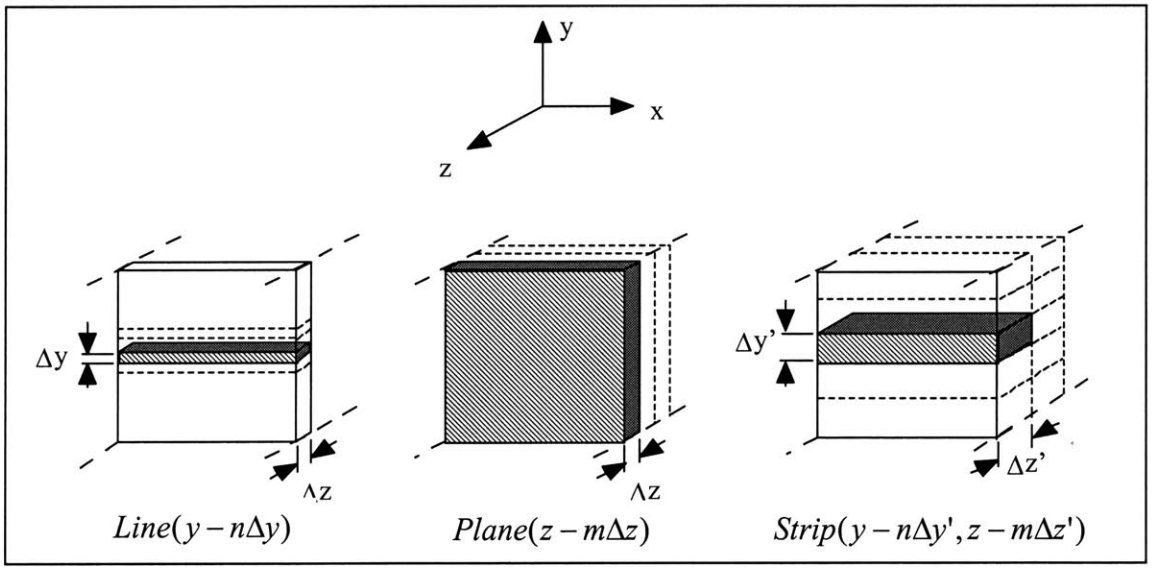

Figure 3.5 Basic volume elements that can be excited using spatially selective RF pulses. Non-Fourier encoding consists of forming linear combinations of basic volume elements distributed throughout the imaging field of view.

The RF encoding method and its matrix representation, as described previously in Section 3.1.2 for one-dimensional encoding, can be generalized for volume encoding. First, define a MxK matrix $\overline{\overline{S}}_{\{M\,\mathrm{x}\,\mathrm{K}\}}$ such that each row vector contains the frequency (and phase) encoded signal values obtained after a basic volume element (*i.e.* plane, line or strip as shown in Fig 3.5) is excited. K is the total number of k-space samples (e.g. 256x128) obtained by frequency and phase encoding one basic volume element, and M is the total number of basic volume elements within the imaging field. Low flip-angle excitations can be used to excite linear combinations of basic volumes, such that:

$$\overline{\overline{Y}}_{\{N \,\mathrm{x}\, \mathrm{K}\}} = \overline{\overline{T}}_{\{N \,\mathrm{x}\, \mathrm{N}\}} \overline{\overline{C}}_{\{N \,\mathrm{x}\, \mathrm{M}\}} \overline{\overline{S}}_{\{M \,\mathrm{x}\, \mathrm{K}\}} \tag{3.10}$$

Note that Eq. 3.10 is a generalized form of Eq. 3.8. $\overline{\overline{C}}$ is an NxM matrix whose N rows define N sets of basic volume elements throughout the imaging field that are to be excited. $\overline{\overline{T}}$ is an NxN orthogonal matrix (e.g. Hadamard or Haar) whose N rows define unique linear combinations for encoding the volumes defined by $\overline{\overline{C}}$. For example, $\overline{\overline{T}}$ can be 8 level Hadamard encoding matrix ($\overline{\overline{H}}$) or a Haar wavelet basis ($\overline{\overline{W}}$) as shown in Fig. 3.6. $\overline{\overline{C}}$ is separated from $\overline{\overline{T}}$ so that selected locations for encoding can be explicitly defined. $\overline{\overline{Y}}$ is the NxK matrix in whose rows we place the output signal values after each unique volume combination is excited.

$$\overline{\overline{H}} = \begin{bmatrix} 1 & 1 & 1 & 1 & 1 & 1 & 1 & 1 \\ 1 & -1 & 1 & -1 & 1 & -1 & 1 & -1 \\ 1 & 1 & -1 & -1 & 1 & 1 & -1 & -1 \\ 1 & -1 & -1 & 1 & 1 & -1 & -1 & 1 \\ 1 & 1 & 1 & 1 & -1 & -1 & -1 & -1 \\ 1 & -1 & 1 & -1 & -1 & 1 & -1 & 1 \\ 1 & 1 & -1 & -1 & -1 & -1 & 1 & 1 \\ 1 & -1 & -1 & 1 & -1 & 1 & 1 & -1 \end{bmatrix} \qquad \overline{\overline{W}} = \begin{bmatrix} 1 & 1 & 1 & 1 & 1 & 1 & 1 & 1 \\ 1 & 1 & 1 & 1 & -1 & -1 & -1 & -1 \\ 1 & 1 & -1 & -1 & 0 & 0 & 0 & 0 \\ 0 & 0 & 0 & 0 & 1 & 1 & -1 & -1 \\ 1 & -1 & 0 & 0 & 0 & 0 & 0 & 0 \\ 0 & 0 & 1 & -1 & 0 & 0 & 0 & 0 \\ 0 & 0 & 0 & 0 & 1 & -1 & 0 & 0 \\ 0 & 0 & 0 & 0 & 0 & 0 & 1 & -1 \end{bmatrix}$$

Figure 3.6 Example of eight-level Hadamard ($\overline{\overline{H}}$) and Haar wavelet ($\overline{\overline{W}}$) encoding matrices.

An advantage of RF encoding is that $\overline{\overline{T}}$ and $\overline{\overline{C}}$ can be manipulated dynamically depending upon the transient requirements of the imaging experiment. $\overline{\overline{C}}$ is designed to select volume sections conveniently located throughout the imaging field. $\overline{\overline{T}}$ is chosen in order to further encode each volume section and enhance SNR. In our functional MRI implementation (which will be presented in later chapters) we used planes as the basic volume element. In decoding process to recover the image estimate, $\overline{\overline{C}} \cdot \overline{\overline{S}}$ can be recovered from $\overline{\overline{Y}}$ by matrix multiplication with the inverse of $\overline{\overline{T}}$. The fully-imaged volume, represented by $\overline{\overline{S}}$, can be recovered only if $\overline{\overline{C}}$ is the MxM identity matrix ($\overline{\overline{I}}$) and $\overline{\overline{T}}$ is invertible;

$$\overline{\overline{S}} = \overline{\overline{C}}^{-1}\overline{\overline{T}}^{-1}\overline{\overline{Y}} = \overline{\overline{I}}\,\overline{\overline{T}}^{-1}\overline{\overline{Y}} = \overline{\overline{T}}^{-1}\overline{\overline{Y}}. \tag{3.11}$$

3.3.2 General SNR analysis

Due to the inherently low BOLD contrast, the inherent signal-to-noise ratio (SNR) is especially important in functional MRI studies, and the RF encoding strategy should be designed to produce the highest SNR possible. We will use the matrix representation to compare direct encoding (where $\overline{\overline{T}}$ is identity matrix in Eq. 3.10) versus volume encoding methods (where $\overline{\overline{T}}$ is Hadamard or Fourier encoding matrix) drawing on the SNR analysis of general encoding developed by Panych et al [99].

Let us define the noise and artifact-free signal estimate of $s(x)$ as the vector $\overline{s}$ defined in Section 3.1.2. Then, SNR can be expressed as,

$$SNR = \left(\frac{\overline{s}^{T}\,\overline{s}}{E} \right)^{1/2} \tag{3.12}$$

where $E = \mathcal{E}[\overline{\eta}'^{T}\,\overline{\eta}']$ represents the image noise level, $\mathcal{E}(x)$ is the expectation of x, and $\overline{\eta}'$ represents the noise vector after the reconstruction from measurements contaminated by the thermal noise vector, $\overline{\eta}$, so that,

$$\overline{\eta}' = \overline{\overline{T}}^{-1}\,\overline{\eta}. \tag{3.13}$$

For orthogonal encoding, it can be shown that the image noise is [99],

$$E = \mathcal{E}[\bar{\eta}'^T \bar{\eta}'] = \mathcal{E}[(\overline{\overline{T}}^{-1}\bar{\eta})^T(\overline{\overline{T}}^{-1}\bar{\eta})] = \mathcal{E}[(\bar{\eta}^T \overline{\overline{T}}^{-1^T})(\overline{\overline{T}}^{-1}\bar{\eta})]$$

$$= \mathcal{E}[(\bar{\eta}^T(\overline{\overline{D}}^T)^{-1}\bar{\eta})] = \mathcal{E}[\sum_{k=0}^{n}\frac{\eta_k^2}{D_{k,k}}] \tag{3.14}$$

where η_k is the k$^{\text{th}}$ element of $\bar{\eta}$ and $\overline{\overline{D}}^{-1}$ is a diagonal matrix such that;

$$\overline{\overline{D}} = \overline{\overline{T}}(\overline{\overline{T}})^T. \tag{3.15}$$

If we define the noise variance, $\sigma^2 = \mathcal{E}[\eta_k^2]$, then the expression for the image noise in Eq. 3.14 can be rewritten such that,

$$E = \mathcal{E}[\sum_{k=0}^{n}\frac{\eta_k^2}{D_{k,k}}] = \sigma^2 Tr[\overline{\overline{D}}^{-1}]. \tag{3.16}$$

If $\overline{\overline{T}}$ is a Fourier or Hadamard transformation matrix,

$$\overline{\overline{D}}^{-1} = \overline{\overline{I}}/N \text{ and } Tr[\overline{\overline{D}}^{-1}] = Tr[\overline{\overline{I}}]/N = 1, \tag{3.17}$$

The resulting noise, E, is;

$$E = \sigma^2 Tr[\overline{\overline{D}}^{-1}] = \sigma^2 \quad . \tag{3.18}$$

For direct encoding, $\overline{\overline{D}}^{-1} = \overline{\overline{I}}$, and

$$E = \sigma^2 Tr[I] = N\sigma^2 \tag{3.19}$$

Comparing (3.18) and (3.19), we see that the noise energy is larger for the direct encoding method by the factor N. If the signal levels are the same, therefore, the SNR of Hadamard and Fourier encoding is greater than that of direct encoding by a factor $\sqrt{N}$. Hadamard or Fourier encoding, which excites the whole volume in each encoding step can potentially increase SNR. However, because these volume-encoding methods rely on the excitation of the volume in each TR period, the effective TR is reduced compared to the multi-slice (*i.e.* direct encoding). The Ernst angle (Eq. 1.17), which is a function of effective TR, becomes smaller than that for the multi-slice approach, resulting in a reduction of signal level. The evaluation of SNR for Hadamard and multi-slice encoding should account for the decreased signal level as well as the decreased noise level.

3.3.3 SNR of Hadamard and Multi-slice Encoding

From Eq. 1.16, the MR signal was shown to be;

$$Signal \propto \sin\alpha \frac{(1-e^{-TR\_eff/T1})}{(1-e^{-TR\_eff/T1}\cos\alpha)}, \tag{3.20}$$

where TR_eff is the effective TR, and α is the Ernst angle which maximizes the signal for a given TR_eff and T_1,

$$\alpha = \cos^{-1}(e^{\frac{-TR\_eff}{T1}}). \tag{3.21}$$

Figure 3.7 shows the relation between effective TR and the Ernst angle for gray matter which is the major constituent in activated voxels.

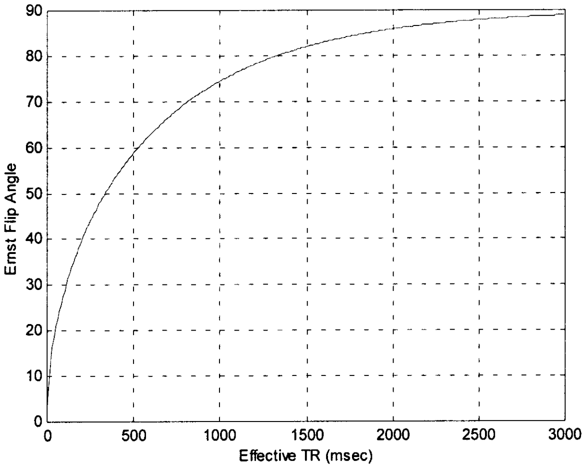

Figure 3.7. Ernst Flip Angle versus effective TR period when T_1=760 msec which is typical for the gray matter.

We computed SNR for two different cases; multi-slice (or direct) encoding assuming single-shot EPI, and Hadamard slice encoding using spatially selective RF excitation. Our computations assume a fixed TR of 100 milliseconds and TE and T_2* of 50 milliseconds. A T_1 of 760 milliseconds, which is typical value for gray matter, was used [100]. Sample results for encoding eight slices ($n_{sl}=8$) are tabulated in Table 3.1. For Hadamard encoding, there is a decrease in noise by a factor of $1/\sqrt{n_{sl}} = 1/\sqrt{8}$. Meanwhile, effective TR for multi-slice approach is longer than that of Hadamard encoding by factor of 8.

Concomitant Ernst flip angle is therefore, greater than that of Hadamard approach (75° versus 30°). The calculated SNR was normalized with respect to the SNR of the multi-slice method for comparison, and we see in the table that Hadamard encoding provides only a slightly higher SNR (7%) than that of multi-slice method.

Case	Effective TR (msec)	FA	Signal Level	$\sqrt{n_{sl}}$	SNR	SNR w.r.t. Case I
Multi-slice	800	~75	0.26	1	0.26	-
Hadamard	100	~30	0.1	2.83	0.28	1.07

Table 3.1 Comparison of SNRs normalized with respect to the multi-slice encoding method for encoding 8 slices. Effective TR, Ernst flip-angle, and number of excitations, $\sqrt{n_{sl}}$, are shown.

Figure 3.8 compares the percentage improvement of SNR for the Hadamard versus multi-slice encoding for different numbers of slices. From the curve, it is seen that the SNR improvement by Hadamard encoding is about 16% compared to the multi-slice approach if 16 slices are encoded and 48% if 32 slices are encoded. In general, then, SNR is improved by Hadamard encoding and the gain increases with the number of slices. However the gain would be much lower than theoretical maximum ($=\sqrt{16}$) that does not take the lowering of flip angle into account. Significant SNR gain over the multi-slice approach can be achieved only when encoding a large number of slices (i.e. > 16).

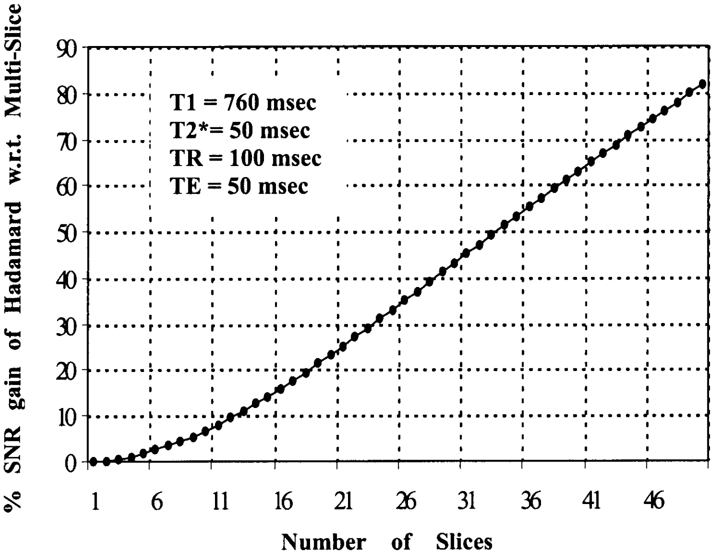

Figure 3.8. Percentage improvement of SNR of Hadamard encoding normalized to the multislice methods with respect to the number of slices. Ernst flip angle was adjusted to the effective TR according to the number of slices. TR= 100 msec, T_1=760 were used in the simulation.

Figure 3.9 shows the percentage improvement of SNR for Hadamard encoding compared to the single-shot multi-slice method assuming fixed temporal resolution (3.2 seconds and 1.6 seconds). The minimum effective TR is set to 100 milliseconds. Therefore, if a multi-slice approach is taken using a single-shot EPI sequence, 32 slices can be encoded in 3.2 seconds and 16 slices can be encoded in 1.6 seconds. The effective TR for Hadamard encoding is equal to the temporal resolution divided by the number of slices that are encoded. As can be clearly seen in Fig. 3.9, there is a point beyond which little SNR advantage is gained by increasing the number of slices that are Hadamard encoded. At roughly 1/4 of the maximum number of slices, over 90% of the SNR advantage due to Hadamard encoding is reached and there is little benefit in further increasing the number of slices.

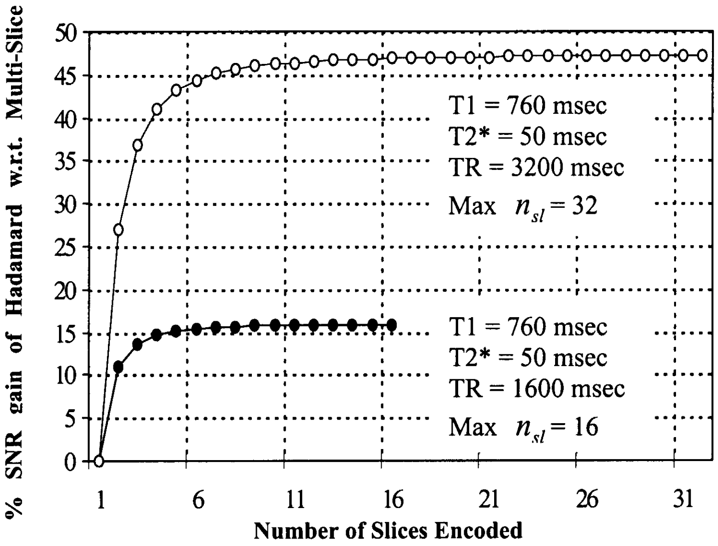

Figure 3.9. Improvement of SNR of Hadamard encoding normalized to the multi-slice method with respect to the number of slices when fixed temporal resolution is used. White and filled circles indicate results for TR of 3200 and 1600 msec respectively.

3.4. Summary

In RF encoding, the shape of RF pulse is manipulated to produce spatial excitation profiles that correspond to functions of non-Fourier encoding bases. A simple matrix representation was used to describe the RF encoding and decoding processes. The importance of the choice of PSF in RF encoding was examined with respect to crosstalk results. The SNR in relation to direct encoding and other orthogonal methods such as Hadamard encoding was analyzed. We found that Hadamard encoding can provide SNR gain over direct multi-slice encoding although a large number of slices (i.e. > 16) must be encoded to achieve any significant gain.

Chapter 4
Multi-resolution Detection of Functional Activation: Theoretical Examination

4.1 Introduction

In fMRI, bimodal hypothesis tests are typically used to create maps of significance levels of functional activation using the fMRI time series for each voxel. The significance of the fMRI activation depends on the amount of BOLD-induced intensity enhancement as well as the noise level, *i.e.*, BOLD contrast-to-noise ratio (CNR). Our proposed multi-resolution adaptive functional MRI method may be justified if the relationship between the BOLD CNR and spatial resolution is favorable for signal detection and zooming. However, it is not completely straight forward how to set the in-plane or through-plane resolution level for initial and intermediate stages of scanning in a functional imaging session.

We were motivated to examine the multi-resolution approach from both theoretical and experimental perspectives addressing BOLD CNR. This chapter presents a theoretical examination of the relationship between BOLD CNR and variable spatial resolution. First, we describe the importance of CNR for the detection of the functional signal. We then present a simplified two-voxel model of the fMRI experiment followed by a more general model. Finally, physiological noise and its effect on BOLD CNR are also analyzed.

4.2 BOLD Signal Detection

Let us start by modeling the data acquisition process in fMRI as a random sampling of data from Gaussian distributions of similar variance but with different means for activated and control states. Thermal noise and physiological fluctuations such as cardiac- and respiratory-related signals cause temporal variations of the signal. Assuming bimodal operation (ON and OFF neuronal states), the mean and standard deviation of the sampled data from each state (S_{Off} and S_{On}) are;

$$S_{Off} : \text{Mean} = \overline{s_{OFF}}, \text{STD} = \sigma_{\text{OFF}} \tag{4.1}$$

$$S_{On} : \text{Mean} = \overline{s_{\text{ON}}} = \overline{s_{OFF}} + \Delta s, \text{STD} = \sigma_{\text{ON}} \tag{4.2}$$

where Δs is the contrast due to the BOLD effect ($\Delta s = \overline{s_{ON}} - \overline{s_{OFF}}$).

In order to reject the null hypothesis of $\overline{s_{ON}} = \overline{s_{OFF}}$ (i.e. hypothesizing that there is no difference between the two states), the difference in mean (Δs) and the standard deviation of the two states are compared. Assuming the noise level of ON and OFF states is same ($\sigma_{OFF} = \sigma_{ON} = \sigma$) and n samples are chosen from each state, a standardized variable, referred to as the Z-score, can be defined as [101];

$$\text{Z}_{\text{s}} = \frac{\overline{s_{ON}} - \overline{s_{OFF}}}{\sigma/\sqrt{n}} = \frac{\Delta s}{\sigma/\sqrt{n}} = \frac{\sqrt{n}\Delta s}{\sigma}. \tag{4.3}$$

A large BOLD contrast, Δs, compared to the baseline noise level indicates that the null hypothesis can be rejected with higher probability. For the same Δs, increasing either the number of samples (n) or decreasing the noise level (σ) favors the rejection of the null hypothesis.

The p-value (i.e., false negative error) for the Z score is defined;

$$p = 1 - \frac{erfc(Z_s / \sqrt{2})}{2}, \tag{4.4}$$

where error function is $erfc(x) = \frac{2}{\sqrt{\pi}} \int_0^x e^{-t^2} dt$.

Note that the expression in Eq. 4.3 is same as that for BOLD CNR ($\Delta s / \sigma$) adjusted to account for the number of trial events ($\sqrt{n}$).

$$CNR = \frac{\Delta s}{\sigma / \sqrt{n}} = \frac{\sqrt{n}\Delta s}{\sigma} = Z_s. \tag{4.5}$$

The BOLD CNR, therefore, is directly related to the significance level represented by p-value. BOLD CNR depends on several factors; the magnitude of BOLD contrast, noise level and the number of data points acquired in the experiment time. In subsequent sections, the factors affecting CNR will be discussed in greater detail.

4.3 Temporal Resolution and BOLD CNR

The effective repetition period, TR, determines the temporal resolution of a fMRI experiment because temporal resolution directly affects the signal level of the image and thus, the concomitant BOLD CNR. As described in Section 1.2.4, the signal magnitude has two components. The first component depends on the ratio of TE time to T_2* and the second is modulated by the effective TR period, flip angle and T_1 of tissue. It was noted that setting $TE \approx T_2^*$ and using the Ernst flip angle, $\cos^{-1}(e^{\frac{-TR}{T1}})$, will maximize the signal (See 1.2.4). The condition $TE \approx T_2^*$ is generally set when using an EPI sequence for fMRI, thus, the component depending on the ratio of TE time to T_2* is not considered further. By substituting the Ernst angle expression for α using Eq. 1.17, Equation 1.16 is rewritten as a function of the ratio between the effective TR and T_1;

$$S \propto \sqrt{1-e^{-\frac{2TR}{T1}}}\,\frac{(1-e^{-\frac{TR}{T1}})}{(1-e^{-\frac{2TR}{T1}})}. \qquad (4.6)$$

Clearly, from Eq. 4.6, the BOLD signal is related to the effective TR period which depends on the encoding method, the volume coverage, and the temporal/spatial resolution of fMRI study.

Volume encoding such as Hadamard or Fourier encoding shortens the effective TR because the whole volume of interest is involved in each TR excitation (Fig. 4.1b) as opposed to the multi-slice approach, where each slice is excited only after all other slices in the volume are excited (Fig 4.1a). The extent of volume coverage and spatial resolution of data acquisition may also influence the effective TR. Let us examine the case of single shot EPI. With the same volume coverage, the slice thickness can be increased to achieve higher temporal resolution (Fig. 4.1c), but a shorter effective TR results. If we reduce the volume coverage while maintaining a fixed spatial resolution, higher temporal resolution is possible but again reducing effective TR (Fig. 4.1d).

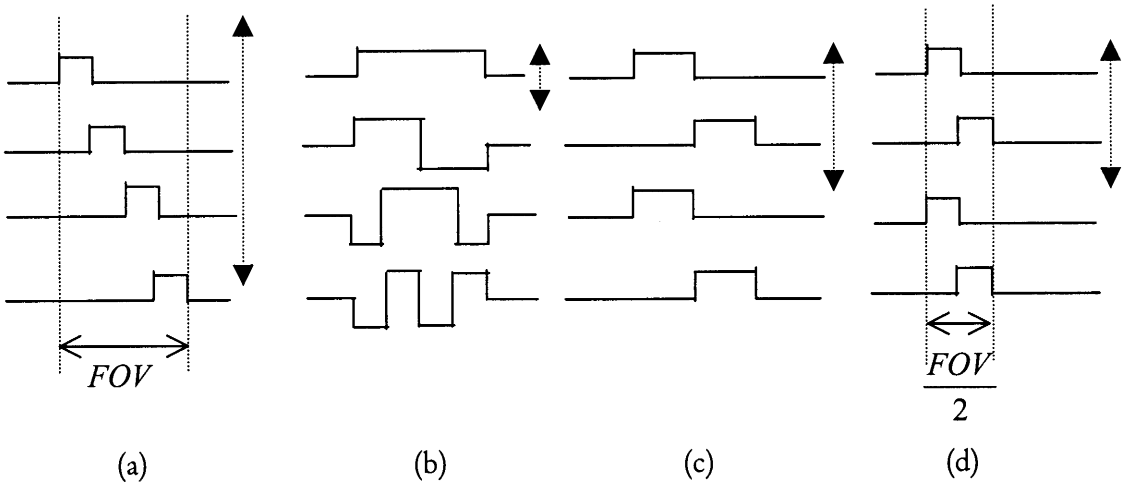

Figure 4.1 Schematic showing relationship between the choice in encoding method and effective TR. (a) direct encoding covering the full FOV, (b) Hadamard encoding of the full FOV, (c) Imaging with thick slices of the full FOV with increase in temporal resolution, and (d) reduced FOV coverage with same slice thickness as (a). The effective TR period is shown by dotted arrows.

4.4 In-Plane Resolution and BOLD CNR

4.4.1 Two-voxel Model

We analyzed the BOLD contrast-to-noise for a simple case where there are only two encoded voxels. Let us assume that all noise is thermal in nature and is therefore uncorrelated spatially and temporally. The encoding combinations of two voxels are shown in Fig. 4.2. From the encoded signal, S^{A+B} and S^{A-B}, estimates for S^{A} or S^{B} can be calculated. This simulates either Fourier or Hadamard encoding. If we use only S^{A+B} for estimation, we simulate the lower resolution imaging case.

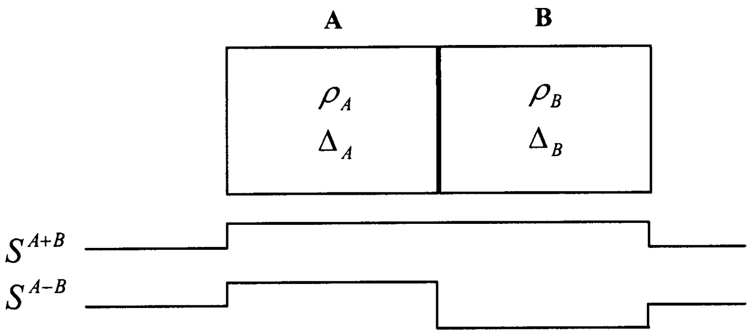

Figure 4.2 Simplified 2-voxel imaging model (A and B). The spatial profiles of the combinations of basic encoding elements are shown (S^{A+B} and S^{A-B}). The mean baseline signal and BOLD contrast are ρ and Δ respectively.

Examining Fig 4.2, we see that,

$$S^{A\pm B} = \rho_A + \Delta_A \pm \rho_B \pm \Delta_B + \eta^{\pm}, \tag{4.7}$$

where $\eta^{\pm}$ is the random thermal noise component associated with each measurement which we assume is a zero mean process with a standard deviation of σ_{η}. The mean baseline signal and BOLD contrast are ρ and Δ respectively. Consideration of physiological "noise" is ignored in this analysis and treated instead in Section 4.6.1.

If only one of the volume elements contains activation (for example, $\Delta_B = 0$ in Eq. 4.7), the signal-estimate of voxel A, which is obtained from a combination of the measurements, S^{A+B} and S^{A-B} is as follows,

$$\tilde{S}^A = (S^{A+B} + S^{A-B})/2 = \frac{2\rho_A + 2\Delta_A + \eta^+ + \eta^-}{2}, \tag{4.8}$$

where η^+ and η^- are the thermal noise components from the measurements S^{A+B} and S^{A-B} respectively.

The resultant CNR becomes;

$$CNR = \Delta_A / (\sigma_\eta / \sqrt{2}) = \sqrt{2}(\Delta_A / \sigma_\eta)\ . \tag{4.9}$$

When S^{A-B} is replaced by zero, simulating reduction of in-plane resolution by k-space truncation and zero-filling, the signal-estimate from voxel A and the associated CNR become;

$$\begin{aligned} &\tilde{S}^A = (S^{A+B} + 0)/2 = (\rho_A + \Delta_A + \rho_B + \eta)/2, \\ &CNR = (\Delta_A / 2)/(\sigma_\eta / 2) = \Delta_A / \sigma_\eta\ . \end{aligned} \tag{4.10}$$

If both voxels A and B have an equivalent magnitude of BOLD activation ($\Delta_A = \Delta_B = \Delta$), the signal-estimate and CNR are,

$$\begin{aligned} &\tilde{S}^A = (S^{A+B} + S^{A-B})/2 = \frac{2\rho_A + 2\Delta_A + \eta^+ + \eta^-}{2} = \rho_A + \Delta + \frac{\eta^+ + \eta^-}{2} \\ &CNR = \sqrt{2}(\Delta / \sigma_\eta)\ . \end{aligned} \tag{4.11}$$

Note that CNR in Eq. 4.11 is the same as Eq. 4.9., the case where only one volume element contains activation.

If there is truncation and zero-filling, the signal-estimate and CNR become,

$$\tilde{S}^A = (S^{A+B} + 0)/2 = (\rho_A + \Delta_A + \rho_B + \Delta_B + \eta)/2 = (\rho_A + \rho_B + 2\Delta + \eta)/2$$

$$CNR = (\Delta_A)/(\sigma_\eta/2) = 2(\Delta_A/\sigma_\eta) \tag{4.12}$$

Analysis using this simple two-voxel model suggests that the BOLD CNR strongly depends on both the spatial dimension of activation and the in-plane resolution. For instance, when the activation is limited to one voxel, reducing in-plane resolution to encompass both voxels actually reduces the CNR by a factor of $\sqrt{2}$ (compare Eq. 4.9 and 4.10). However, when the activation is distributed over both voxels, reducing in-plane resolution has the opposite effect. BOLD CNR is increased by the factor of $\sqrt{2}$ (Compare Eq. 4.11 and 4.12).

4.4.2 In-plane Resolution and BOLD CNR

Based on the simplified 2-voxel model of the previous section, an extended mathematical model was devised to examine theoretically the optimal spatial resolution for maximum BOLD CNR. In order to model the effect of variations of in-plane resolution, truncation in the k-space representation of the BOLD profile was performed, and its effects on noise and BOLD contrast were examined.

Let us define the activation profile as a Gaussian function, $f(x)$, with full-width-at-half-maximum (FWHM) of $\frac{2}{\varepsilon\pi}\sqrt{\ln 2}$ (See Fig. 4.3) so that,

$$f(x) = e^{-(\varepsilon\pi x)^2}. \tag{4.13}$$

The k-space representation of $f(x)$ is also a Gaussian function, $F(k)$, with FWHM of $2\varepsilon\sqrt{\ln 2}$ (Fig. 4.3),

$$F(k) = \frac{1}{\varepsilon\sqrt{\pi}} \cdot e^{-(\frac{k}{\varepsilon})^2}. \tag{4.14}$$

Truncation corresponds to bandwidth-reduction of the k-space representation of the activation profile. Since the truncation in k-space means a filtering of the high spatial frequency content, the spatial profile of the original activation pattern will be affected in addition to the effective spatial resolution. The amplitude of the resulting activation profile is proportional to the area under the k-space profile, therefore, filtering the high frequency region of k-space will reduce the amplitude of the activation profile in image space as illustrated in Fig 4.3.

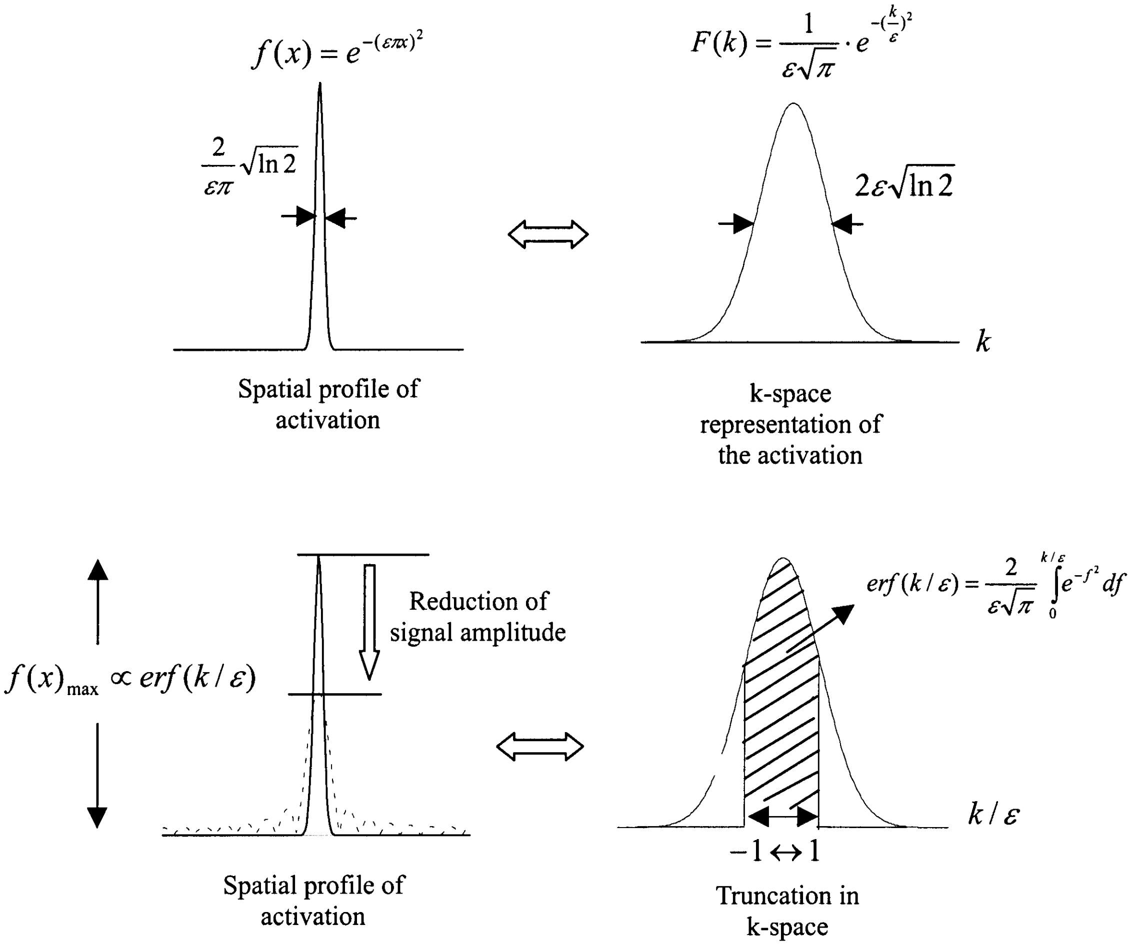

Figure 4.3 Illustration of the signal reduction by simulating reduction in in-plane resolution via k-space truncation.

The degree of amplitude reduction of the Gaussian-shaped activation profile can be obtained analytically from the Error Function, $erf(k/\varepsilon)$ which is equal to the area under the Gaussian shaped function in Eq. 4.14 with a frequency bandwidth $-k/\varepsilon \Leftrightarrow +k/\varepsilon$,

$$erf(k/\varepsilon) = \frac{2}{\varepsilon\sqrt{\pi}} \int_0^{k/\varepsilon} e^{-f^2} df, \tag{4.15}$$

where $0 \le erf(k/\varepsilon) \le 1$.

Assuming σ_η is the noise level at a k-space size of $k/\varepsilon = 1$, k-space truncation alters the image noise level by a factor $\sqrt{k/\varepsilon}$, thus the CNR (assuming fixed TR) is;

$$CNR = \frac{erf(k/\varepsilon)}{\sigma_\eta \sqrt{k/\varepsilon}} \tag{4.16}$$

To find the k/ε that maximizes BOLD CNR, the solution of $\frac{d}{dk}\frac{erf(k')}{\sqrt{k'}} = 0$ is sought, where $k' = k/\varepsilon$.

$$\frac{d}{dk}\frac{erf(k')}{\sqrt{k'}} = \frac{erf'(k')\sqrt{k'} - erf(k')/(2\sqrt{k'})}{k'} = 0 \tag{4.17}$$

which can be rearranged as;

$$erf'(k') = \frac{erf(k')}{2k'}. \tag{4.18}$$

Eq. 4.18 was solved numerically (graphical solution is shown in Fig. 4.4.). Thus, the optimal k-space reduction to produce maximum BOLD CNR is derived,

$$k' = k/\varepsilon \approx 1 \qquad \therefore \; k \approx \varepsilon. \tag{4.19}$$

From our numerical solution, the required k-space bandwidth to maximize CNR corresponds in the breadth of the Gaussian profile in k-space, ε.

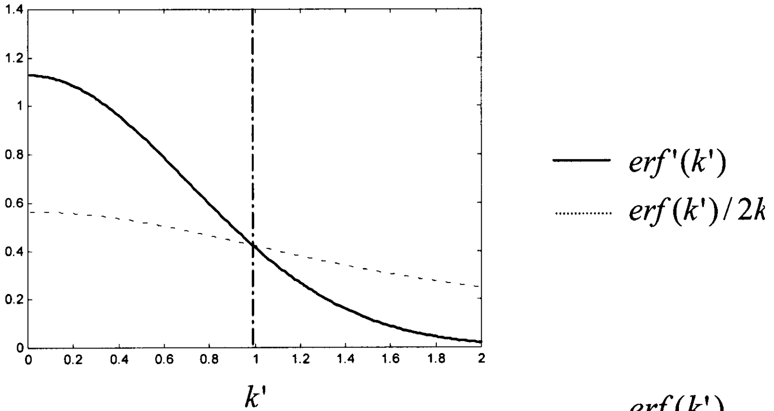

Figure 4.4 Graphical representation for the solution of $erf'(k') = \frac{erf(k')}{2k'}$.

Figure 4.5a shows a plot of normalized BOLD contrast versus k-space size based on the Eq. 4.15. Note that BOLD contrast increases monotonically with increase in k-space size. Fig. 4.5b shows a plot of BOLD CNR versus k-space based on the Eq. 4.16. From the examination of curve of BOLD CNR in Fig 4.5b, we see that CNR reaches a maximum at $k/\varepsilon \approx 1$ as predicted by Eq. 4.19. Thus if the resolution is set too low or too high, less than a maximum CNR is expected.

The previous CNR analysis assumes a fixed number of data acquisitions regardless of the k-space range encoded. If, however, the number of data acquisitions (n) can be increased proportionally with the reduction in k-space, a further factor of $\sqrt{k/\varepsilon}$ is introduced in Eq. 4.16 so that;

$$CNR = \frac{erf(k/\varepsilon)}{\sqrt{k/\varepsilon}} \cdot \frac{1}{\sqrt{k/\varepsilon}} \propto \frac{erf(k/\varepsilon)}{k/\varepsilon}. \qquad (4.20)$$

As shown in Fig 4.5c, CNR is monotonically decreasing function of resolution. The k-space encoding range that produces the maximum CNR in Eq. 4.20 occurs when $k/\varepsilon = 0$. This is somewhat surprising result in that a single encode is enough to generate the maximum CNR, and increasing resolution does not increase CNR.

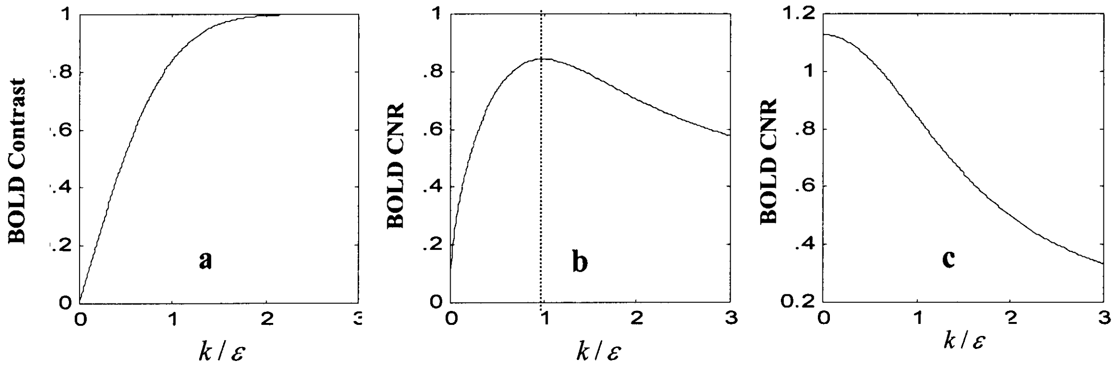

Figure 4.5. The result of functional detection when k-space size is reduced. (a) Normalized BOLD contrast versus k-space size, (b) BOLD CNR versus k-space size. (c) BOLD CNR when the number of acquisitions is increased proportionally with reduction in k-space size.

In summary, increasing k-space size (i.e. resolution) is shown to increase BOLD contrast monotonically (Fig. 4.5a). However, as resolution increases, BOLD CNR increases to a maximum and then decreases. The maximum occurs at a k-space size proportional to the breadth of the activation profile. When the number of acquisition is increased proportionally to reduction in k-space size, the BOLD CNR decreases monotonically with increase in k-space size (resolution).

4.5 Slice Thickness, Size of Activation and BOLD CNR

4.5.1 Two-Slice Model

For the analysis of BOLD CNR in relation to the slice thickness, we used a two-slice model similar to the two-voxel model for variation of in-plane resolution (See Section 4.4.1). Consider two different slices, A and B, as shown in Fig. 4.6. Examples of imaging either slice A alone, or slices A and B together are shown. The mean baseline signal and BOLD contrast are ρ and Δ respectively.

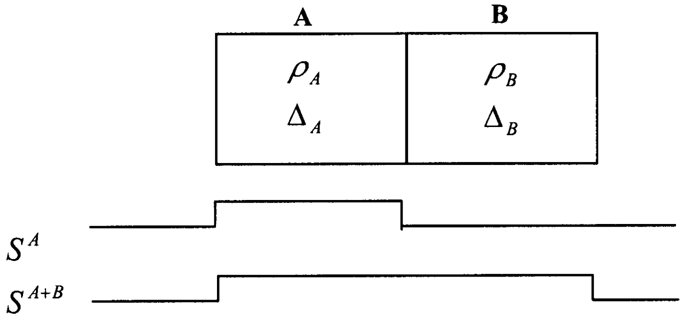

Figure 4.6 Simplified two-slice model of the site of possible activation (A and B). The spatial profiles of the basic encoding elements are shown.

If there is activation in only one of the slices, for example, $\Delta_B = 0$ in (Fig. 4.6), for the first case in Fig. 4.6 where slice A alone is excited,

$$S^A = \rho_A + \Delta_A + \eta, \text{ and } CNR = \Delta_A / \sigma_\eta, \tag{4.21}$$

where η is a thermal noise component with standard deviation of σ_η. In the second case shown in Fig. 4.6. where the slice A + B is excited,

$$S^{A+B} = \rho_A + \Delta_A + \rho_B + \eta, \text{ and } CNR = \Delta_A / \sigma_\eta. \tag{4.22}$$

If both A and B contain functional activation and the magnitude of BOLD contrast is the same in both slices (i.e. $\Delta_A = \Delta_B$),

$$S^A = \rho_A + \Delta_A + \eta \text{ and } CNR_{Thermal} = \Delta_A / \sigma_\eta \tag{4.23}$$

If A + B is excited,

$$S^{A+B} = \rho_A + \Delta_A + \rho_B + \Delta_B + \eta = \rho_A + \rho_B + 2\Delta_A + \eta, \text{ and}$$
$$CNR = (2\Delta_A)/(\sigma_\eta) = 2(\Delta_A / \sigma_\eta) \tag{4.24}$$

Our two-slice model results imply that the relation between the spatial dimension of activation is crucial in determining BOLD CNR. As shown by Eqs. 4.21 and 4.22, as long as the slice includes the site of functional activation, CNR does not change with increasing slice thickness. In case that the functional activation extends beyond the single slice width, CNR increases by a factor of 2 if the slice thickness is increased to contain the activation (compare Eqs. 4.23 and 4.24).

4.5.2 Slice Thickness and BOLD CNR

Based on the previous section using simple two-slice model, a more general model assuming multi-slice single-shot echo-planar-sequence is constructed. First, let us assume that each slice can be encoded within a fixed imaging time ($TR_{\min}$). The effective TR, TR_{eff}, is a function of the number of slices (n_{sl});

$$TR_{eff} = TR_{\min} \cdot n_{sl}. \tag{4.25}$$

If we maintain a constant volume of interest (VOI), the number of slices is inversely proportional to slice thickness $\lozenge_{thk}$,

$$n_{sl} = {}^{VOI}\!/_{\lozenge_{thk}}. \tag{4.26}$$

From (4.25) and (4.26),

$$TR_{eff} = TR_{\min} \cdot n_{sl} = TR_{\min} \cdot ({}^{VOI}\!/_{\lozenge_{thk}}), \tag{4.27}$$

where both $TR_{\min}$ and VOI are constant.

The BOLD signal contrast, ΔS_{act}, can be related to the slice thickness $\lozenge_{thk}$ by substituting TR_{eff} in Eq. 4.27 into Eq. 4.6;

$$\Delta S_{act} \propto \sqrt{1 - e^{-\frac{2TR_{\min} \cdot VOI}{\lozenge_{thk} \cdot T1}}} \, \frac{(1 - e^{-\frac{TR_{\min} \cdot VOI}{\lozenge_{thk} \cdot T1}})}{(1 - e^{-\frac{2TR_{\min} \cdot VOI}{\lozenge_{thk} \cdot T1}})}. \tag{4.28}$$

If the BOLD contrast, ΔS_{act}, is distributed uniformly throughout the volume, the measured BOLD contrast, ΔS, is dependent on both the imaging slice thickness ($\lozenge_{thk}$) and activation thickness , $\lozenge_{act}$, as shown in Fig 4.7.

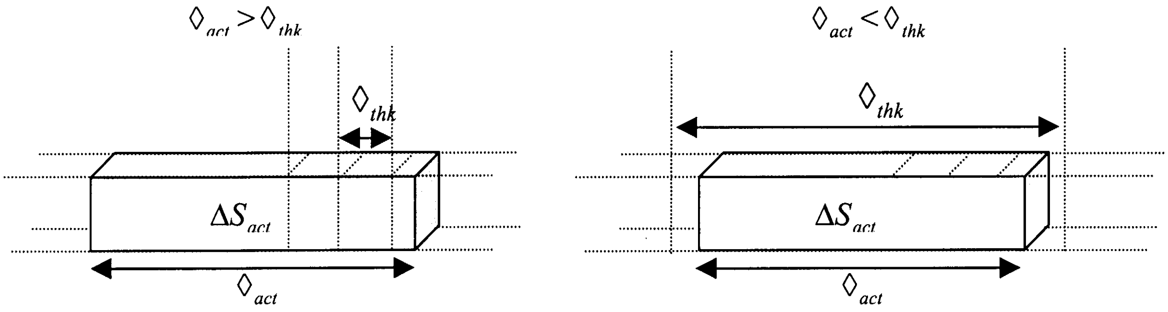

Figure 4.7 Illustration of the extent of activation in through plan direction $\Diamond_{act}$ in relation to the slice thickness, $\Diamond_{thk}$. BOLD contrast, ΔS_{act}, is distributed over the same volume.

We now consider the two cases, $\Diamond_{act} > \Diamond_{thk}$ and $\Diamond_{act} \leq \Diamond_{thk}$.

If $\Diamond_{act} > \Diamond_{thk}$, ΔS increases proportionally with the slice thickness,

$$\Delta S = \Delta S_{act} \times \frac{\Diamond_{thk}}{\Diamond_{act}} \tag{4.29}$$

If $\Diamond_{act} \leq \Diamond_{thk}$, ΔS is constant;

$$\Delta S = \Delta S_{act} \tag{4.30}$$

In addition to BOLD contrast, the number of averaged data acquisitions, n, should also be considered in the CNR calculation (See Fig 4.1c). When a fixed total imaging time, T_{tot}, is used, n is inversely proportional to TR_{eff}.

$$n = \frac{T_{tot}}{TR_{eff}} \tag{4.31}$$

From (4.27) and (4.31)

$$n = \frac{T_{tot}}{TR_{eff}} = \frac{T_{tot} \cdot \Diamond_{thk}}{TR_{\min} \cdot VOI} \tag{4.32}$$

thus, n is directly proportional to $\Diamond_{thk}$.

Eqs. 4.29 and 4.30 and 4.32 were used to calculate BOLD CNR ($CNR = \frac{\sqrt{n}\Delta S}{\sigma}$) for slice thickness vs. activation width. Thermal noise was assumed. TE/ $T_2^*=50/50$ msec and T_1 of 760 msec were used in the calculations. The activation width ($\Diamond_{act}$) was assumed to be evenly distributed over 5.5mm, and the slice thickness ($\Diamond_{thk}$) was varied from 2.5mm to 15.5mm in increments of 1mm. It was assumed that there is minimal susceptibility-related signal loss for a slice thickness of 15.5 mm. It was assumed that a minimum of 50 msec ($TR_{\min}$) is required to encode a single slice. The maximum BOLD percentage change (ΔS_{act}) was set to 5% of the baseline signal level and uniformly distributed over the width of activation. A thermal noise level of $\sigma \approx \Delta S_{act}$, and a fixed VOI of 192-mm were assumed.

The results of the calculations are plotted in Fig. 4.8 assuming a 5.5 mm-thick functional activation width was contained within 192-mm thick volume. Fig. 4.8a is the BOLD contrast (same as the percentage signal change level with respect to the baseline signal intensity). Up to a 5.5-mm slice thickness ($\Diamond_{act} > \Diamond_{thk}$), the BOLD contrast level increases to a maximum at a slice thickness of 5.5mm, However, as slice thickness increases beyond the activation width ($\Diamond_{act} \leq \Diamond_{thk}$), the BOLD contrast decreases due to the reduction in signal level (Eq. 4.28). The BOLD CNR, plotted in Fig. 4.8b, has a similar shape with BOLD contrast since the thermal noise condition was assumed. If the number of acquisitions, n, is increased proportionally to the slice thickness (Eq. 4.32), *i.e.* there is a fixed total imaging time, the large CNR is obtained when the thickest slices are used even when $\Diamond_{act} \leq \Diamond_{thk}$ (Fig 4.8c).

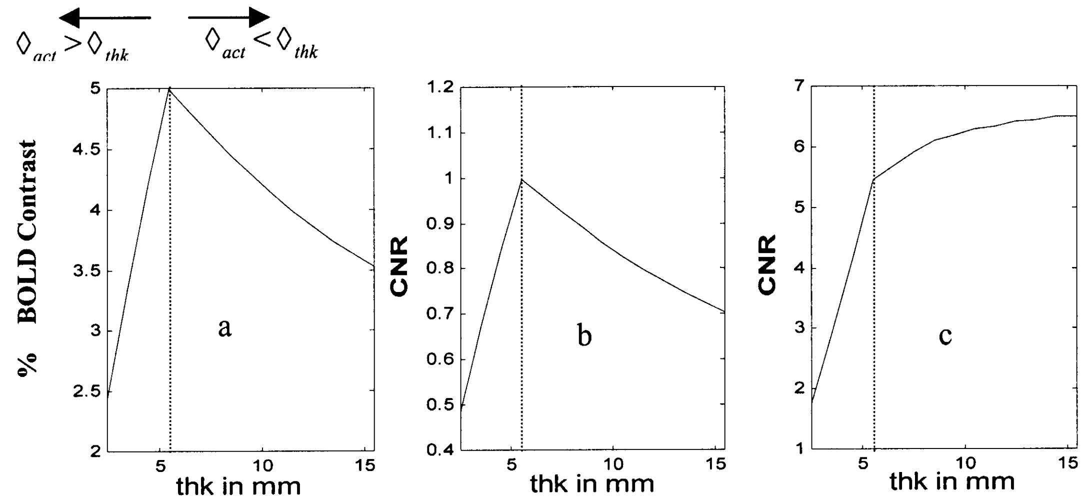

Figure 4.8. BOLD contrast and CNR versus variation in slice thickness assuming BOLD signal change is evenly distributed in a 5.5 mm thick activation width. Total 192-mm coverage was assumed and temporal resolution varies depending on the number of slices excited. (a) Percent change in BOLD signal contrast with variation in slice thickness. (b) CNR vs. slice thickness, (c) CNR vs. slice thickness when the number of acquisitions is increased to maintain constant total imaging time independent of slice thickness.

4.6 Physiological Noise and CNR

The effect of physiological noise on CNR for different encoding bases was analyzed for different activation profiles analogous to the previous section using a simple, two volume-element model. The possible encoding combinations, A+B and A-B are shown in Fig. 4.9, in which we intend to simulate the effect of varying in-plane resolution. The mean baseline signal and BOLD contrast are ρ and Δ respectively.

From Fig 4.2, the signal obtained for the two encodes, ignoring the effect of thermal noise is;

$$S^{A\pm B} = \rho_A + \Delta_A \pm \rho_B \pm \Delta_B + \delta_A \pm \delta_B, \tag{4.33}$$

where δ is the physiological noise component with standard deviation of σ_{phys} with respect to the baseline signal level.

In practice, there is a time difference between encodes S^{A+B} and S^{A-B}, however, we assume that the time-variation of physiological noise is minimal during the short encoding duration as in EPI.

The general expression for the signal estimate when two elements are Fourier or Hadamard encoded is;

$$\tilde{S}^{A} = (S^{A+B} + S^{A-B})/2 = \frac{2\rho_A + 2\Delta_A + 2\delta_A}{2} = \rho_A + \Delta_A + \delta_A \cdot \tag{4.34}$$

If truncation and zero padding is applied, with resultant reduction in spatial resolution, the signal estimate becomes,

$$\tilde{S}^{A} = (S^{A+B} + 0)/2 = \frac{\rho_A + \Delta_A + \rho_B + \Delta_B + \delta_A + \delta_B}{2}. \tag{4.35}$$

Consider first the case where only one of the volume elements contains functional activation, for example, $\Delta_B = 0$ in (4.34),

$$\tilde{S}^{A} = (S^{A+B} + S^{A-B})/2 = \frac{2\rho_A + 2\Delta_A + 2\delta_A}{2} = \rho_A + \Delta_A + \delta_A,$$

$$CNR_{phys} = \Delta_A / \sigma_{phys} \cdot \tag{4.36}$$

With truncation and zero padding, the signal estimate becomes,

$$\tilde{S}^{A} = (S^{A+B} + 0)/2 = \frac{\rho_A + \Delta_A + \rho_B + \delta_A + \delta_B}{2} \ . \tag{4.37}$$

If δ_A and δ_B are uncorrelated, the CNR is the same as that obtained assuming thermal noise in Sec. 4.4.1. However, if δ_A and δ_B are correlated, the variance of $\delta_A + \delta_B$, is the same as that of the single variable $2\delta_A$, and is $4\sigma^2_{phys}$. The CNR is therefore dependent on the spatial characteristics of the physiological noise component;

$$CNR_{phys} = (\Delta_A / 2)/(\sigma_{phys}) = \frac{1}{2}(\Delta_A / \sigma_{phys}) \qquad \text{for}\, \delta_A = \delta_B = \delta \tag{4.38}$$

$$CNR_{phys} = (\Delta_A / 2)/(\sigma_{phys} / 2) = \Delta_A / \sigma_{phys} \qquad \text{for}\, \delta_A = \delta, and\ \delta_B = 0 \tag{4.39}$$

Consider another case where both A and B contain functional activation with the same magnitude of BOLD contrast ($\Delta_A = \Delta_B = \Delta$),

$$\tilde{S}^A = (S^{A+B} + S^{A-B})/2 = \frac{2\rho_A + 2\Delta_A + 2\delta_A}{2} = \rho_A + \Delta_A + \delta_A, \text{ and}$$

$$CNR_{phys} = \Delta_A / \sigma_{phys}. \tag{4.40}$$

In the case of truncation and zero-padding,

$$\tilde{S}^A = (S^{A+B} + 0)/2 = \frac{\rho_A + \Delta_A + \rho_B + \Delta_B + \delta_A + \delta_B}{2} = \frac{\rho_A + \rho_B + 2\Delta + \delta_A + \delta_B}{2} \tag{4.41}$$

and for CNR ,

$$CNR_{phys} = \Delta / \sigma_{phys} \qquad \text{for } \delta_A = \delta_B = \delta \tag{4.42}$$

$$CNR_{phys} = \Delta / (\sigma_{phys}/2) = 2(\Delta / \sigma_{phys}) \qquad \text{for } \delta_A = \delta, and\ \delta_B = 0. \tag{4.43}$$

A general trend of the relationship between the size of activation and the size of area affected by physiological noise can be seen from the results above. When the size of activation is greater in extent than the areas that are affected by physiological noise, there is an increase in CNR if we reduce spatial resolution (Eqs 4.40 and 4.43). However, when the size of activation is smaller than that the area affected by physiological noise, reducing spatial resolution decreases CNR (Eqs. 4.36 and 4.38). If the size of activation is equal to that due to physiological noise, the CNR is not affected by changing resolution (Eqs. 4.36, 4.39 and 4.42).

4.7 Summary

In this chapter, we first showed that the BOLD CNR is an important parameter, which directly relates to the detection of functional signal assuming Gaussian distribution with same variances for signals obtained from activated and control tasks. Temporal resolution is also important because it directly affects the signal level of the image, and concomitant CNR.

We used a simplified two-voxel model to examine the spatial resolution with respect to CNR in both in-plane and through-plane resolution, and extended the analysis to include the more general cases. Our analysis based on this simple two-voxel model suggests that the dimensions of the activation and spatial resolution affect BOLD CNR in that CNR is maximized when the spatial resolution is matched to the size of activation. Further analysis, simulating functional activation with a 1-dimensional Gaussian shaped profile showed that the maximum CNR is achieved for in-plane encoding when the k-space range in imaging matches the breadth of the k-space profile of activation. In the through-plane direction, the slice thickness should be adjusted to equal to the size of activation in order to obtain maximum CNR. If it were possible to increase the number of acquisitions proportionally to increased slice thickness, we showed that a single slice covering the whole FOV would give the maximum CNR.

A two-voxel model was also used to examine BOLD CNR when noise is predominantly physiological. We showed that when the size of activation is greater in extent than the areas that are affected by physiological noise, there is an increase in CNR if we reduce spatial resolution. However, when the size of activation is smaller than that the area affected by physiological noise, reducing spatial resolution decreases CNR. CNR is not influenced by changing resolution if the size of activation is equal to the size of areas affected by physiological noise.

Chapter 5

Multi-resolution Detection of Functional Activation: Experimental Data

5.1 Introduction

From the previous chapter, our analysis showed that maximum detection of functional activation as quantified by the BOLD CNR, depends on the relationship between the size of the activation and spatial resolution of the imaging. We were motivated to investigate and confirm this analysis in functional MRI sessions using simple sensorimotor paradigms. In this chapter, BOLD contrast as well as BOLD CNR with respect to variation of in-plane and through-plane resolution is investigated. We simulate the variation of in-plane resolution by truncating k-space and zero-padding before reconstructing images. Multiple fMRI sessions were performed and we varied the slice thickness for each session. Additionally, to further examine the relationship between spatial resolution and the activation profile, a single activation profile of known size and location was simulated. Finally, the physiological noise component, which affects the BOLD CNR, was measured as a function of slice thickness, and a simple model was constructed to relate physiological noise and spatial resolution.

5.2 Materials and Methods

Two male subjects (aged 28 and 48) gave written consent prior to the scan sessions according to institutional IRB. All the experiments except the measurement of physiological noise were performed on a 1.5T MR system (GE Medical, Milwaukee, WI) with a standard gradient and quadrature bird-cage head coil for RF transmission and detection. For the measurement of physiological noise, a single-shot EPI sequence was used in a MR system with dedicated hardware for echo-planar imaging (Signa LX, GE Medical).

In order to restrict head motion, a vacuum-pillow (S&S X-ray Products, Brooklyn, NY) was molded around the subject's head. This head immobilization was used for most experiments presented in this thesis. Image encoding in the slice-select direction was performed using combinations of 3 mm-thick planes as the basic volume elements with RF pulses designed to provide uniform saturation over the volume in order to reduce the in-flow effect (A detailed discussion of the in-flow reducing RF pulse can be found in Chapter 6). For imaging on the system with standard gradients, an interleaved EPI (IEPI) sequence [102] was adapted for RF encoding in the slice-select-direction (Chapter 6). Spin-Echo T_1-weighted sagittal slices (7-12 contiguous slices, TE/TR 10/700 msec, 5mm thickness, 1 NEX, matrix size of 128x256, 24x24 cm FOV) were acquired for anatomical localization and to provide reference T1-weighted anatomical images.

5.2.1 Data Processing

All data-processing and simulations were done using the Matlab programming environment (Mathworks, Inc. Natick, MA). In order to find the relation between spatial resolution (both in-plane and through-plane) and CNR, the distribution of CNR in selected volumes-of-interest (VOIs) was computed. BOLD contrast (ΔS) was calculated by taking the difference in means of signal in stimulus and non-stimulus phases for each pixel, and representing it as a percentage value with respect to the baseline signal. The standard deviation of the noise was estimated by computing the mean of the standard deviation of the signal computed separately for the two phases. The signal magnitude was not normalized in order that we could compare the relative CNR at different resolutions.

Histograms for CNR and percentage BOLD contrast for selected ROI's were generated. The quantification of the BOLD CNR among voxels at different slice-thickness required more than a simple count of pixels because each pixel represented a different volume depending on slice thickness. Therefore, histograms were generated from the ratio of number of pixels to the total number of pixels within the volume of interest for both percentage BOLD contrast and CNR.

5.2.2 Variation of In-plane Resolution

A preliminary low-resolution functional study with a left hand-clenching task was performed for each volunteer (FOV 192 x 192mm, 8 contiguous slices, 3mm slice thickness, TE/TR=45/100msec, 64 x 64 matrix, and flip angle 60). Seven sets of 11 images were acquired during alternating epochs of control and task performance. After identifying a slice showing significant activation ($p < 0.001$), high-resolution functional mapping was performed for a single slice. Data was acquired in twelve shots, each with ten individually phase-encoded echoes, interleaved to fill a 128 x 120 k-space matrix for each image. Nominal in-plane resolution was 1.5mm. Flip angle and slice thickness were set at 40° and 3mm respectively. One image was acquired every 2.4 seconds. Fifteen sets of 12 images each were acquired during alternating epochs of control and task performance (left hand clenching) periods. To reconstruct images at different resolution, the k-space data was truncated to 8 different resolution levels (truncated square k-space size: 112, 96, 80, 64, 48, 32, and 16) and zero-filled to 128 x 128. The data was then inverse Fourier transformed and magnitude images were obtained.

5.2.3 Variation of Slice Thickness

In order to evaluate the multi-resolution approach in the through-plane direction, three separate functional MRI sessions were performed using the same motor task (right hand clenching), but changing the slice thickness for each session. A 64 x 64 k-space matrix was filled with echo data from four shots each with sixteen individual phase encoding steps. Each image was acquired in 3.6 seconds (effective TR = 900 msec, TE=45 msec, flip angle = 60°). FOV was set to 192mm x 192mm, giving an in-plane resolution of 3mm. Fifty image sets were obtained for each study with 3 control periods interleaved with 2 periods of task activation. Axial slices were prescribed to image most of the primary motor areas that are inferior to the superior apex of precentral gyrus in sagittal anatomical images. Slice thickness was set at 3mm, 6mm, and 12mm for these functional studies while the subject stayed motionless in the scanner. In each session, 8 slices were encoded to maintain the same temporal resolution. Images were prescribed in order to resolve the top two 12mm-thick superior slices into four 6mm-thick and subsequently into eight 3mm-thick slices (Fig 5.1).

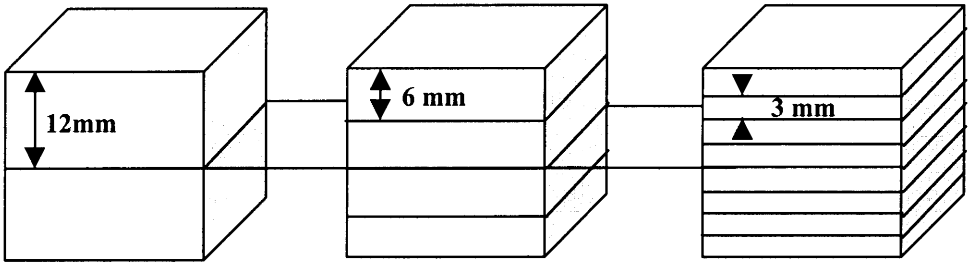

Figure 5.1 Experimental design in varying slice thickness (12mm, 6mm and 3mm) for the same volume

5.2.4 Simulation of Multi-resolution Detection

To further examine the relationship between in-plane resolution and activation, a single activation profile was simulated in a high-resolution image. A 128 x 128 anatomical image (128 mm FOV) was used to simulate the baseline states. A single, 2 dimensional activation profile (Gaussian shape with FWHM corresponding to 6.6 mm, maximum magnitude adjusted to 5% of the baseline image intensity) was overlaid on the approximate location of supplementary motor area. A time series of images was then constructed simulating five epochs each of 10 images with alternating control and task period. Each image in the simulated time series of data was transformed to k-space, and random noise with a standard variation approximately equal to the BOLD contrast level was added to the simulated k-space data. To reconstruct images at different resolution, the k-space data was truncated to ten different resolution levels (truncated square k-space size: 128, 112, 96, 80, 64, 48, 32, 16, 8 and4) and zero-filled back to 128 x 128. The data was then inverse Fourier transformed to make magnitude images.

5.3. Results

5.3.1 Variation of In-plane Resolution

Figure 5.2a shows a functional map obtained at the highest in-plane resolution levels (1.5mm). The activated pixels with high significance ($p < 0.001$) were overlaid on anatomical images. For further analysis, we selected an ROI of 24 by 24 pixels containing activation. The percentage of BOLD contrast (ΔS) is represented by the gray-level image in Fig. 5.2b. Note that the BOLD contrast intensity decreases as the in-plane resolution is lowered. The histogram of BOLD contrast in Fig. 5.2d for different resolutions indicates that, at higher resolution, the distribution of activated pixels broadens to include a greater BOLD contrast.

Figure 5.2c shows gray-level images of the CNR at different levels of spatial resolution. As evidenced from these images, CNR levels do not uniformly decrease as the resolution lowered in contrast to the behavior for percentage BOLD contrast. For example, for k-space truncation at k= 48 or 32, there is a more definite spatial pattern and higher intensity in the CNR map compared to the high resolution map. Further, the histogram in Fig. 5.2e shows an opposite trend to that seen in Fig 5.2d. There are more pixels with high CNR (increased histogram breadth) for the low resolution case compared to the results obtained from the high-resolution data. We should also observe that the shape of the original activation significantly changes due to the filtering effect. At the lowest resolution (k=16), the activation morphology, apparent at higher levels of resolution, is lost.

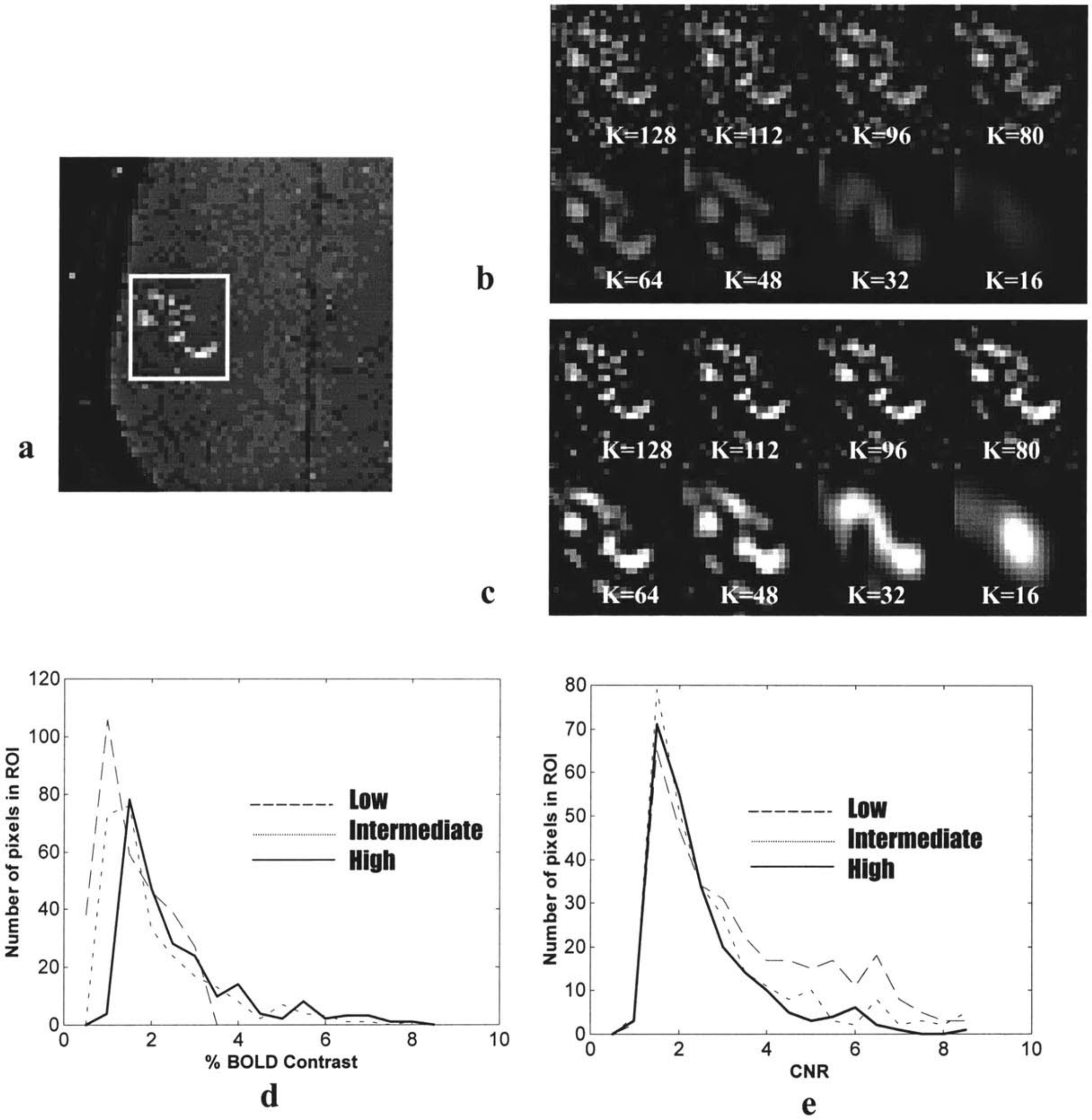

Figure 5.2. (a) Activation map for $p < 0.001$ (overlaid on anatomical images) with box showing ROI for analysis, (b) Percentage BOLD contrast in an ROI for each of the multiple levels of resolution at 8 levels of resolution from 1.5 mm down to 12mm (truncated square k-space size: 112, 96, 80, 64, 48, 32, and 16 from top left to bottom right). (c) Set of CNR maps from fMRI data reconstructed at 8 levels of resolution from 1.5 mm down to 12mm. (d) Histogram showing distribution of percentage BOLD contrast in the ROI using the results at high resolution of 1.5mm (solid line), intermediate resolution of 6mm (dotted line), and low resolution of 12mm (dashed line). (e) Histograms showing distribution of CNR for activated pixels in the ROI using the results at high resolution of 1.5mm (solid line), intermediate resolution of 6mm (dotted line), and low resolution of 12mm(dashed line).

Although the activation in the above experiment clearly does not have the simple Gaussian shape as modeled in Section 4.4.2, we wished to see if the experimental results could be compared at least qualitatively with the theoretical prediction shown in Fig 4.5. The mean CNR and percentage BOLD contrast from pixels in the ROI are plotted versus different k-space sizes (Fig 5.3). Note that the result is qualitatively similar to that obtained using the model in Section 4.4.2. As in Fig. 4.5, the percentage BOLD contrast in the experimental results also increases as k-space size increases (Compare to Fig 5.3). The CNR reaches a maximum around a k-space size of 32 (Fig 5.3). This is also evident in the gray-level intensity maps of CNR (Fig 5.2c). For this specific sensorimotor task, the activated sensorimotor area is distributed over a significantly larger area than a single pixel. Higher in-plane resolution is clearly not necessary in this case if the primary goal of the fMRI session is to detect the existence of activation within the slice.

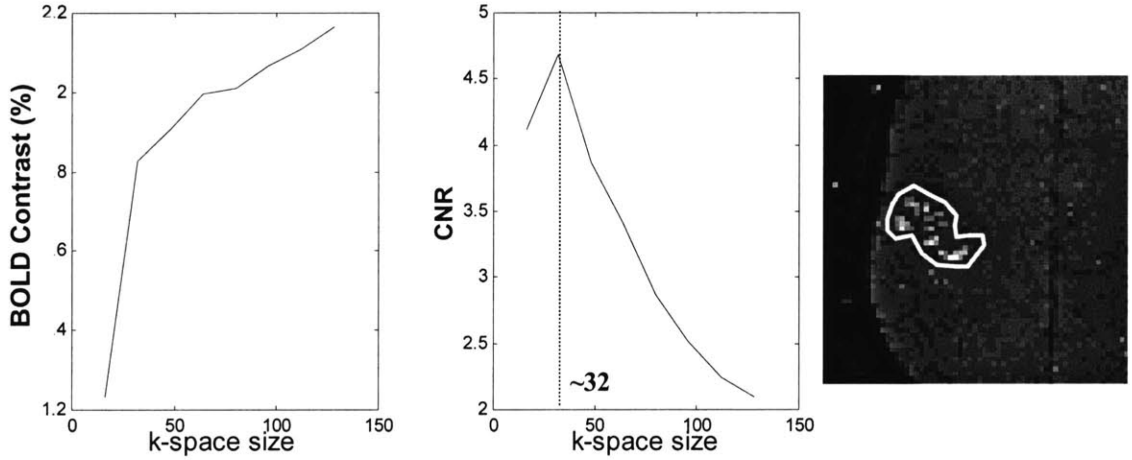

Figure 5.3 The average BOLD enhancement (%) and CNR in the ROI (shown in the right column) for variation in k-space size.

5.3.2 Variation in Slice Thickness

ROI (Sensorimotor area, all 2 by 2 pixels) analysis for different slice thickness (12mm, 6mm, and 3mm) was conducted and the results are summarized in Fig 5.4. ROI 1 and 2 are from a 48 year-old male, and ROI 3 is from a 28 year-old male. ROI's were chosen based on the regions with significant activation ($p < 0.001$) at 12mm-thick slices. As shown in Fig. 5.4, the mean signal change, noise level and CNR ratio are presented for ROI's at each of three slice-thicknesses. The results from the ROI analysis are presented as three vertically arranged rows of boxes where each row represents the results of ROI-analysis at a different slice thickness. The mean BOLD signal change and standard deviation of noise is written within each box. The CNR is the number written under each box.

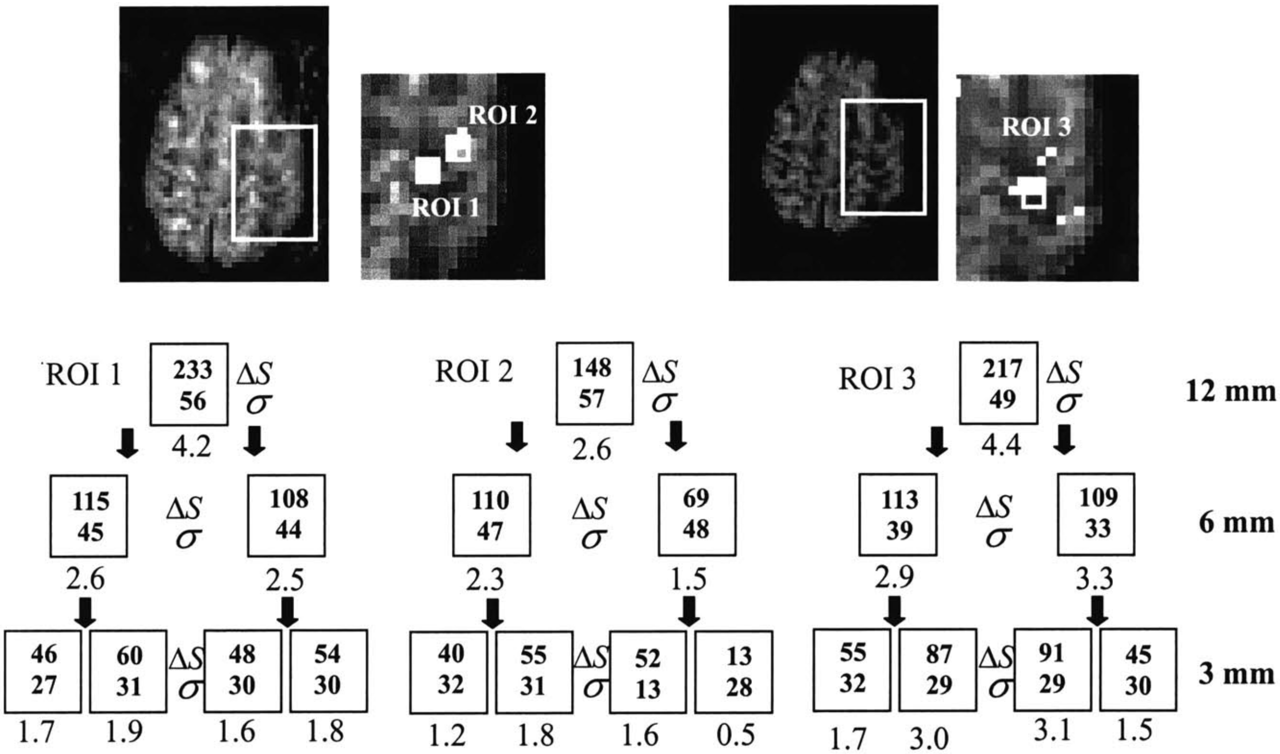

Figure 5.4 ROI (Sensorimotor area, all 2 by 2 pixels) analysis of fMRI results at different slice thickness (12mm, 6mm, and 3mm). ROI 1 and 2 were from a 48 year-old male, and ROI 3 was from a 28 year-old male. ROIs were identified from the data acquired with a 12mm thick slice ($p < 0.001$). Slice positions in the experiment were arranged so that one 12mm slice includes two 6mm slices and the two 6mm slices includes four 3mm thick slices. The slice thickness that corresponds to the ROI analysis is shown in the right column horizontally. (Yoo et al., "Real-time Adaptive Functional MRI", *Neuroimage*, 10:596-606, Copyright © Academic Press. Inc. Reprinted by permission of Academic Press. Inc.)

There are three major findings from the ROI analysis. They are: (1) BOLD signal change is additive with increasing slice thickness, (2) noise increases with increasing slice thickness, and (3) CNR increases as slice-thickness increases.

Our first major observation was that the BOLD signal appeared to be additive in the sense that the sum of the BOLD signal changes in two thin slices was approximately equal to the BOLD signal change in a thick slice covering the thinner slices. For example In ROI 1 of Fig. 5.4, the mean signal change of 233 in the 12mm-thick slice is approximately the sum of BOLD signal in ROI 1 for the two 6mm slices (115+108=223), and subsequent slices shows the additive trend from 3mm to 6mm slices (46+60=106, and 48+54=102). Other ROI's showed a similar trend.

Our second major observation from the ROI analysis is a tendency toward increased noise level as slices get thicker. This trend is especially evident when we look at the mean noise level for all ROI's in a sensory area as detailed in Table 5.1. We measured the noise of ROI's in the background outside of the head, and note that, in contrast to areas within the brain, the noise level was constant regardless of the variation in slice thickness.

The third major observation was that CNR increased or remained constant with increasing slice thickness. This trend is further evaluated in Section 7.3.2. Problems with loss of CNR due to partial volume effects or susceptibility dephasing were not evident at the slice thicknesses and location we used.

Location	Thickness	Mean noise
Sensorimotor ROI	12 mm	53.6
	6mm	40.7
	3 mm	30.0

Table 5.1 Averaged noise measured from all sensorimotor ROI's. There is a trend of increasing noise level with increasing slice thickness.

5.3.3 Simulation of Multi-resolution Detection

A set of activation maps for $p < 0.001$ (overlaid on anatomical images) on simulated data at 10 levels of resolution from 1 mm down to 48 mm are shown in Fig. 5.5a. Figures 5.5b and 5c show the histograms of percentage BOLD contrast and CNR for a ROI (circle). As evident in Fig. 5.5, the activation was not visible at the highest spatial resolution. The activation starts to be visible only around k=48 and is most prominent around k=16. When k is only 4, the activation was still visible, however, the gray-scaled intensity map of p-values is visibly lower compared to k=16. When we look at the histograms for the percentage BOLD contrast (Fig 5.5b) and CNR (Fig 5.5c), at higher resolution, the distribution of activated pixels in the ROI broadens to include a higher proportion of pixels with a large percentage change. As seen in the experimental data, however, the opposite trend occurs for the CNR histogram. For CNR, the histogram broadens to include higher CNR at lower resolution.

In Fig. 5.6, The mean CNR and percentage BOLD contrast from pixels in the ROI are plotted against different k-space sizes. The result is similar to the theoretical results shown in Fig. 4.5, that is, the percentage BOLD contrast increases as the k-space size increases. CNR, however, reaches a maximum, and then declines. The maximum CNR in this case occurs when the spatial resolution associated with this k-space cut-off is approximately equal to the size of the modeled activation (~7 mm).

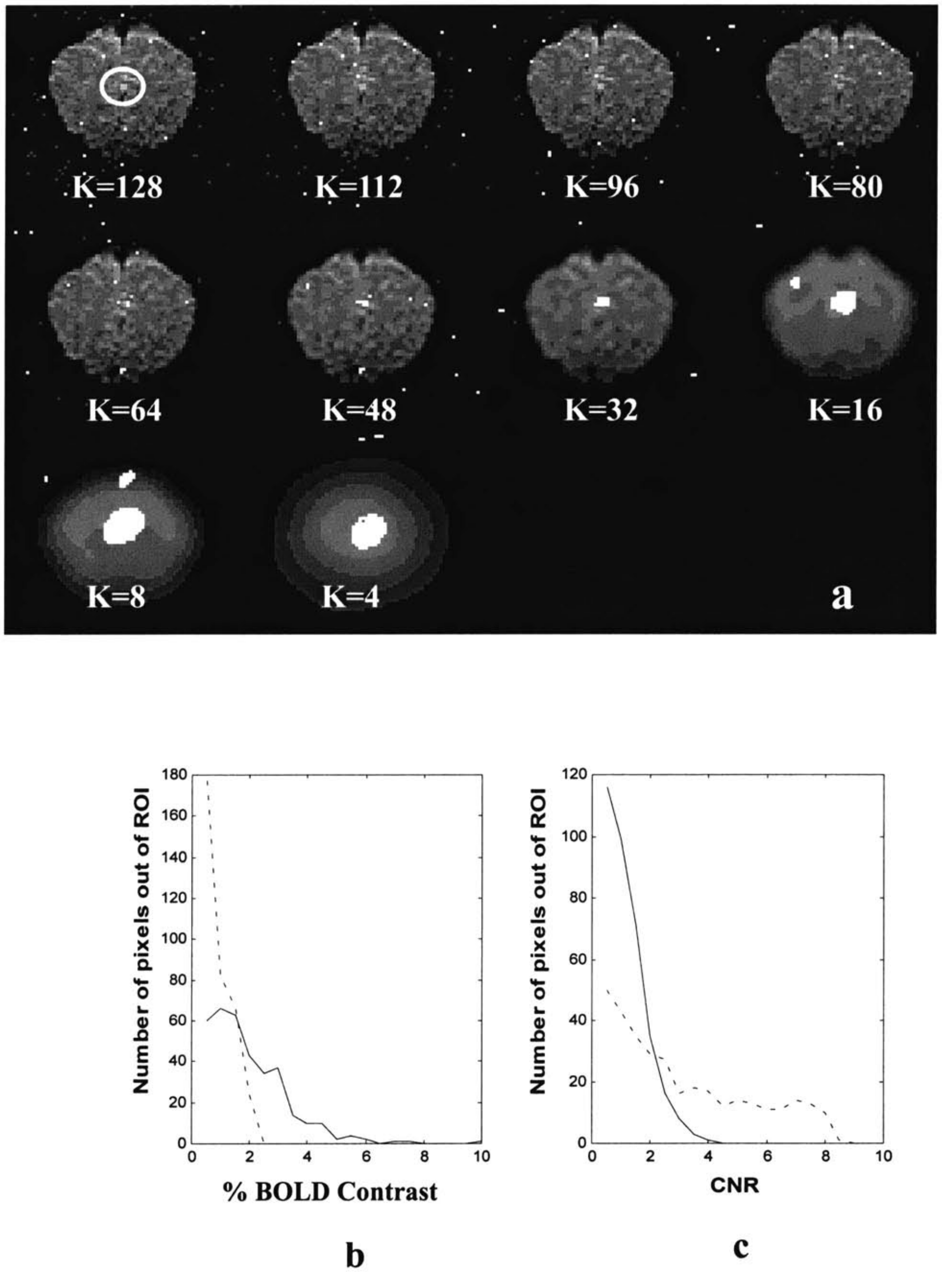

Figure 5.5. (a) Set of CNR maps for $p < 0.001$ (overlaid on anatomical images) of simulated fMRI data reconstructed at 10 levels of resolution from 1 mm down to 32 mm. ROI is identified as white circle. (b) Percentage BOLD change in an ROI for each of the multiple levels of resolution with spatial resolution of 1.0mm (solid line) and 8 mm (dashed line). (c) Histograms showing distribution of CNR in the ROI with different resolution, 1.0mm (solid line) and 8 mm (dashed line).

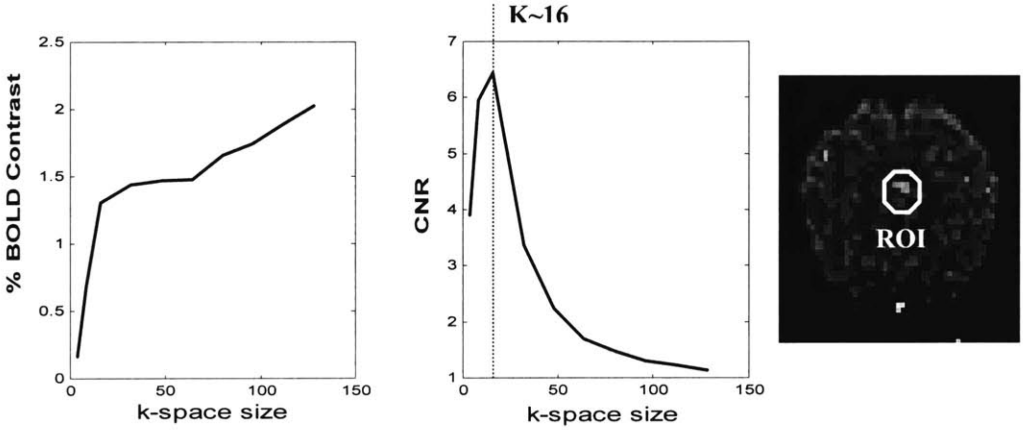

Figure 5.6 Average BOLD percent enhancement and CNR within the ROI versus k-space size.

5.3.4 Measurement of Noise Level

As discussed in Section 5.3.2, we observed a tendency toward increased noise level as slices get thicker. We hypothesized that this is due to the presence of cardiac, respiratory and other physiological variations that scale with increasing slice thickness compared to the thermal noise, which does not. We were, therefore, motivated to further measure image noise while varying slice thickness.

Noise level was calculated from a sequence of 270 images at different slice thickness, from 3.0mm to 7.0mm in increments of 0.4mm using scan parameters of TR/TE/flip angle =200/50/40°. The volunteer was at rest during the scan session. The k-space matrix was 64 x 64 and FOV was 190mm (in-plane resolution ~3mm). A pairwise subtraction of each image set in the time series with respect to the first image set was performed to test for significant global head-motion. The data with significant motion was excluded from further analysis. Background noise as well as the mean signal level from gray and white matter ROIs were measured. Gray and white matter ROIs were selected randomly in the various anatomical compartments based on the T_1-weighted image of 7.0mm-thick slice.

In general, we noted that the image noise measured from the white matter ROI's was constant over the slice thickness. In gray matter ROI's, we found that, in general, the physiological noise increased with increasing slice thickness as noted also in Section 5.3.2. The trend was roughly linear in a number of the gray matter ROI's and extrapolated physiological noise in these ROI's was close to zero for zero slice thickness. This is expected because no physiological noise should be evident for zero volume. In other gray matter ROI's, however, the linear trend of increasing physiological noise with increasing slice thickness was not observed over the whole range of slice thickness measured. In some ROI's, for example, we observed a roughly linear trend over only half the range of slice thickness and no variation over the other half. We believe that such variability of noise level behavior among different gray matter ROI's is due to the inhomogenous nature of brain anatomy where very different types of tissues with respect to physiological noise components may be present within a single voxel.

5.4 Summary

In this chapter, we reported experimental data on the variation of BOLD contrast and CNR with variable in-plane resolution and slice thickness to validate earlier analytical results from Chapter 4. In addition, to further validate the results with respect to the relationship between spatial resolution and the activation profile, a single activation profile was artificially created and we simulated fMRI processing at different in-plane resolutions.

For the given sensorimotor task and from the artificially created Gaussian-shaped activation profile, we found that high in-plane spatial resolution is not necessary or even desirable to detect the presence of the activation within a slice. The histogram of BOLD contrast for different in-plane resolutions, from both experimental data and simulation, indicates that, at higher resolution, the distribution of activated pixels broadens to include a higher BOLD contrast. However, the BOLD CNR, which is the parameter directly relevant for the functional signal detection, showed the opposite trend in that there are more pixels with high CNR at reduced k-space size. The ROI analysis showed that the percentage BOLD contrast increases as k-space size increases, however, BOLD CNR reached certain maximum at reduced k-space size. From the simulation of the artificially created Gaussian-shaped activation profile, we found the maximum CNR occurs for resolution matching the breadth of the k-space profile of activation.

When we varied slice thickness, we found that up to about 12 mm slice thickness could be used in practice without introducing significant susceptibility-related signal loss. The ROI analysis on the activated regions showed that CNR level was increased or remained constant while the BOLD contrast was additive across the slice thicknesses. We found that our experimental results were consistent with those we modeled in Chapter 4. We were therefore able to validate our previous analytical model on BOLD contrast and CNR in relation to the variation of the spatial resolution.

Chapter 6
Functional MRI Using RF Encoding

6.1 Introduction

Spatially selective RF encoding was introduced in Chapter 3, and theoretical and experimental investigations regarding multi-resolution approach in fMRI were described in the two previous chapters. Based on the results of the previous chapters, we have shown that RF encoding provides the flexibility necessary for adaptive multi-resolution zooming and based on maximization of CNR, this approach is reasonable for application in functional MRI. The feasibility of using RF encoding for functional MRI still needs to be shown.

In this chapter, RF encoding in the slice-select direction was implemented on a conventional MR system to demonstrate the flexibility to selectively encode non-contiguous slices distributed throughout the brain. The implementation details and fMRI results on simple sensorimotor and visual paradigms are reported in this Chapter. We also aimed to explore the possibility of Hadamard encoding in slice-select direction. The spatial selectivity of RF encoding was also exploited for in-flow reduction by applying uniform degree of excitation over the imaging volume. Results were compared with those from a separate functional session without in-flow reducing RF pulses.

6.2 Materials and Methods

A study consisting of two sets of functional MRI experiments using different RF excitation schemes was conducted. In the first set of experiments, the excited volumes were slices, comprised of combinations of thin planes as the basic volume elements. No further encoding of these slices was done (*i.e.* $\overline{\overline{T}}$ in Eq. 3.10 was the identity matrix). We refer to this as 'multi-slice imaging'. In second set of experiments, these slices were Hadamard encoded (*i.e.* $\overline{\overline{T}}$ in Eq. 3.10 was a Hadamard matrix). In the formalism described in the Section 3.1.1, Eq. 3.10, K=96x96, M=96, N=4 or 5, $\overline{\overline{T}}$ was either a 4x4 Hadamard matrix for Hadamard encoding or the 5 x 5 identity matrix for multi-slice imaging.

Six subjects ranging in age between 24-47 were studied using the RF encoding method. All six subjects, 3 subjects (1 female and 2 males) for the first sets of experiments and 3 subjects (1 female and 2 males) for the second set, gave written informed consent prior to the fMRI study. Spin-Echo T_1-weighted sagittal slices (7-12 contiguous slices, TE/TR 10/700 msec, 5mm thickness, 1 NEX, matrix size of 128x256, 24x24 cm FOV) were acquired for anatomical localization. Contiguous coronal slices with 7.5mm thickness covering from precentral gyrus to occipital cortex were imaged with same image parameters to provide T_1-weighted anatomical images. In order to visualize large blood vessels, flow-sensitive gradient echo imaging (TE/TR, 20/50 msec, Flip angle 30, 96x96 matrix size on 24x24cm FOV, 1NEX) was performed.

An Interleaved EPI (IEPI) sequence [102] was adapted for non-Fourier encoding in the slice-select-direction for functional study. Each profile was a combination of thin planes of 2.5 mm thickness which were the basic volume elements for these experiments (as introduced in Section 3.3.1 and Fig. 3.6). The maximum flip angle was set at 30° to insure validity of the linear systems assumption (Flip angles larger than 30 ° can be used if a special method of RF pulse design is employed [104].) The echo data from each successive shot were interleaved to fill a 96x96 k-space matrix. Twelve echoes per shot were phase-encoded requiring 8 shots per matrix acquisition. The FOV was 24cm, giving an in-plane resolution of 2.5mm. With TR of 100 msec, 5 slices could be encoded in 4 seconds. The effective TE of the sequence was 50 msec.

6.2.1 Multi-Slice Imaging

RF pulses for encoding were prepared by Fourier transforming the desired spatial profiles (from C1 to C5) defined by $\overline{\overline{C}}$ in Eq. 3.10. Figure 6.1 shows a schematic representation of the rows of $\overline{\overline{C}}$ which define 5 slices chosen for excitation in the first set of functional MRI experiments. Two contiguous coronal slices of 7.5mm each (C1, C2) to cover motor cortex in the precentral gyrus and 2 contiguous coronal slices of 7.5mm each (C3,C4) to cover visual cortex in the calcarine sulci were chosen.

The profile C5 was chosen so that spins close to the volume of interest, that may contribute to in-flow effect, would experience the same level of saturation as spins inside the slices chosen for imaging. We will refer to the volume encoded by the profile C5 as the "saturation region". C5 was designed to alternate between negative and positive values to keep the signal from the excited volume within the dynamic range of detection. To examine the effectiveness of the method to reduce in-flow effect, the fMRI session was repeated both with and without the fifth slice (C5 in Fig. 6.1).

After RF pulse shapes were computed, magnitude and phase files were transferred to the MR imager for use with the pulse sequence. RF pulses exciting the desired slices were used in succession for each shot until k-space matrices were filled for each of the 5 slices.

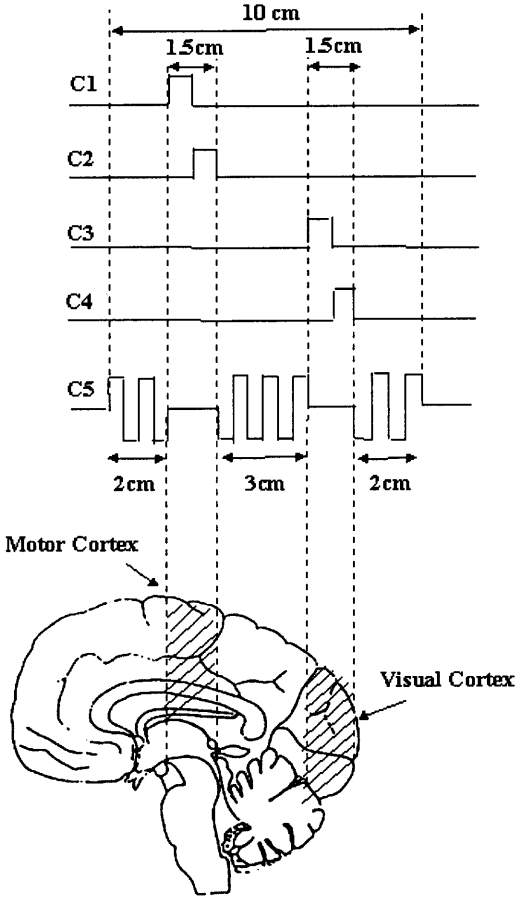

Figure 6.1. Encoding scheme including saturation regions (C5). Non-Fourier encoding in the slice-select direction with two contiguous coronal slices of 7.5mm each (C1, C2) to cover motor cortex in precentral gyrus and 2 contiguous slices of 7.5mm each (C3, C4) to cover visual cortex in calcarine sulci are shown here. The two volumes are separated by 2 cm in this particular subject. (Yoo et al., *Magn. Reson. Med.*, 41:759-766, Copyright © Wiley-Liss, Inc. Reprinted by permission of Wiley-Liss, Inc., a subsidiary of John Wiley & Sons, Inc.)

6.2.2 Hadamard Encoding

A Hadamard version of the encoding was performed in our second set of experiments. Three contiguous slices (C1, C2, C3 using notation of Eq. 3.10) of 1 cm thickness each covering 3cm, and a slice of 2cm width (C4) on either side of the contiguous slices (as shown in Fig. 6.2) were chosen for Hadamard encoding. To examine the effectiveness of the method to reduce in-flow effects, the fMRI session was repeated both with and without the slice covering the saturation regions (C4 in Fig. 6.2).

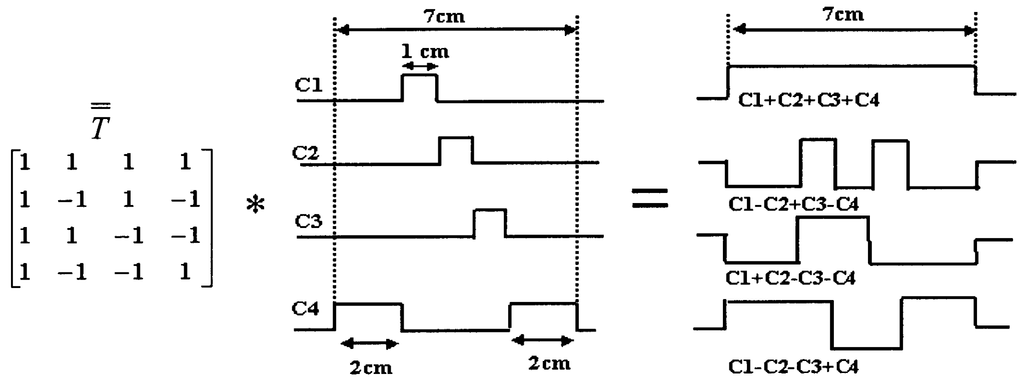

Figure 6.2. Volume encoding scheme including saturation regions are shown on the left-hand side of the schematic equation. Hadamard combinations of these profiles obtained by matrix multiplication with Hadamard matrix $\overline{\overline{T}}$ are shown on the right. (Yoo et al., *Magn. Reson. Med.,* 41:759-766, Copyright © Wiley-Liss, Inc. Reprinted by permission of Wiley-Liss, Inc., a subsidiary of John Wiley & Sons, Inc.)

The four RF pulse shapes (ie, one for each profile) were computed on a workstation by Fourier transformation of the Hadamard combinations. For reconstruction, each of the 4 data matrices was Fourier transformed in both directions and then Hadamard combinations of the matrices were formed to decode information in the third dimension. For the fMRI study, the same image parameters were used as in the first set of experiments. Since the fourth excitation pulse was used to excite the saturation region, only three slices were available for fMRI. Three contiguous slices were imaged, and the experiment was repeated with both motor and visual stimulation separately.

6.2.3 Task Paradigms and Data Analysis

Motor (finger tapping in right hand) and visual (viewing of 8 Hz stroboscopic light) tasks were performed by each volunteer in two separate sessions. A series of 50 acquisitions was obtained in a session with 5 control periods interleaved with 5 periods of activation. Approximately 5 seconds of delay were introduced between control and task period to allow for hemodynamic response to reach steady state [25,54]. For fMRI with Hadamard encoding, a series of 20 image acquisitions was obtained in each session with 2 control periods (rest-periods) interleaved with 2 periods of activation over each session, resulting in 5 image sets from each period.

Pairwise subtraction of each image set in the time series with respect to the first image set in the time series was performed to test for significant bulk motion of the head. No significant motion was detected in any of the trials. Slow signal drift over the time series was removed by linear de-trending. Pixel-by-pixel paired t-test scores were calculated and converted to p-values. Clusters of 3 or more pixels with significant activation ($p < 0.005$) were chosen for display and for further temporal analysis.

Activated areas were analyzed by the number of voxels of $p < 0.005$ and the average signal change with respect to the averaged base-line signal intensity upon activation. ROIs were defined in the precentral gyrus and around the calcarine fissure. In each individual, the same ROI was chosen for the cases of encoding with and without the saturation regions. The temporal response of the activated pixels was examined to see how the signal varied with the inclusion of the saturation regions. Signal changes due to activation were normalized with respect to the baseline intensity.

6.3 Results

6.3.1 Activation Map

Figure 6.3 shows the results obtained from subject #1 with pixels of $p < 0.005$ overlaid on the anatomical images. Figures 6.3a and 6.3b show results of the visual task with and without encoding of a saturation region and Fig. 6.3c and 6.3d show results from the motor task. Similarly, Figure 6.4 shows the results from subject #4 using Hadamard encoding analogous to the multi-slice imaging experiment. The 4th RF profile was used for the saturation band (C4 in Fig. 6.2), therefore, only three contiguous slices were obtained. Functional maps showed the activation in sites consistent with those expected for the tasks. Results obtained with encoding of saturation regions were significantly different from those obtained without the encoding of a saturation region in that they showed less 'activation' in regions where no functional activation was expected such as in a venous sinus (Arrows in Fig. 6.3 and 6.4). We hypothesize this is due to the suppression of in-flow effects.

6.3.2 ROI Analysis for Inflow-Reduction

Table 6.1 summarizes the results from the 6 volunteers tested using the multi-slice imaging and Hadamard encoding. Without saturation, the average signal changes were quite large compared to expected BOLD change which is reported to be in the range of 1-6% in cortical tissue at 1.5T (6% maximal signal change was adapted from the lower boundary of experimental data of Gati *et. al.* [22]). A relatively large standard deviation in signal changes among the activated pixels was observed suggesting that pixels affected by activation-related in-flow were included in the ROI. When a saturation region was encoded, the results showed an overall decrease in number of activated pixels and also in the amount of signal change. However, in several cases (subject #1 motor, subject #2 visual, subject #4 visual and motor) the signal changes were still somewhat large to be due to BOLD contrast alone. The relatively large standard deviation in these activated regions suggests remaining in-flow related signal.

In order to further evaluate the effect from the inclusion of the inflow reducing saturation regions, an analysis in terms of percentage signal change associated with the activation paradigm was performed on several activated pixels from subject #1 (see Fig. 6.5). Figure 6.6a shows a comparison of the mean signal difference between control and activation periods in pixels when encoding with and without the saturation regions. The temporal response of one of the activated pixels (Pixel #3 in visual cortex) is shown in Fig. 6.6b. We found that most of the cortical pixels showed significant decrease in the activation-related signal change (from 14.5-5.6% down to 7.3-3.4%) when saturation regions were encoded. However, pixel #1 located in the region of the superior sagittal sinus showed a decrease in signal change from 19.7% down to only 12.8%, suggesting a remaining in-flow component. We hypothesize that fast-moving spins in the sinus pass directly through the saturation regions into imaging slices. A study of the effects of varying the width of saturation region outside of image plane could help to determine the validity of this hypothesis.

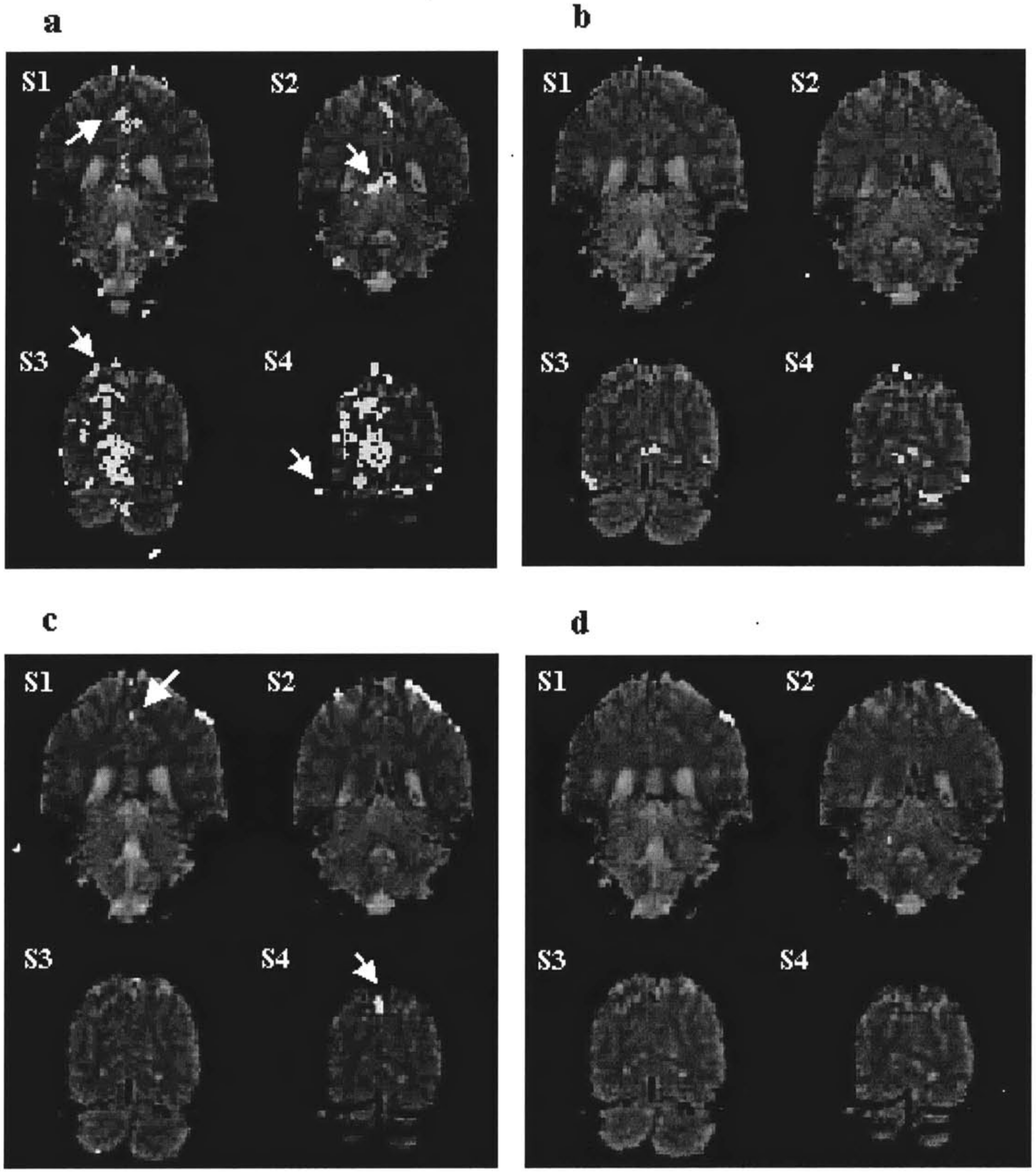

Figure 6.3. Comparison of fMRI results ($p < 0.005$ in white dots) with and without saturation regions using multi-slice method. Results obtained with encoding of the saturation region were significantly different from those obtained without the encoding of a saturation region in that they showed less 'activation' in regions where no functional activation was expected (in white arrows) such as in venous sinus. (a) Visual task without saturation regions, (b) Visual task with saturation regions. (c) Motor task without saturation regions, (d) Motor task with saturation regions. (Yoo et al., *Magn. Reson. Med.,*41:759-766, Copyright © Wiley-Liss, Inc. Reprinted by permission of Wiley-Liss, Inc., a subsidiary of John Wiley & Sons, Inc.)

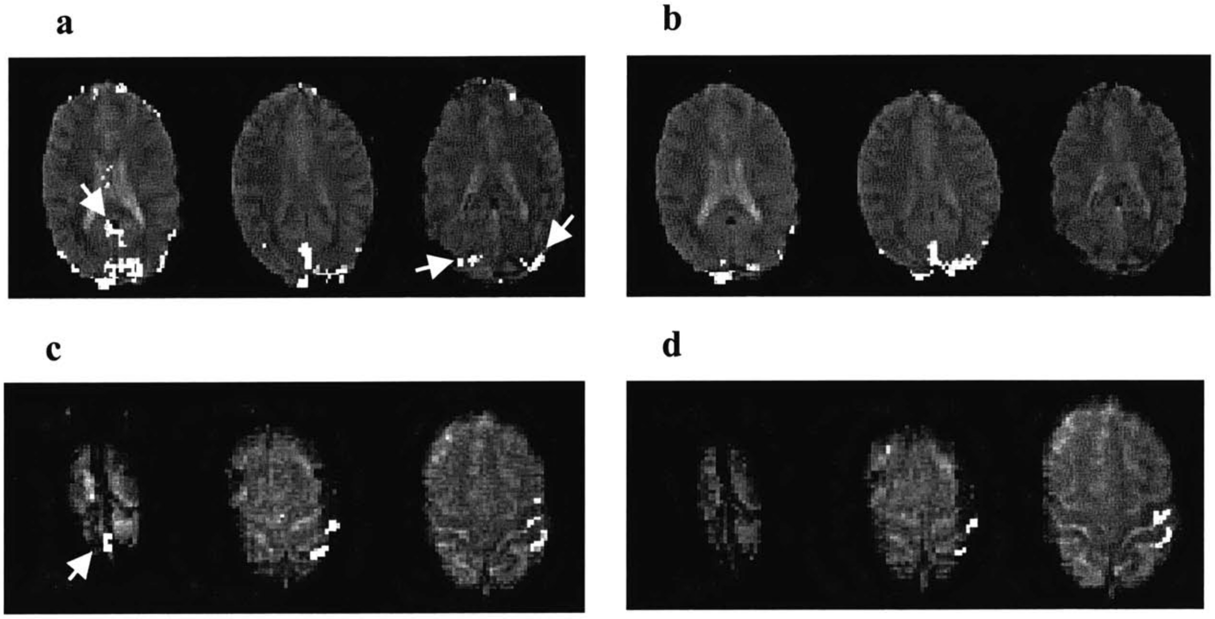

Figure 6.4. Comparison of fMRI results ($p < 0.005$ in white dots) with and without saturation regions using Hadamard encoding analogous to Figure 6.3. (a) Visual task without saturation regions, (b) Visual task with saturation regions. (c) Motor task without saturation regions, (d) Motor task with saturation regions. (Yoo et al., *Magn. Reson. Med.*, 41:759-766, Copyright © Wiley-Liss, Inc. Reprinted by permission of Wiley-Liss, Inc., a subsidiary of John Wiley & Sons, Inc.)

			Number of Activated Voxels		Average Signal Change in Activated Voxels	
Encoding Method	Subject	Task	w/o Saturation	w/ Saturation	w/o Saturation	w/ Saturation
Multi-Section Imaging	1	visual	91	27	5.09%± 3.14	3.85% ±2.00
		motor	29	19	8.38%± 3.60	7.02%± 5.60
	2	visual	27	29	8.75%± 9.90	5.99%± 6.60
		motor	33	22	3.35%± 2.24	3.82%± 2.39
	3	visual	26	17	9.14%± 3.25	5.32%± 2.15
		motor	35	24	10.45%± 5.10	5.67%± 1.75
Hadamard Encoding	4	visual	14	13	9.81%± 8.70	7.14%± 5.20
		motor	35	22	8.25%± 6.07	6.36%± 4.80
	5	visual	21	14	3.34%± 1.29	2.67%± 0.99
		motor	31	9	6.91%± 5.73	4.68%± 1.93
	6	visual	27	18	8.14%± 3.52	3.14%± 1.15
		motor	14	6	1.86%± 0.61	1.85%± 0.51

Table 6.1. Comparison of the number of activated voxels ($p < 0.005$) and regional average signal changes (Mean % ± SD) in activated voxels when encoding with and without saturation regions. For each voxel, signal change during the activation-period was calculated with respect to the baseline (control period) intensity.

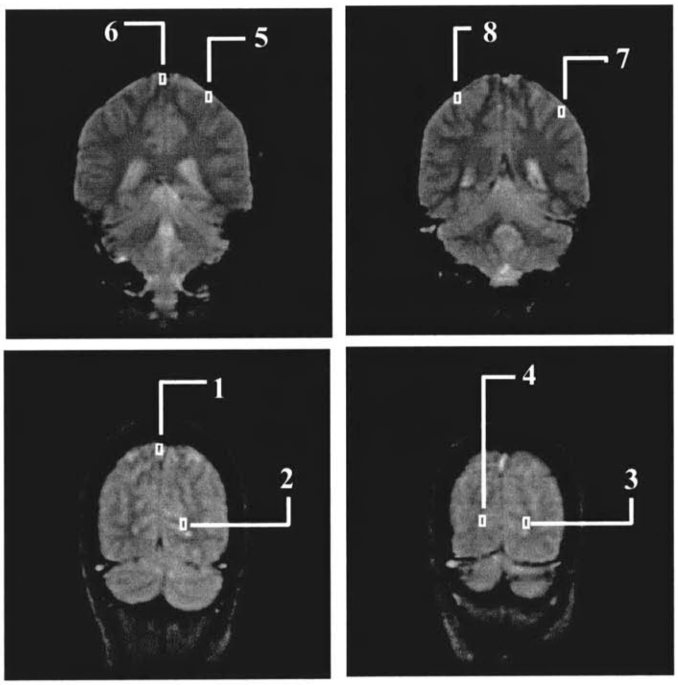

Figure 6.5. Location of pixels used in data analysis from subject 1. Pixels 1-4 were used for visual task, and pixels 5-8 were used for the motor task. (Yoo et al., *Magn. Reson. Med.*, 41:759-766, Copyright © Wiley-Liss, Inc. Reprinted by permission of Wiley-Liss, Inc., a subsidiary of John Wiley & Sons, Inc.)

(a)

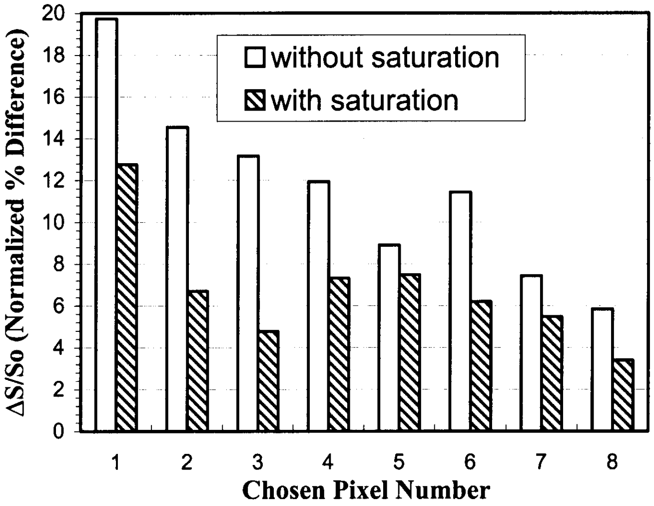

(b)

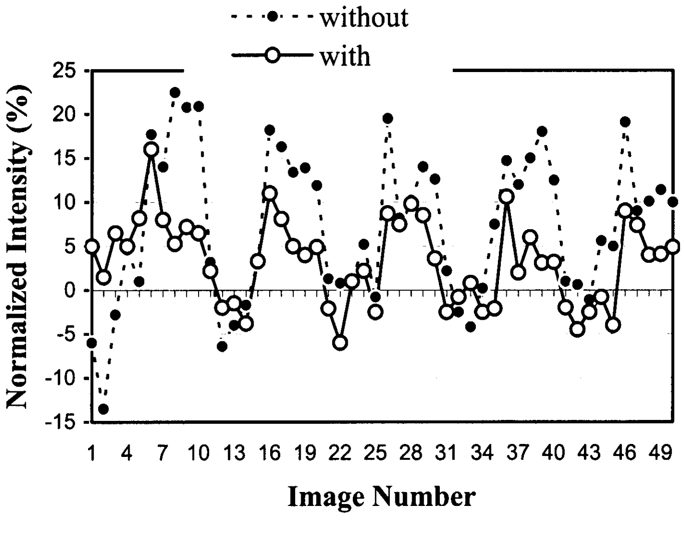

Figure 6.6. (a) Comparison of mean signal difference (ΔS) with respect to the baseline intensity (S_o) in chosen pixels with and without the saturation regions. Note a significant decrease in the signal change when saturation regions are encoded. (b) Temporal response of normalized signal intensity in pixel 3 with and without the application of the saturation regions.

6.4 Summary

In this chapter, RF encoding using spatiality-selective excitation was adapted in the slice-select (or through-plane) direction for functional MRI. It was demonstrated that it is possible to selectively monitor planes irregularly distributed throughout the brain without the need to encode the whole volume. This flexibility was exploited in order to reduce in-flow effects, which are a difficult problem for most multi-shot, multi-slice methods by applying uniform saturation over both imaging slices and slices adjacent to the imaging slice. The method also offers the potential for SNR improvement with appropriate choice of encoding basis for the through-plane direction such as Hadamard basis. Because this approach turns the through-plane direction into an 'encoded' direction, it is a true volume encoding technique analogous to 3D Fourier encoding. In the next chapter, the implementation of adaptive fMRI algorithm with real-time data transfer and processing for functional brain mapping is presented.

Chapter 7
Real-time Adaptive Functional MRI

7.1 Introduction

As previously proposed by Panych et al, RF encoding can be used for adaptive multi-resolution imaging [40]. By applying this multi-resolution approach to fMRI, we believe that areas of activation can be selectively explored in real-time at increasingly higher spatial and temporal resolution, or a combination of both, depending on the specific goals.

The basic idea of the adaptive approach in fMRI is that the regions of activation, however they are distributed throughout the brain, can be selectively detected in multiple stages at progressively higher resolution, while ignoring quiescent regions and "zooming" only into the regions of activation. An example of such adaptive fMRI-encoding scheme using non-Fourier encoding in the slice-select direction could be designed as shown schematically in Fig. 7.1. First, the whole brain volume is imaged in thick sections (for example, 12 mm) and fMRI data is processed to detect the slices with activation. The second imaging stage encodes with smaller slice thickness (6mm in this example) and RF pulses designed to encode only those slices that show the activation with fewer numbers of slices (8 slices in the example). Therefore, both temporal and spatial resolution of the second stage is increased compared to the first stage. The process can be repeated in an iterative manner, from third to fourth stages, until some minimum section thickness is reached (1.5mm thick at the fourth stage).

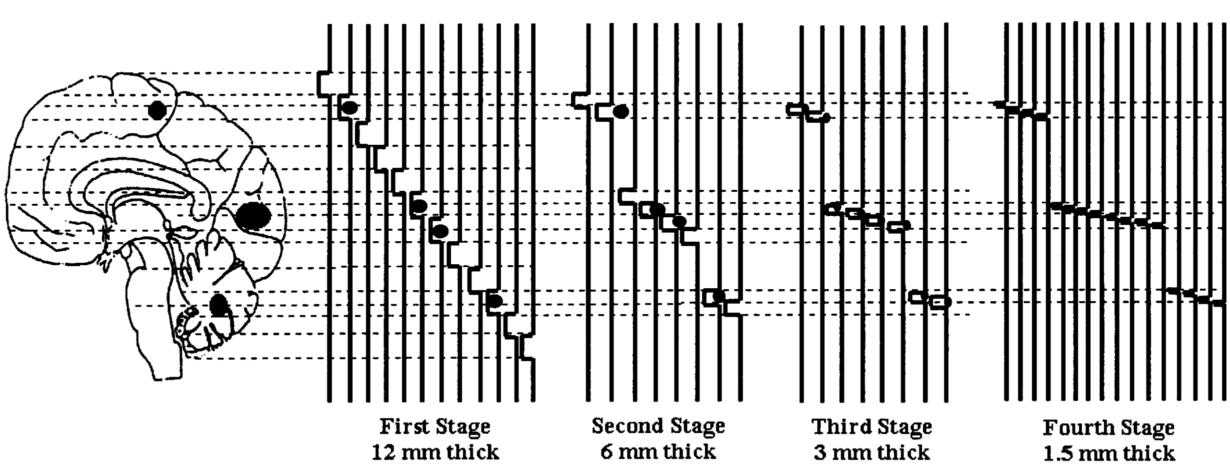

Figure 7.1 A schematic illustration of an adaptive fMRI algorithm. Slice-selective profiles in axial slices are shown in multiple stages of a scan session. Circles represent the areas of the brain that are activated during cognitive tests. Dots in the profiles indicate sections where activation is detected during each fMRI scan.

In this chapter, the flexibility and versatility of an adaptive multi-resolution method is demonstrated using a sensorimotor activation paradigm implemented with an interleaved EPI sequence on a conventional MR system. The hardware configuration and real-time adaptive algorithm are described. In addition, data from the real-time fMRI experiments is analyzed quantitatively to assess the adaptive multi-resolution approach in fMRI in terms of BOLD CNR.

7.2 Materials and Methods

In this adaptive multi-resolution approach, the scan session was divided into several stages where we dynamically changed which volume elements to excite, based on the results from the real-time functional processing. We used planes with variable thickness as the basic volume elements to encode the volume (Fig. 3.5, Section 3.3.1). At the end of each stage of imaging, new RF pulse waveforms were computed according to the operator's prescriptions regarding new target locations, and the waveforms were transferred to the imager for the next stage of scanning.

The adaptive scheme adopted in the study included five stages, calling for operator interaction between each stage (Fig. 7.2). The operator was able to observe the evolution of the functional correlation maps over the course of the experiment and switch from one imaging stage to the next, by selecting slices-of-interest for further study. Imaging and real-time analysis proceeded to the next stage.

To demonstrate the flexibility of real-time adaptive fMRI, the subjects executed an easy and well-characterized finger tapping task, which was expected to simultaneously activate both cerebral and cerebellar areas [32, 46]. For the purposes of this demonstration, we concentrated on the detection of primary sensorimotor cortex, and deliberately neglected other telencephalic areas involved in motor control, such as the supplementary motor and premotor cortices. The primary sensorimotor cortex and the cerebellar motor area of activation are at a relatively large distance from each other and serve to demonstrate the flexibility of the adaptive, multi-resolution approach.

Periods of self-paced sequential finger opposition of the right hand were alternated with resting periods. In order to limit possible adaptation during the task performance and ensure consistent cerebellar activation, the sequence of finger opposition was reversed upon completion of every other set of finger-opposition tasks [32, 46]. Ten sets of images for each epoch (on/off cycle) were acquired. Epochs were acquired at each level of slice thickness until the expected activation areas in the contralateral (left) motor cortex as well as in the ipsilateral (right) cerebellar motor area [32] were detected by real-time correlation analysis [74].

Initial functional maps of eight contiguous slices covering both anatomical areas of interest, pre- and post central gyri and cerebellum, were generated. The operator then selected four slices demonstrating task-related activation for further mapping in the second stage. In the third stage, two of the slices from the second stage were explored at increased spatial resolution in the slice direction, that is, each original slice was imaged as two contiguous slices, with half the thickness. For the fourth stage, two slices from the third stage were chosen for further exploration at the highest resolution (2.5mm-thick). Finally, in the fifth stage, three slices were selected at multiple resolutions (5mm and 10mm slice thicknesses).

7.2.1 Subjects and Image Acquisition

The real-time functional mapping of a motor activation paradigm was performed on two male subjects (aged 29 and 32) in the multi-staged, multi-resolution adaptive scan sessions. In all functional imaging experiments, an Interleaved Echo-Planar Imaging (IEPI) sequence [102] was adapted for RF encoding in the slice-select-direction (Section 3.3.1). To reduce the contribution of inflowing spins, a uniform degree of magnetization was established by applying saturation RF excitation to thick regions on either side of imaging planes which were not adjacent to other selected imaging sections (see Section 6.2). Image encoding in the slice-select direction was performed as previously described using combinations of thin planes as the basic volume elements. For example, in our real-time implementation, 10mm thick slice profiles were constructed as the sum of four 2.5mm-thick planes, whereas we only used two of our basic plane elements in the case of a 5 mm-thick slice. Any volume of interest could be probed as long as it can be represented as linear combinations of the 2.5 mm-thick planes.

Eight shots, each with twelve individually phase-encoded echoes, were acquired for each image. Echo data from each successive shot were interleaved to fill a 96x96 k-space matrix. The FOV was 24 x 24cm, giving a nominal in-plane resolution of 2.5mm. TE was 50 msec. TR and flip angle were variable depending on imaging stage. Although we could have changed in-plane resolution for each image stage, we maintained it constant throughout the experiment. For ROI analysis, real-time data were processed retrospectively. For consistency with the previous experiments using varying slice thickness shown in Chapter 5, only the first 50 sets of images from the real-time session were chosen for ROI analysis. The region-of-interest was defined as voxels with significant activation ($p<0.001$) at the lowest resolution.

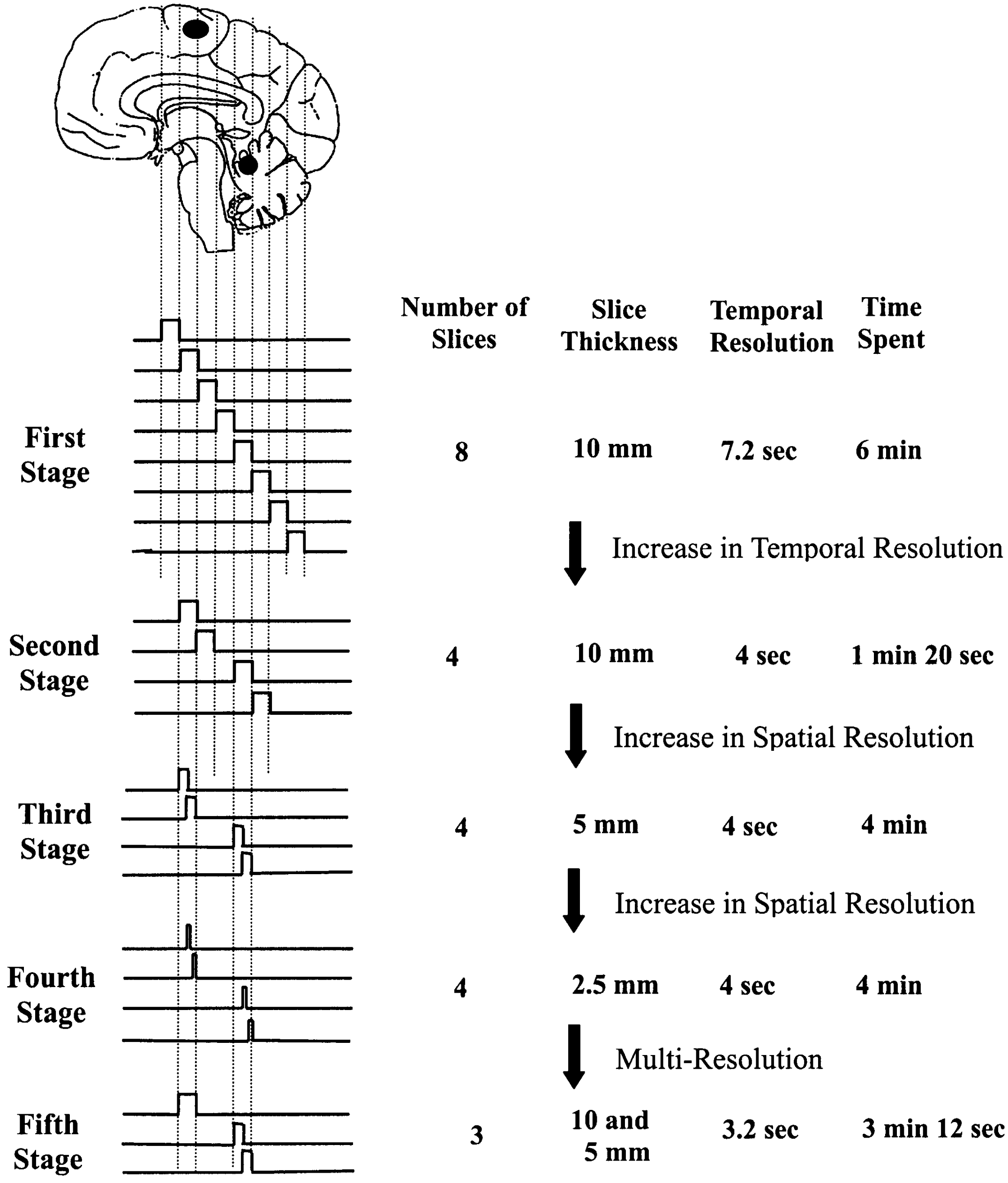

Figure 7.2 A schematic illustration of an adaptive fMRI algorithm. Left column indicates the slice-selective profiles for coronal slices. The black circles in the brain region refer to the ROI's that are in the primary motor cortex and cerebellum. The right column indicates the number of encoded slices, slice thickness, temporal resolution, and time taken to complete each stage. All scanning was done using a multi-shot EPI sequence on a 1.5T imaging system with standard gradient hardware. (Yoo et al., "Real-time Adaptive Functional MRI", *Neuroimage*, 10:596-606, Copyright © Academic Press. Inc. Reprinted by permission of Academic Press. Inc.)

7.2.2. Hardware and Software Configuration for Real-time Adaptive System

In order to achieve a real-time environment for fMRI, we linked three external workstations to the MRI scanner. Dr. Pairash Savironpoorn and Dr. Lei Zhao designed and implemented the communication protocols and processing platform. All implementation work specific to fMRI was performed within the framework of this thesis. A schematic description of the system is shown in Fig. 7.3. A communication control workstation (SUN SPARC 2, Sun Microsystems, Mountain View, CA) functioned as a relay for the transfer of data and pulse sequence parameters between a high-performance Sun Microsystems' Ultra Enterprise 6000 and the MRI scanner. Acquired MRI data and pulse sequence parameters were first passed between the scanner and the communication control workstation through direct memory access (DMA). The communication control workstation, in turn, communicated with the Ultra Enterprise via a local Ethernet. A third, general-purpose workstation (SUN SPARC 10) located adjacent to the scanner and connected via Ethernet to the high-performance computer, was used as a front-end for data display and interactive control interface. Communication programs were coded in C. Data processing and display, and control interfaces were programmed using Matlab (The Mathworks, Inc. Natick, MA).

During real-time dynamic adaptive imaging, raw data was transferred to the Ultra Enterprise via the communication control workstation immediately after each acquisition. As soon as a complete set of image data was available, an image was reconstructed by the Ultra Enterprise and displayed on the general-purpose workstation. Real-time functional processing using correlation analysis was performed immediately after the image-reconstruction using a recursive algorithm that includes linear trend removal [74]. The operator was able to view real-time computed correlation-coefficient maps and to adjust the threshold p-value for display on the front-end workstation next to the scanner.

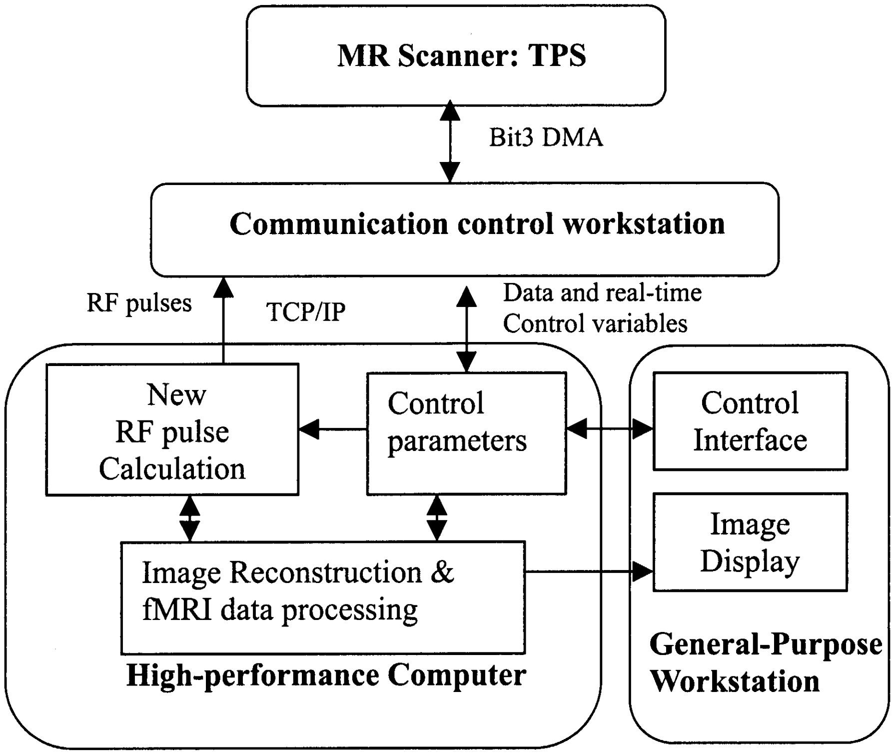

Figure 7.3 A schematic of the real-time adaptive functional MRI system. The set of three workstations (communication control, general-purpose workstation, and high-performance computer) was used for data processing, visualization and control. The tasks of each component are also shown. The arrows indicate the flow of the control parameters and data. (Yoo et al., "Real-time Adaptive Functional MRI", *Neuroimage*, 10:596-606, Copyright © Academic Press. Inc. Reprinted by permission of Academic Press. Inc.)

7.3 Results

7.3.1 Real-time Adaptive Functional MRI

Real-time adaptive functional MRI were conducted to demonstrate the flexibility and versatility of the adaptive fMRI method. Each of the two subject studies consisted of five scan-stages (See Fig. 7.2). The results from one subject (29 year-old) are presented in Fig. 7.4.

The First Stage: Identification of Volumes-of-interest

In the first stage, eight 1-cm-thick coronal sections, covering a contiguous slab including pre- and post-central gyri as well as the cerebellum, were acquired every 7.2 seconds. Functional maps were processed and displayed in real-time, and at any time during the scan, the operator was able to specify one or more locations for zooming. Processing of data from the first stage demonstrated task-related activation in the contralateral (left) primary motor cortex and ipsilateral cerebellum (Fig. 7.4A) leading to a choice of a volume-of-interest for the second imaging stage.

The Second Stage: Increasing Temporal Resolution

Four sections demonstrating activation were chosen for further characterization and imaged at higher temporal resolution in the second imaging stage. New RF pulses were computed and transferred to the scanner, and scanning continued at the 4 new locations without any interruption until activation was confirmed to operator satisfaction. The purpose of continuing the data acquisition with higher temporal resolution in the second imaging stage was to increase statistical confidence that there was activation within selected regions. As expected, p-values declined in selected ROI's with the inclusion of additional data. The average p-value in a 3 by 3 pixel-ROI in one subject went from 0.2 down to 0.6×10^{-4} in sensorimotor area, and in a cerebellar ROI from 0.25 down to 0.01. In the second subject's sensorimotor area, the average p-value went from 0.1×10^{-4} to 0.3×10^{-5} and the cerebellar ROI from 0.4×10^{-2} down to 0.6×10^{-3}. The operator then elected to zoom into one slice in the motor cortex and one slice in the cerebellum for the third stage of imaging.

The Third and Fourth Stage: Spatial Zooming

In the third and fourth stage, two slices were chosen and resolved at higher resolution by halving the slice thickness (each selected slice was divided into two new sections). Thus, in the third stage, four 5mm-thick sections were imaged every 4 seconds (Fig. 7.4C). The scan continued until significant activation was observed consistent with the previous scanning. Two distinct areas of activation within the 10 mm-thick slice covering the left motor cortex, were resolved in separate 5 mm slices in the third imaging stage of the adaptive procedure. Two of the 5mm-thick sections were chosen for further characterization, and split into 2.5mm-thick slices with isotropic voxels (2.5 mm x 2.5 mm x 2.5 mm). At this point, activation was still detectable in the motor cortex, but no longer detectable in the cerebellum (Fig. 7.4D).

The Fifth Stage: Spatially Variable Resolution

The flexibility of multi-resolution imaging was demonstrated in the fifth stage (Fig. 7.4E), in which the operator chose two different resolutions for the detection of primary sensorimotor and cerebellar motor activation (Fig. 7.2). The primary sensorimotor cortex was imaged with two 5mm-thick slices while the cerebellum was imaged with a single 10mm thick slice to confirm that activation was still present. As expected, the prominent activation in both motor and cerebellum was detected again. At this point, the locations of interest were being imaged every 3.2 sec, over double the rate of imaging in the first stage of the adaptive procedure (Fig. 7.2).

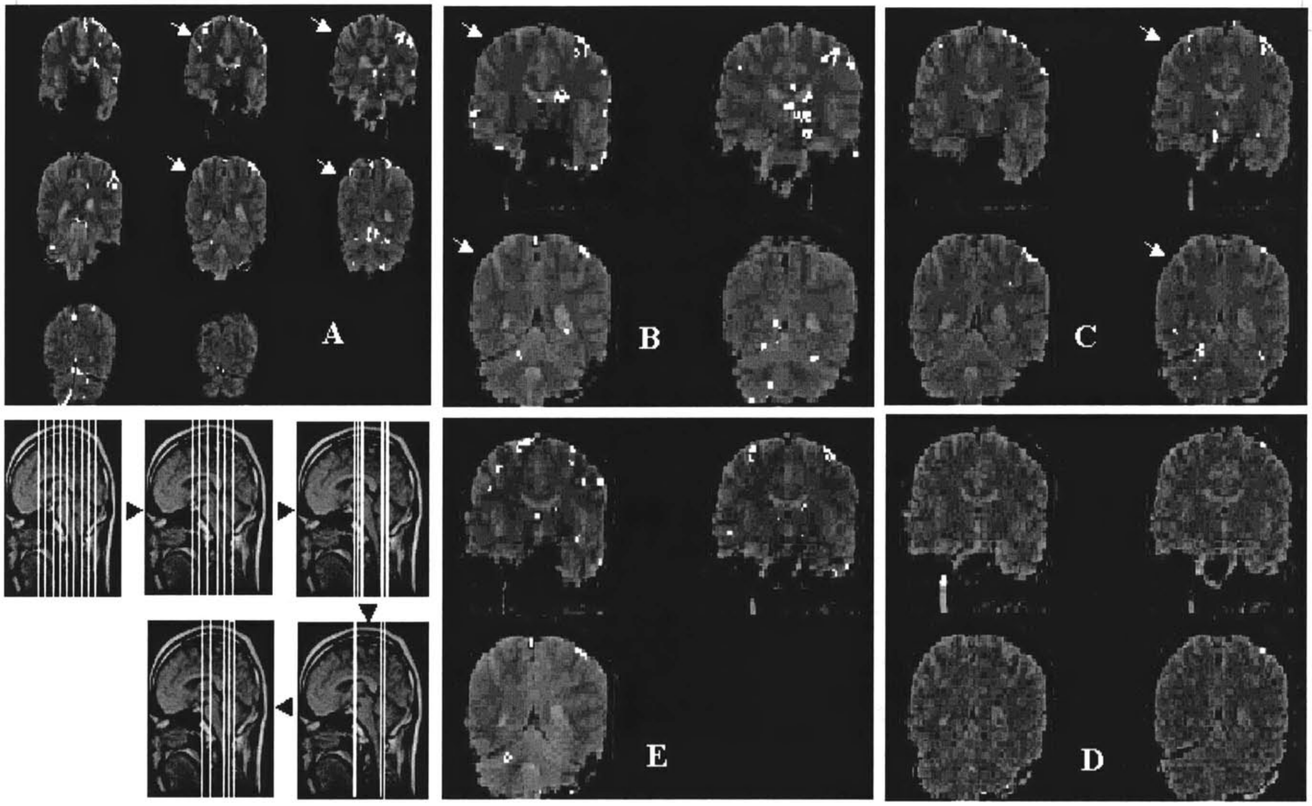

Figure 7.4 Results from an adaptive fMRI session. Box in lower left corner indicates the locations of the slices selected by RF encoding during five stages of the adaptive session. fMRI results are thresholded at $p < 0.001$, and shown as white dots overlaid on anatomical images. (A) Results of the first stage from eight 10mm-thick contiguous slices. Four sections from the first stage (white arrows) were chosen for continued scanning in the second stage using same slice thickness. (B) Results of the second stage. Two sections from the second stage (white arrows) were chosen and further split as two 5mm thick slices. (C) Results of the third stage. Two sections were chosen from the third stage and further split into two 2.5mm-thick slices. (D) Results of the fourth stage. (E) Results of the fifth stage. Two sections with 5-mm thickness to cover motor cortex and one 10mm section to cover cerebellum are shown. (Yoo et al., "Real-time Adaptive Functional MRI", *Neuroimage*, 10:596-606, Copyright © Academic Press. Inc. Reprinted by permission of Academic Press. Inc.)

7.3.2 Quantitative Evaluation at Multiple Resolutions

From the real-time data (two ROI's in the motor cortex and one ROI from the cerebellar in one subject), several ROI's were chosen for further analysis. In Figure 7.5, the mean signal change, noise level and contrast-to-noise ratio are presented for ROI's at each of three slice-thicknesses. The results from the ROI analysis are presented as three vertically arranged rows of boxes where each row represents the results of ROI-analysis at a different slice thickness. The mean BOLD signal change and standard deviation of noise is written within each box. The Contrast-to-noise ratio (CNR), is the number written under each box.

These results are consistent with those obtained in our previous multi-resolution study (Section 5.3.2). As previously, we found that (1) BOLD signal change was additive with increasing slice thickness, (2) noise increased with increasing slice thickness, and (3) CNR increased as slice-thickness increased. The few exceptions where the BOLD signal was not additive (ROI 1 in Fig. 7.5, zooming from 10mm to 5mm thickness) are possibly due to either inconsistency in task performance between each imaging stage by the subject or the difference in susceptibility-related signal losses at different slice thickness. The BOLD signal for the ROI's with CNR smaller than unity was, as expected, not additive because there was no statistically significant activation (noise is not expected to be additive). The second observation of a tendency toward increased noise level as slices get thicker, is especially evident when we look at the mean noise level for all ROI's in a sensory area as detailed in Table 7.1.

It should be noted that, during the real-time adaptive imaging, the cerebellar ROI (ROI 3 in Fig. 7.5) chosen in the process of zooming from the 5 mm-thick slice to two 2.5 mm-thick slices, had a CNR of only 0.5. Subsequently, there was no functional detection at 2.5mm slice thickness due to the choice of the slice with low CNR. In retrospective analysis, we noted that the slice with higher CNR, from which we may actually have detected cerebellar activation at 2.5mm, was not chosen for zooming by the operator.

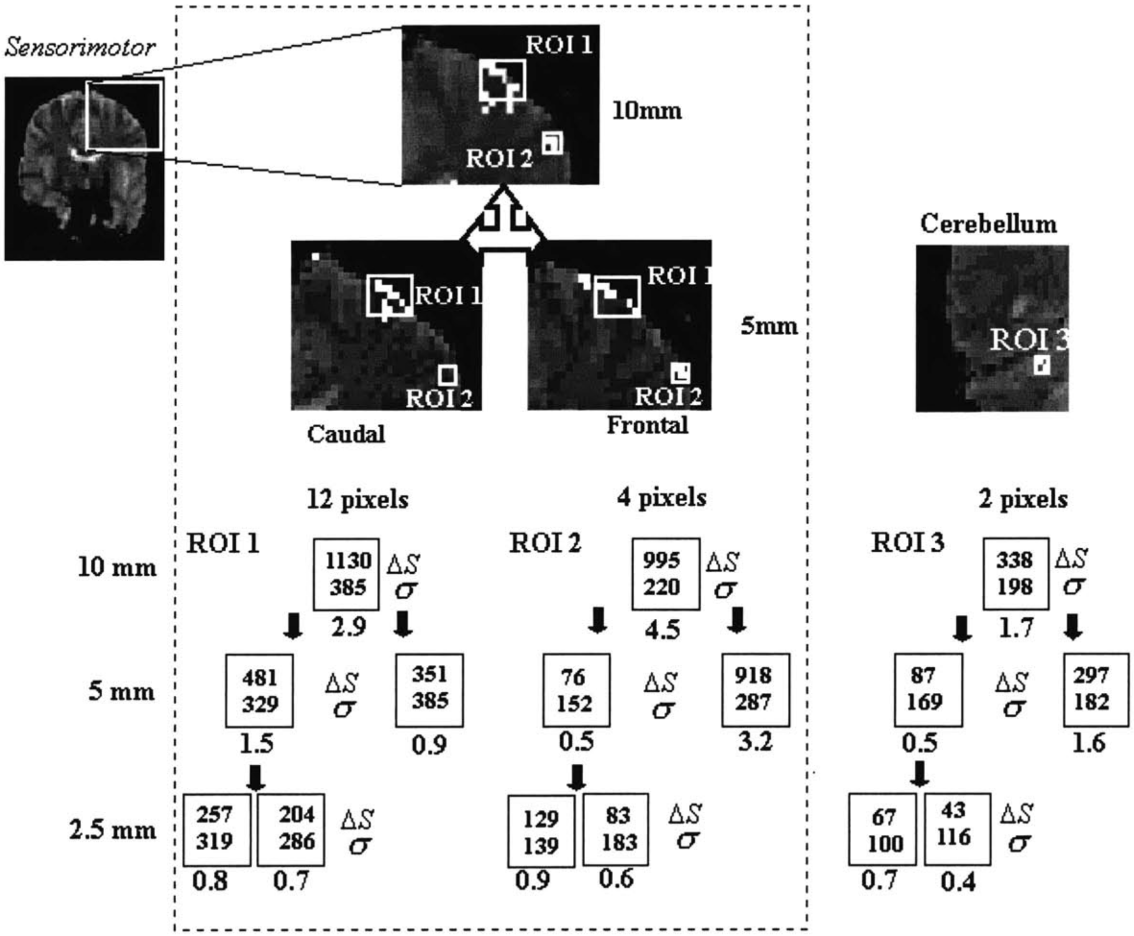

Figure 7.5 Retrospective ROI analysis of real-time fMRI results at different slice thickness (10mm, 5mm, and 2.5mm) on the data from a 29-year old male. The location of the ROI (Sensorimotor or Cerebellar) is indicated at the top of each anatomical image. Two sites of activation (ROI 1 and 2) seen in the 10mm-thick slice were resolved further in caudal and frontal direction in 5mm-thick slices. The number of pixels in each ROI is indicated ($p < 0.001$). Unit-less mean signal change and noise are shown with CNR. A schematic is shown for each ROI analysis on the right with the three vertically arranged boxes representing the three levels of slice thickness (as indicated in the right column horizontally). The top number in each box indicates the mean change (ΔS) in signal between stimulus and non-stimulus phases, and the bottom number represents the combined standard deviation of the signal σ. The ratio of the two numbers, equal to the CNR, is written below each box. (Yoo et al., "Real-time Adaptive Functional MRI", *Neuroimage*, 10:596-606, Copyright © Academic Press. Inc. Reprinted by permission of Academic Press. Inc.)

In one case, two distinct foci of activation (ROI 1 and 2 in Fig. 7.5) at higher resolution (i.e. 5mm-thick slice) appeared as one focus at lower resolution (i.e. 10mm slice-thickness). This finding supports the notion that even at 1.5T, high-resolution fMRI may be useful in improving delineation of areas of neuronal activation [60]. For example, the activated sites in primary sensorimotor cortex 10mm slice thickness, segregated into two different sections (caudal and frontal) at the higher resolution of 5mm slice thickness (dotted box in Fig. 7.5).

Location	Thickness	Mean noise
Sensorimotor ROI	10 mm	329.1
	5mm	301.3
	2.5 mm	248.6
Cerebellar ROI	10 mm	257.9
	5mm	216.8
	2.5 mm	126.8

Table 7.1 The mean of noise level (unitless) in all ROI's in each sensory area for different slice thickness. The noise level increases for increasing slice thickness.

7.4 Summary

In this chapter, we reported on the design and implementation of an adaptive image acquisition scheme that uses a multi-resolution-based strategy to zoom into the regions of cortical activity. The specific implementation presented in this Chapter consists of five stages of scan sessions that are tailored to identify the volume of interest and to increase temporal (from 7.2 sec to 3.2 sec) and/or spatial resolution (from 10mm to 2.5 mm slice thickness) of the fMRI data acquisition by zooming into selected slices-of-interest. During finger tapping, adaptive imaging with real-time data display and processing capability allowed simultaneous mapping of eloquent primary sensorimotor cortex as well as cerebellar regions using very few slice-acquisitions. The detected activation sites were consistent with those previously described for similar tasks [32,46]. Contrast-to-noise analysis in selected ROI's was performed to quantitatively assess the multi-resolution adaptive approach. Results were similar to the observations from the previous analysis in Chapter 5 using different slice thicknesses.

Chapter 8
Discussions and Conclusions

8.1 Introduction

In this thesis, we have demonstrated how adaptive multi-resolution approach using spatially selective RF encoding can add significant flexibility to functional brain mapping protocols. We believe that real-time adaptation of spatial and temporal sampling to task-related changes will increase the efficiency and flexibility of functional mapping experiments. In this work, the multi-resolution adaptive method, proposed initially by Panych *et. al.* [40], was applied in fMRI to enhance functional signal detection and characterization. The multi-resolution approach was validated using simulations and experiment for both in-plane and through-plane directions and it was shown that BOLD CNR increases to a maximum where the spatial resolution matches the size of the activation.

Non-Fourier RF encoding using manipulation of spatially selective RF pulses was implemented in order to encode spins in the slice-select direction. Several advantages of the method over standard multi-slice approaches were demonstrated. We showed how it is possible to monitor irregularly distributed sections throughout a volume without the need to encode the whole volume. We further showed that it offered the potential for increased signal-to-noise ratio if an appropriate basis is used for encoding. We also showed that a unique design of excitation pulses, it also appeared possible to significantly reduce in-flow effects.

Using spatially selective RF encoding combined with real-time pulse prescription and data processing capabilities, we designed and implemented an adaptive image acquisition scheme that uses a multi-resolution-based strategy to zoom into the regions of cortical activity in the slice-select direction. The method was successfully demonstrated in volunteers performing simple sensorimotor paradigms for simultaneous activation of primary motor, as well as cerebellar areas. Temporal and spatial resolution of the fMRI session were increased demonstrating the effectiveness of our particular implementation of adaptive fMRI. RF encoding is compatible with and can potentially enhance any fMRI experiment, irrespective of the pulse sequence, main field-strength, or the gradient system performance. It is thereby conceivable that real-time adaptive session could yield high-resolution delineation of ROI's in clinically reasonably times.

8.2 Multi-resolution Detection of Activation

In order to theoretically and quantitatively assess the multi-resolution approach for use in functional MRI, we chose BOLD CNR as the measure for functional detection. We investigated the effect of varying both in-plane and through-plane spatial resolution on BOLD CNR and on the BOLD contrast both theoretically (Chapter 4) and experimentally (Chapter 5).

BOLD CNR and Variation of In-plane Resolution

Analysis based on our theoretical models suggests that BOLD CNR is maximized when the spatial resolution matches the dimension of the activation even though BOLD contrast alone is enhanced by imaging at higher spatial resolution. In examination of experimental results, we note that the width of the histogram showing the distribution of BOLD contrast in activated areas broadens to include higher BOLD contrast at higher spatial resolution (Fig. 5.2d). This finding is consistent with the previous observations of others that the histogram breadth of BOLD contrast increases with increase in resolution

[35]. Other researchers have measured BOLD contrast at different resolutions and also suggested that higher spatial resolution tends to increase the magnitude of BOLD contrast [34, 60, 63, 65]. It was hypothesized that this is due to less partial volume averaging of inactive tissue or the increased contribution from the vessels in high-resolution data. These results may falsely imply that high resolution tends to result in better detection compared to low spatial resolution. However, we have further demonstrated that when BOLD CNR is considered, the histogram broadens to include high CNR at lower, not at the highest in-plane resolution (Fig 5.2e). In general, we find that the maximum CNR is obtained when the resolution matches the size of the functional activation itself (Fig 5.3).

Based on the gray-level CNR maps over the region-of-interest (Fig 5.2), we observed a significant distortion in the original shape and size of the activation as we reduced the in-plane resolution. However, this is not a concern because in the multi-resolution zooming approach, low resolution is used only in the initial detection of activation. In later stages of the scan session, higher spatial resolution is used and the highest resolution is used in the final mapping stage. However, it is important to note that, with low-resolution data acquisition, false negative errors are possible. For example, the reduction of BOLD CNR at very low spatial resolution, as illustrated by model and simulation (See Fig. 4.5 and Fig. 5.6) may cause failure in detection due to reduction in BOLD CNR.

The point to be made from the experimental and theoretical results on the variation of the in-plane resolution is that the spatial resolution needs to be optimized to generate the maximum detection of the site of activation. The maximum detection would be obtained by matching resolution to the size of the activation, neither using too high nor by too low resolution.

BOLD CNR and Variation of Slice Thickness

From our analytical model results at different slice thicknesses, we predicted BOLD CNR would be maintained as long as the imaging slice contains the site of activation and the effect of susceptibility-related signal loss is small. Similar to results for the variation of in-plane resolution, we showed that maximum CNR will be obtained if the slice thickness matches the thickness of activation. For the range of slices used in our sensorimotor task, the BOLD contrast was shown to be additive and BOLD CNR was relatively constant regardless of the slice thickness and even increased as long as the slice contained the site of activation (Fig 5.5). The analysis of CNR in our data showed higher or constant functional CNR was observed as slice-thickness increases up to 12 mm. The initial thickness of 12mm was acceptable in primary motor area, justifying the approach of lowering through-plane resolution for initial detection of the activation.

We observed that the noise level in cortical areas increased when thicker slices were used (Table 5.1) and expect that physiological noise may significantly reduce BOLD CNR for very thick slices. For example, If the initial slice is significantly thicker than the dimension of activation, the increase in physiological noise may surpass the BOLD contrast resulting in an increase in false negative error. Susceptibility–related signal losses would also reduce the BOLD CNR. On the other hand, increasing slice thickness might, as we found, increase the BOLD signal due to larger pixel volume and thereby increase CNR if the noise level is relatively constant with slice thickness.

Functional Detection versus Mapping

It is important to distinguish the process of 'detection' from 'mapping' of the brain activation. The purpose of detection is to examine the existence of activation, and may not necessarily to map or characterize the activation. The rationale behind the multi-resolution approach in functional MRI could be compared to the acquisition and analysis of images by a spy satellite for the purpose of identifying the type of aircraft located at an airfield as illustrated in Fig. 8.1a. It would not be efficient to acquire and analyze image data at the spatial resolution necessary to identify aircraft type (δ in Fig. 8.1a) before an airfield had been detected. Instead, the imaging system and detection algorithm should initially be set to detect airfields at lower resolution (Δ in Fig. 8.1a). After the determination of the location of airfields, higher spatial resolution can be used to resolve the type of aircraft.

The situation described above is similar to the brain mapping problem. For the sensorimotor area, which was previously shown in Fig 5.2a, the dimension of whole extent of motor area is approximately Δ which is much larger than the spatial dimension of δ which is necessary to map the detailed profile of activation (Fig 8.1b). Our results show that the detection of the functional activation is maximized when the resolution matches the size of activation (Δ, Fig. 8.1b) from both analytical model and the simulated sensorimotor area (Chapter 4 and 5).

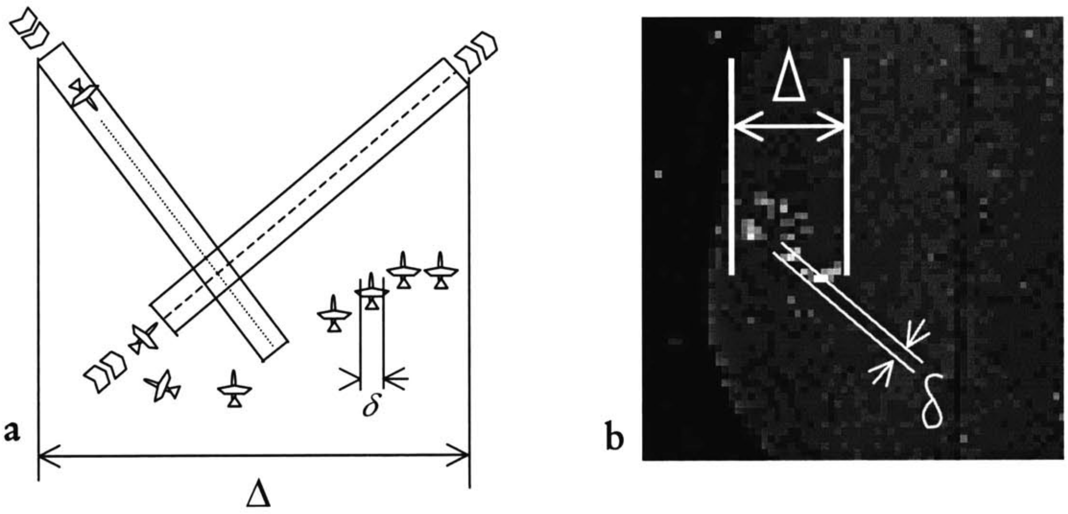

Figure 8.1. Comparison of the detection and the mapping of functional activation to the acquisition and analysis of images by a spy satellite for the purpose of identifying the type of aircraft located at an airfield. (a) An airfield has the size of Δ whereas the resolution of δ is necessary to identify the type. (b) Example from the functional map shown in Fig. 5.2a.

Mapping functional areas can be done much more efficiently if we have some minimum knowledge about what to expect in terms of size of activation. For example, we can expect that many functional areas are more than a voxel size and distributed across the brain. Therefore, in the initial and intermediate scan stages we want to maximize detection of these areas prior to conducting a detailed mapping of the activation. The last stage of the adaptive zooming process is used to identify the detailed activation profile at high-resolution. In order to maximize the detection in the initial stages of imaging, the spatial resolution should match the overall size of the total area of activation and this is usually much lower than the higher levels of resolution desired for mapping.

8.3 RF encoding for Functional MRI

Flexibility of Spatially Selective RF encoding

The proposed RF encoding method has the ability to encode sections that are not only irregularly distributed throughout the volume but that are also of differing thickness. In the implementation reported in Chapter 6, the fundamental volume element was a plane of 2.5mm thickness. Individual sections could be any combination of these volume elements so that, for example, one could use 5mm sections to monitor one part of the brain while using 7.5mm sections to monitor another. Other fundamental volume elements such as lines or strips can also be used to encode the volume. Line encoding may not offer enough SNR for functional MR at 1.5T. However, by using an adaptation of the spliced-pencil sequence [98], we could encode combinations of thin strips providing adequate SNR for fMRI while offering improved temporal resolution and flexibility over the multi-plane encoding approach.

Reduction of in-flow effect

A very attractive feature of the RF encoding method from a practical point of view is the significant reduction of the in-flow effect. The reduction from the contribution of in-flow was achieved by additionally encoding thick sections on either side of the volume of interest. We maintain that this suppresses in-flow by producing a level of saturation for in-flowing spins that is the same as spins within the volume-of-interest. Other approaches such as spatial presaturation [71], dual-echo gradient echo [45], or the long TR in single-shot EPI have been used to decrease the in-flow effect. A major advantage of the proposed method, however, is that the flexibility in spatial encoding can be exploited to reduce in-flow for regions that are not necessarily contiguous, which is not easily implemented with other methods using existing hardware and software.

Hadamard Encoding and fMRI

Hadamard encoding slices in the through-plane direction can achieve potential SNR gains. Quantification is complicated, however, because the SNR depends on multiple factors such as the flip angle, the TR, the number of encoded slices, and the T_1 of the tissue. For example, a SNR advantage of $\sqrt{8} \cong 2.83$ is expected when 8 slices are Hadamard encoded. However, the Hadamard encoding also results in a decrease by a factor of 8 of the effective TR because the whole volume is excited during each TR period. This requires a concomitant lowering of the flip angle (assuming operation at the Ernst angle). As shown (see Fig 3.9), significant SNR gain by Hadamard encoding over the multi-slice approach can be obtained only when a relatively large number of slices (> 16) are encoded.

One possible problem with encoding large portions of the volume with Hadamard encoding lies in peak power limitations which may otherwise demand lowering the flip angle and thereby lowering SNR [107]. This is because wider spatial profiles are excited by more narrowly peaked RF pulses. It is best, therefore, to limit the number of slices that are Hadamard encoded if a large portion of the volume is being covered. Based on the results plotted in Fig. 3.10 of the improvement of SNR for Hadamard encoding compared to the multi-slice method, there was a point beyond which little SNR advantage is gained by increasing the number of slices that are Hadamard encoded. At roughly 1/4 of the maximum number of slices, over 90% of the SNR advantage due to Hadamard encoding are reached and there is little benefit in further increasing the number of slices. This is a useful finding because the possible peak power problem associated with Hadamard encoding large FOV may be reduced by subdividing FOV into sub sections and Hadamard encoding those sections without risking too much of SNR loss.

As an example, assume that column A of Fig. 8.2 shows the Hadamard profiles for encoding 16 slices covering the entire volume. The RF pulses to excite these profiles are likely to lead to peak RF power problems so that it is better to use the hybrid scheme shown in column B of Fig. 8.2 where sets of 4 slices are Hadamard encoded. According to the curve in Fig. 3.9, both schemes are roughly equivalent in terms of SNR advantage, but the scheme that is shown in column B of Fig. 8.2 is preferable because it minimizes the possibility of peak power problems. Issues such as signal fluctuation from imperfection in RF profiles for Hadamard encoding are expected to be negligible since these fluctuations were shown to be small and not correlated with the task-related signal level (Section 3.2.1).

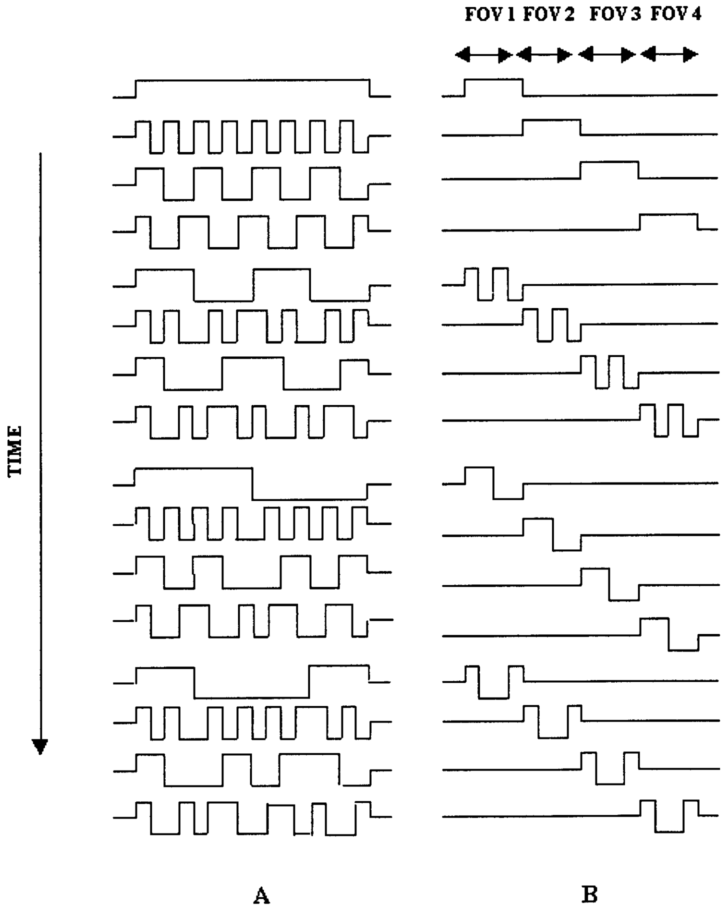

Figure 8.2 An example of the use of hybrid splitting of Hadamard encoding to avoid possible peak RF power in encoding 16 slices with fixed temporal resolution of 1600 msec. The minimum effective TR in this example is therefore 100 msec. Column **A** shows the Hadamard encoding of the full FOV. If the original FOV is subdivided into four regions and each region of four slices is Hadamard encoded (Column **B**), the effective TR is increased by a factor of four to 400 msec so that approximately the same SNR is obtained while peak RF power problems are reduced.

8.4 Real-time Adaptive fMRI

We have designed and implemented an adaptive MR image acquisition scheme based on RF (radio-frequency) encoding in the slice-selection direction with real-time data-processing and transfer capability. It is worth noting that this real-time adaptive setup was implemented on a standard 1.5T scanner with conventional gradient systems (1Gauss/cm). We were therefore limited to using an interleaved EPI sequence. Adaptive encoding is intended, however, to improve scanning efficiency with a variety of pulse sequences, including those used for standard fMRI. It is straightforward to modify a multi-slice, single shot EPI sequence to enable adaptive fMRI at higher speed on imaging systems with more powerful magnetic gradients, and this approach can be applied to any field strength. Although not demonstrated, we believe that the combination of altering resolution in in-plane and through-plane direction would benefit the adaptive approach.

Real-time adaptive imaging has three components: (1) image acquisition, (2) real-time processing of images and the detection of ROI's, and (3) real-time adaptation of imaging parameters based on ROI-detection. In the particular implementation of real-time adaptive imaging demonstrated in this work, the detection of ROI's was enabled by a simple statistical measurement in combination with the somewhat arbitrary choice by a human operator. From our real-time results, it was noted that one 5 mm slice with high CNR in a cerebellar ROI (ROI 3 in Fig. 7.5) was unintentionally ignored in the process of zooming in to 2.5-mm thick slices in favor of a 5 mm thick slice with much lower CNR. This demonstrates the necessity of careful attention by the operator for successful zooming. Premature zooming before the confirmation of activation in a ROI can lead to the missing of regions with significant activation. Some "intelligent" guidance on the part of the adaptive algorithm, for example, more sophisticated statistical analysis leading to automated ROI-selection, is necessary and constitutes area for further investigation.

It also should be noted that the adaptive multi-resolution approach is based on the assumption that there is no substantial change in the location or the size of the original site of activation during the adaptive procedure. Therefore, it assumes that there is no physiological adaptation of cortical areas between each scan stage. For the block-based design, this assumption is accepted. However, the degree of activation in different regions of brain can change during motor learning and other complicated sensorimotor task [50,51]. The adaptive algorithm and the task paradigm under these conditions undergo a complicated interplay that requires further investigation.

8.5 Application of Adaptive Approach

Adaptive selection of activated areas-of-interest could enable sampling of selected locations of interest at ultrahigh temporal resolution to further the understanding of complex temporal relationships of the activation of multiple relays in distributed neural networks. As briefly introduced in Chapter 2, the event-related fMRI method has immerged as a new powerful tool in functional mapping experiments. We have conducted an initial feasibility study of real-time detection of event-related fMRI signals of simple audio-cued, sensorimotor trials [108]. This study suggests that adaptive fMRI data acquisition and analysis can be combined with event-related experimental paradigms.

A potential application of such a design approach might be to selectively study the event-related temporal response of multiple functional regions. Certain cognitive tasks such as the motor response to a particular visual cue are believed to involve multiple brain regions including visual cortex (visual perception), frontal lobe (higher cognitive processing and memory), cerebellum (motor control/planning and attention), supplementary motor cortex, and motor cortex (motor execution) [46,50,54]. The event-related hemodynamic responses in these areas, and the temporal relationship between them are not yet understood in detail.

It would be very useful if the signal changes of those areas could be monitored simultaneously with as high temporal resolution as possible. With combination of fast scan techniques and real-time adaptive MRI, it may be possible to follow the response of such distributed regions with sufficiently high temporal resolution because imaging can be limited to the regions-of-interest regardless of how they are distributed throughout the brain. If the stimulation is carefully synchronized with the pulse sequence, the temporal behavior including rise-time of MR signal change in relation to the gated paradigm might be resolved more finely, shedding new light on the temporal dynamics of the hemodynamic response.

Similar adaptive schemes can be used to characterize regions of interest with different MR contrast mechanisms, including MR spectroscopic imaging [107,109]. An operator could, for instance, elect to pinpoint a functional location using an adaptive multi-resolution approach, and subsequently switch in real-time to the spectroscopic characterization of functional ROIs.

Another potential application of adaptive fMRI approach is the functional mapping for neurosurgical planing. Functional MRI has been used to delineate functionally-eloquent areas adjacent to the target of surgical intervention ([16]-[18]). With the advancement in technologies such as microscope-assisted surgery, the spatial precision of the surgical procedures has greatly increased [19], therefore, high-resolution characterization of activation will be necessary to provide more accurate mapping of functions within the surgical field.

8.6 Future Studies

Studying event-related BOLD signals from multiple regions of brain with high-temporal resolution is one of the main targets of future studies. In order to achieve efficient volume coverage and excellent temporal resolution necessary in study, our research is currently focused on the implementation of the real-time adaptive fMRI method adapted to an EPI system. With dedicated data processing and communicating platform, necessary data transfer and processing will be provided.

Several technical aspects regarding the implementation of adaptive fMRI that are not presented in this thesis, have been recently addressed. They are real-time processing of event-related fMRI [108] as well as a real-time detrending of physiological noise [110]. Real-time processing of ER-fMRI data was achieved by using the reference function estimated to for the hemodynamic response of a given stimuli [108]. Real-time detrending of physiological noise was proposed using predetermined 'tracer' pixels representing respiratory and cardiac component signal prior to the functional data acquisition [110]. By applying the detrending function formed by these tracer pixels to the real-time fMRI algorithm, physiological noise may be reduced in real-time.

The capability to switch in-plane resolution and usage of the different volume element such as lines or strips as a basic volume element will be implemented in the near future. We expect line encoding may not offer enough SNR for functional MRI at 1.5T, however, by using an adaptation of the spliced-pencil sequence [98], we could encode combinations of thin strip with adequate SNR. To study functional areas close to large static susceptibility gradients, it may be necessary to incorporate a variable slice-thickness approach such as the Multiple Variable Slab Thickness (MVST) method in order to reduce the susceptibility loss [111,112]. As we have previously shown in Chapter 6, the RF encoding technique gives the necessary flexibility for implementing approaches with variable size of volume elements.

In the current implementation of the adaptive method, an operator bases the detection of a ROI on somewhat arbitrary selection, thus, premature zooming during adaptive selection or missing the ROI are possible. We expect that some 'intelligent' guidance to aid an operator is necessary to improve detection. Development of such an automated detection algorithm with interactive MR environment constitutes another area for further studies.

As a first step towards an 'intelligent' adaptive method, the following procedure is proposed. First, the brain regions are masked out from the adjacent non-brain anatomical structures based on the image intensity and morphology of brain anatomy. Probability of activation is calculated in real-time based on the methods outlined in the thesis (See Section 7.2.2). A user might then input conditional parameters for ROI selection and zooming at each stage. Since activation may be limited to very few pixels depending on brain anatomy and the functional unit under study, different conditions in terms of size of activation and statistical significance may be used for ROI selection. For example, clusters of more than 7 adjacent pixels in volume with $p < 0.01$ for one ROI and single pixel location of $p < 0.0001$ for another ROI may be used criteria for ROI selection.

The information gathered from the initial scan session would then be used to determine the locations for further zooming and setting the optimal resolution for detection in later scan stages. RF encoding prescription would be updated interactively with user input between scan stages until the final goal of temporal or spatial resolution of the functional study is obtained. The process may be fully automated once the whole process is optimized for the given experimental setting.

We believe the adaptive approach can provide an efficient method of targeting VOI's and characterizing the selected VOI's with high spatial resolution. A goal we hope to achieve with our method is isotropic 1.5-mm spatial resolution in a functional study in well under 10 minutes.

8.7. Conclusions

In this thesis, an adaptive multi-resolution approach using spatially selective RF encoding was developed for fMRI. The basic idea of the method is to zoom into selected slice locations of interest with high temporal and/or spatial resolution. We aimed to show the adaptive multi-resolution method combined with real-time data processing and imaging prescription would add significant flexibility of functional mapping experiment. Our conclusions from this work are as follows;

- Based on numerical study described in Chapter 3, we conclude that Hadamard encoding can improve image SNR (and therefore, BOLD CNR) although a relatively large number of slices (>16) is necessary to provide significant gain over the multi-slice method. We also concluded that the possible introduction of the signal fluctuation by imperfection in spatial profile of Hadamard basis is not highly significant in terms of seriously compromising the functional detection.

- Based on the theoretical analysis described in Chapter 4, we conclude that there is an optimal spatial resolution to insure maximum detection of the functional activation.

Generally, we found that the maximum CNR is obtained when the resolution matches the size of the functional activation itself. Our analysis is based on using BOLD CNR as qualitative determinant for functional detection.

- Based on the experimental results described in Chapter 5, we confirmed the conclusions of the theoretical analysis. Again, BOLD CNR was used as the quantitative measure of functional detection, and conclude high spatial resolution is not generally desirable for the initial detection of activation, at least for the sensorimotor paradigm that we used in our studies. The optimal resolution to obtain maximum CNR is the resolution that matches the size of the functional activation itself.

- Based on the experimental results described in Chapter 5, we conclude that physiological noise increases with slice thickness. Physiological noise, as described by the analytical model in Chapter 4, can reduce the CNR significantly when lowering spatial resolution. This is true if the area affected by physiological noise is larger than the areas of functional activation.

- Based on the results described in Chapter 6 where the utility of RF encoding in fMRI was demonstrated in a conventional MR system, we conclude that the method provides a simple means of monitoring planes with variable thickness irregularly spaced throughout the brain without the need to encode whole brain.

- We further conclude from our studies described in Chapter 6 that the flexibility of RF encoding can exploited to reduce the in-flow effect by applying uniform level of saturation over the imaging volume.

- Based on the results of our implementation of a real-time interactive fMRI method as described in Chapter 7, we conclude that a multi-resolution adaptive approach can be used for detecting functional activation and result in increased temporal or/and spatial resolution.

In general, multi-resolution adaptive zooming approach based on RF encoding offers greater flexibility in designing functional MRI protocols. In addition, there is potential for increase in SNR and reduction of in-flow effect using RF encoding. More work must be directed toward the implementation of the method with EPI and toward the exploration of applications in neuroscientific studies and neurosurgical planning.

List of Symbols

Chapter 1

ΔE : Energy created by Zeeman interaction
γ : Gyromagnetic ratio
κ : Boltzmann's Constant (1.38 x 10^{-23} J/K^o)
T : Temperature (K^o)
$\hbar$: Plank's constant
B_o : Magnetic field
ω_o : Larmor resonance frequency
$\overrightarrow{M}$: Modeled bulk magnetization vector with component (M_x, M_y, M_z)
$\vec{\Gamma}$: Torque vector
$\overrightarrow{B_1}$: Magnetic field vector created by RF pulse
$\mathfrak{R}$: Relaxation matrix
$\vec{G}$: Magnetic gradient vector (Gauss/cm)
$s(t)$: Signal from a sample
$\rho(x, y)$: Signal density function within the excited sample
ΔG_y : Magnitude of gradient increment in each phase encoding step
τ : Duration of phase encoding gradient
ΔT : Sampling interval during the data acquisition during readout
TE : Time of echo
TR : Time of repetition
τ_o : Gradient reversal period in EPI
α_E : Flip angle

Chapter 2

R_2^* : Transverse relaxation rate

Chapter 3

$\Phi_m(x)$: Spatially selective basis functions
$\overline{\overline{T}}$: Set of encoding functions
$t_n(x)$: Spatially-dependent weighing factor in encoding
$\bar{s}$: Spin density estimate of the sample in vector

$\bar{y}$: Acquired signal vector
$\bar{\bar{Y}}$: Matrix whose rows we place the output signal values
$\bar{\bar{C}}$: Matrix defining basic volume element
$\bar{\bar{S}}$: Matrix whose each row vector contains the frequency or phase encoded signal value
$\bar{\bar{H}}$: Hadamard encoding matrix
$\bar{\bar{W}}$: Haar encoding matrix
$\bar{\bar{I}}$: Identity matrix
$\bar{\eta}$: Thermal noise
$\bar{\eta}'$: Noise vector after the reconstruction
$\mathcal{E}$: Expectation operator
$\bar{\bar{D}}$: Diagonal matrix
σ^2 : Noise variance
TR_eff : Effective TR period
n_{sl} : Number of slices encoded

Chapter 4

S_{off} : Signal vectors obtained during off stage of task-paradigm
S_{on} : Signal vectors obtained during on stage of task-paradigm
n : Number of samples
Z_s : Z-score
S : MR signal level
ρ : Mean baseline signal level
Δ : BOLD signal contrast
σ_η : Standard deviation of thermal noise
ε : Distribution width of Gaussian function
$TR_{\min}$: Minimum imaging time for one slice
n_{sl} : Number of slices encoded
$\Diamond_{thk}$: Slice thickness of imaging
$\Diamond_{acr}$: Thickness of BOLD activation
δ : Physiological noise
σ_{phys} : Standard deviation of physiological noise
ΔS_{act} : BOLD signal contrast
ΔS : Measured BOLD contrast

List of Figures

List of Tables

References

[1] Belliveau, J.W., Rosen, B.R., Kantor, H.L., Rzedzian, R.R., Kennedy, D.N., McKinstry, R.C., Vevea, J.M., Cohen, M.S., Pykett, I.L., and Brady, T.J., 1990, Functional cerebral imaging by susceptibility-contrast NMR. *Magn. Reson. Med.* **14:** 538-546

[2] Belliveau, J.W., Kennedy, D.N., McKinstry, R.C., Buchbinder, B.R., Weisskoff, R.M., Cohen, M.S., Vevea, J.M., Brady, T.J., and Rosen, B.R. 1991, Functional mapping of the human visual cortex by magnetic resonance imaging. *Science* **254:** 716-719

[3] K.K. Kwong, J.W. Belliveau, D.A. Chesler, I.E. Goldberg, R.M. Weisskoff, B.P. Poncelet, D.N. Kennedy, B.E. Hoppel, M.S. Cohen, R. Turner, H. Cheng, T.J. Brady, B.R. Rosen, 1992, Dynamic magnetic resonance imaging of human brain activity during primary sensory stimulation. *Proc. Natl. Acad. Sci. USA* **89,** 5675-5679

[4] Rosen B.R., Belliveau, J.W., Vevea, J.M., and Brady, T.J., 1990, Perfusion imaging with NMR contrast agents. *Mag. Res. Med.* **14**:249-265

[5] Rosen, B.R. and Brady, T.J. 1993, Future uses of MR imaging agents, *J. Comp. Assist. Tomogr.* ,**17**:S36-S42

[6] Rosen, B.R., Buckner, R.L., and Dale, A.M. 1998, Event-related functional MRI: Past, present, and future. *Proc. Natl. Acad. Sci. USA.* **95:**773-780

[7] Ogawa, S., Tank, D.W., Menon, R., Ellerman, J.M., Kim, S.G., Merkle, H., and Ugurbil, K., 1992, Intrinsic signal changes accompanying sensory stimulation: functional brain mapping using MRI. *Proc. Natl. Acad. Sci. USA.* **89:** 5951-5955

[8] Schneider, W., Noll, D.C. and Cohen, J.D. 1993, Functional topographic mapping of the cortical ribbon in human vision with conventional MRI scanners, *Nature*, **365**:150-153

[9] Nitschke, M.F., Kleinschmidt, A., Wessel, K., and Frahm, J. 1996, Somatotopic motor representation in the human anterior cerebellum, A high-resolution functional MRI study. *Brain*, **119**:1023-1029

[10] Kleinschmidt, A., Nitschke, M. F. and Frahm, J. 1997. Somatotopy in the human motor cortex hand area, A high-resolution functional MRI study, *European J of Neurosci.* **9:**2178-2186

[11] Buckner, R.L., Goodman J., Burock, M., Rotte M., Koutstaal, W., Schacter D.,Rosen, B.R., and Dale, A.M., 1998, Functional-anatomic correlates of object priming in human revealed by rapid presentation of event-related fMRI. *Neuron*, **20:**285-296

[12] Buckner R.L., Koutstaal W., Schacter D.L., Dale, A.M., Rotte M., Rosen, B.R., 1998, Functional-anatomic study of episodic retrieval, *Neuroimage*, **7**:163-175

[13] Courtney S.M., Ungerleider L.G., Keil, K., Haxby J.V., 1997, Transient and sustained activity in a distributed neural system, for human working memory. *Nature*, **386:** 608-611

[14] D'Esposito M.E., Postle, B.R., Jonides J., and Smith E.E., 1999, The neural substrate and temporal dynamics of interference effects in working memory as revealed by event-related functional MRI. *Proc. Natl., Acad., Sci. USA.,* **96**:7514-7519

[15] Henson, R.N.A., Rugg, M.D., Shallice T., Josephs, O., and Dolan R.J., 1999, Recollection and familiarity in recognition memory; An event-related functional magnetic resonance imaging study. *J of NeuroScience*, 19:3932-3972

[16] Roux F.E., Ranjeva, J.P., Boulanouar K., Manelfe C., Sabatier J., Tremoulet M., and Berry I., 1997, Motor functional MRI for presurgical evaluation of cerebral tumors. *Stereotactic and Functional Neurosurgery,* **68**:106-111

[17] Schulder, M., Maldjian, J.A., Liu, W.C., Mun, I.K., and Carmel, P.W. 1997, Functional MRI-guided surgery of intracranial tumors. *Stereotactic & Functional Neurosurgery.* **68**:98-105

[18] Sperling, R.A., Wible, C.G., Yoo, S.-S.,Guttmann, C.R.G., Panych, L.P., Johnson, K.A., Nelson, A., Kacher, D., Jakab, M., Mulkern, R., Wells, W., Chabrerie, A., Ozlen, F., Stieg, P.E., Kikinis R., and Jolesz, F.A. 1998. Integration of fMRI with intraoperative imaging techniques. *Proceedings in the 4th International Conference on Functional Mapping of the Human Brain*, Montreal, Canada. S403

[19] Kaminogo, M. Morikawa, M., Ishimaru H., Ochi M., Onizuka M., Shirakawa, Y., Takahashi H., and Shibata S.,1999, Presurgical mapping with functional MRI: Comparative study with transcranial magnetic stimulation and intraoperative mapping, *Neurological Surgery,* **27:**437-444

[20] Wible, C.G., Kubicki, M., Kricun, A., Yoo,S.-S., Kacher, D., Sailisbary, D.F., Hirayashu, Y., and McCarley, R.W, "fMRI Using the Auditory Mismatch Negativity Task in Schizophrenics" Submitted to *Biological Psychiatry*, 1999

[21] Rivkin, M.J., Vajapeyam, S., Mulkern, R.V., Weiler, M.D., Yoo, S.-S., Hutton, C. Hall, E.K., Wolff, P.H., and Waber, D.P., "fMRI on Children with Learning Disability: The Preliminary Results", in Abstract for *International Society for Neuroscience. 2000.*

[22] Gati, J.S., Menon, R.S., Ugurbil, K., and Rutt, B.K. 1997. Experimental determination of the BOLD field strength dependence in vessels and tissue. *Magn. Reson. Med.* **38:** 296-302

[23] Bandettini, P.A., Wong, E.C., Hinks, R.S., Tikofsky, R.S., and J.S. Hyde, 1992, Time course of EPI of human brain function during task activation. *Magn. Reson. Med.* **25:** 390-397

[24] Bullmore E., Brammer M., Williams SCR., Rabe-Hesketh S., Janot, N, David A., Mellers J., Robert H., Sham P.,1996, Statistical methods of estimation and inference for functional MR image analysis. *Mag. Res. Med.,* **35**:261-277

[25] Bandettini, P.A., Jesmanowicz,A., Wong,E.C., and Hyde, J.S., 1993, Processing strategies for time-course data sets in functional MRI of the human brain. *Magn. Reson. Med.* **30**: 161-173

[26] Kim, K.H.S., Relkin, N.R., Lee, K.-M., and Hirsch, J. 1997, Distinct cortical areas associated with native and second language. *Nature*, **388**:171-174

[27] Schad, L.R., Wieber, E., Baudendistel, K.T., Muller, E. and Lorenz, W.J. 1995, Event-related functional MR imaging of visual cortex stimulation at high temporal resolution using a standard 1.5T imager. *Mag. Reson. Imag.* **13**:899-901

[28] Zarahn E., Aguirre G., and D'Esposito, 1997, A trial-based experimental design for fMRI, *Neuroimage,* **6**:122-138

[29] Ernst, T. and Hennig, J., 1994, Observation of a fast response in functional MR. *Magn, Resn. Med.* **32**:146-149

[30] Cohen M.S. 1997, Parametric analysis of fMRI data using linear systems methods. *Neuroimage.* **6(2)**:93-103

[31] Glover, G.H., 1999. Deconvolution of impulse response in Event-related BOLD fMRI. *Neuroimage* **9**:416-429

[32] Allen, G., Buxton, R.B., Wong, E.C., and Courchesne, E. 1997, Attentional activation of the cerebellum independent of motor involvement. *Science* **275**:1940-1943

[33] Merboldt, K. D., Kruger, G., Hanicke, W., Kleinschmidt, A., and Frahm, J. 1995, Functional MRI of human brain activation combining high spatial and temporal resolution by a CINE FLASH technique, *Magn. Resn. Med.* **34**:639-644

[34] Frahm, J., Merboldt, K.D., and Hanicke, W. 1993, Functional MRI of human brain activation at high spatial resolution. *Magn. Reson. Med.* **29**:139-144

[35] Jesmanowicz, A.,Bandettini, P.A., and Hyde, J.S. 1998. Single-shot half k-space high resolution gradient recalled EPI for fMRI at 3 Tesla. *Magn. Reson. Med.* **40**:754-762

[36] Wildgruber, D., Erb, M., Klose, E., and Grodd, W., 1997, Sequential activation of supplementary motor area and primary motor cortex during self-paced finger movement in human evaluated by functional MRI. *Neurosc. Letters.* **227**:161-164

[37] Gao, J.-H., Xiong, J., Lai, S., Haacke, E.M., Woldorff, M.G., Li, J.,and Fox, P.T., 1996, Improving the temporal resolution of functional MR imaging using key hole techniques, *Magn, Resn, Med.* **35**:854-860

[38] Chandra S. Liang ZP. Webb A. Lee H. Morris HD. Lauterbur PC. 1996, Application of reduced-encoding imaging with generalized-series reconstruction (RIGR) in dynamic MR imaging. *J. Magn. Reson. Imag.*, 6:783-97, 1996

[39] Cao, Y. and Levin, D.N., 1993, Feature-recognizing MRI. *Magn. Reson. Med.* **30:** 305-317

[40] Panych, L.P., and Jolesz, F.A., 1994, A dynamically adaptive imaging algorithm for wavelet-encoded MRI. *Magn. Reson. Med.* **32**:738-748

[41] Panych, L.P., Oesterle C., Zientara G.P., and Hennig.J, 1996, Implementation of a fast gradient-echo SVD encoding technique for dynamic imaging. *Magn. Reson. Med.* **35**:554-562

[42] Sprawl, P., and Bronskill, M.J., "The Physics of MRI: 1992 AAPM Summer School Proceedings", American Association of Physicists in Medicine. Woodbury, NY

[43] Pauly J., Nishimura D. Macovski A., 1989, A k-space analysis of small-tip-angle excitation. *J. Magn. Reson.*,**81**:43-56

[44] Mansfield P. 1997, Multi-planer image formation using NMR spin echoes, *J. Phys. C: Solid State Physics,* **10**:L55-58

[45] Glover, G.H., Lemieux, S.K., Drangova, M., and Pauly, J.M., 1996, Decomposition of inflow and blood oxygenation level dependent (BOLD) effects with dual-echo spiral gradient-recalled echo (GRE) fMRI. *Magn. Reson. Med.* **35**:299-308

[46] Courchesne, E., Townsend, J., Akshoomoff, N.A., Saitoh, O., Yeung-Courchesne, R., Lincoln, A.J., James, H.E., Haas, R.H., Schreibman, L., and Lau, L. 1994, Impairment in shifting attention in autistic and cerebellar patients. *Behav. Neurosci.* **108**:848-865

[47] Courchesne, E., Akshoomoff, N.A., Townsend, J., and Saitoh, O., 1995, A model system for the study of attention and the cerebellum: infantile autism, *Electroencelphalogr. Clin. Neurophysiol. Suppl.* **44**:315-325

[48] Rachele M.E., 1998, Behind the scenes of functional brain imaging: A historical and physiological perspective, *Proc. Natl., Acad., Sci., USA.*, **95**:765-772

[50] Kawashima R., Roland Per. E., and O'Sullivan. B.T., 1994, Fields in human motor areas involved in preparation for reaching, actual reaching, and visucomotor learning: a positron emission tomography study. *J of Neurosci.* **14**:3462-3474

[51] Jenkins, I.H., Brooks, D.J., Nixon, P.D., Frackowiak, R.S.J., and Passingham, R.E. 1994, Motor sequence learning: a study with positron emission tomography. *J of Neurosci.* **14**: 3775-3790

[52] Hillyard, S.A., and Anllo-vento, L., 1998, Event-related brain potentials in the study of visual selective attention. Proc. Natl. Acad. Sci. USA., **95**:781-787

[53] Liu AK. Belliveau JW., and Dale AM., 1998, Spatiotemporal imaging of human brain activity using functional MRI constrained magnetoencephalography data: Monte Carlo simulations. *Proc. Natl. Acad. Sci. USA.,* **95**:8945-50

[54] Fox, P.T., and Raichle, M.E. 1986, Focal physiological uncoupling of cerebral blood flow and oxidative metabolism during somatosensory stimulation in human subjects. *Proc. Natl. Acad. Sci. USA* **83**:1140-1144

[55] Ogawa, S., Menon, R.S., Tank, D.W., Kim, S.-G, Merkle,H., Ellerman, J.M., and Ugurbil K., 1993., Functional brain mapping by blood oxygenation level-dependent contrast magnetic resonance imaging. *Biophys. J.* **64,** 803-812

[56] Menon, R.S., Ogawa, S., Hu, X., Strupp, J.P., Anderson P., and Ugurbil, K., 1995, BOLD based functional MRI at 4 Tesla includes a capillary bed contribution: Echo-Planar Imaging correlates with previous optical imaging using intrinsic signals. *Magn. Reson. Med.* **33**:453-459

[57] Siewert, B., Bly, B.M., Schlaug, G., Darby, D.G., Thangaraj, V., Warach, S., and Edelman, R.R., 1996. Comparison of the BOLD and EPISTAR technique for functional brain imaging by using signal detection theory. *Magn. Reson. Med.* **36**:249-255

[58] Haacke E.M., and T.B. Parrish, Reduction of T2* dephasing in gradient field-echo imaging, 1989, *Radiology*, **170**:457-462

[59] Kennan R.P., Zhong J., and Gore J.C., 1994, Intravascular susceptibility contrast mechanisms in tissues, *Magn. Reson. Med.* **31**:9-21

[60] Hoogenraad, F.G.C., Hofman, M.B.M., Pouwels, P.J.W., Reichenbach, J.R., Rombouts, S.A.R.B. and Haacke, E.M. 1999, Sub-millimeter fMRI at 1.5 Tesla; Correlation of high-resolution with low resolution measurement. *J. of Mag. Res. Imag.,* **9**:475-482

[61] Boxerman, J.L., Hamberg, L.M., Rosen, B.R., Weisskoff, R.M., 1995, MR contrast due to intravascular magnetic susceptibility perturbations, *Magn. Reson. Med.* **34**: 555-566

[62] Y. Yang, V.S. Mattay, D.R. Weinberger, J.A.Frank, J.H. Duyn, 1997, Localized echo-volume imaging methods for functional MRI. *J. Magn. Reson. Imaging.,* **7**:371-375

[63] Lai. S., Hopkins. L., Haacke, E.M., Li. D., Wasserman, B.A.., Buckley, P., Friedman, L., Meltzer, H.., Hedera, P., Friedland, R., 1993., Identification of vascular structures as a major source of signal contrast in high resolution 2D and 3D functional activation imaging of the motor cortex at 1.5T: preliminary results. *Magn. Reson. Med.* **30**: 387-392

[64] Weisskoff, R.M., Zuo C.S., Boxerman J.L., and Rosen B.R., 1994, Microscopic Susceptibility Variation and Transverse Relaxation: Theory and Experiment. *Magn. Reson. Med.* **31**:601-610

[65] Bandettini P.A., Wong E.C., Jesmanowicz A., Hinks R.S., and Hyde J.S., 1994, Spin-echo and Gradient echo EPI of human brain activation using BOLD contrast: a comparative study at 1.5T, *NMR in BioMed* 7:12-20

[66] Boxerman, J.L., Bandettini, P.A., Kwong, K.K., Backer J.R., Davis, T.L., Rosen B.R., and Weisskoff, R.M., 1995, The intravascular contribution to fMRI signal change: Monte Carlo modeling and diffusion-weighted studies in vivo. *Magn. Reson. Med.* **34**:4-10

[67] Constable R.T., Kennan R.P., Puce, A., McCarthy G., and Gore J.C., 1994, Functional NMR imaging using Fast Spin Echo at 1.5T. *Magn. Reson. Med.* **31:** 686-690

[68] Biswal, B., Yetkin F.Z., Haughton V.M., Hyde J.S., 1995, Functional connectivity in the motor cortex of resting human brain using EPI, *Mag. Res. Med.* **34**:537-541

[69] Kim SG. Richter W. and Ugurbil K., 1997, Limitations of temporal resolution in functional MRI. *Magn. Reson. Med.*.**37:** 631-636

[70] Buckner R.L., Bandettini, P.A., O'Craven K.M., Savoy R.L., Petersen S.E., Raichle M.E., and Rosen B.R., 1996, Detection of cortical activation during averaged single trials of a cognitive task using functional magnetic resonance imaging. *Proc. Natl. Acad. Sci. USA,* **93:** 14878-14883

[71] Duyn, J.H., Moonen, C.T., Yperen, G.H. van.Boer., and Luyten, P.R. 1994, Inflow versus deoxyhemoglobin effect in BOLD functional MRI using gradient echoes at 1.5 T. *NMR Biomed.* **7:** 83-88

[72] Duyn, J.H., Mattay, V.S., Sexton, R.H., Sobering, G.S., Barrios, F.A., Liu, G., Frank, J.A., Weinberger, D.R., and Moonen, C.T., 1994, 3-dimensional functional imaging of human brain using echo-shifted FLASH MRI. *Magn. Reson. Med.* **32,** 150-155

[73] van Gelderen, P., Ramsey, N.F., Liu, G., Duyn, J.H., Frank, J.A., Weinberger, D.R., and Moonen, C.T., 1995., Three-dimensional functional magnetic resonance imaging of human brain on a clinical 1.5-T scanner. *Proc. Natl. Acad. Sci.USA.,* **92:**6906-6910

[74] Cox, R.W., Jesmanowicz, A., and Hyde, J.S. 1995, Real-time functional magnetic resonance imaging. *Magn. Reson. Med.* **33:** 230-236

[75] Talairach, J. and Tournoux, P., 1998, "Co-planar stereotaxis atlas of the human brain", Thieme Medical, N.Y.

[76] Friston, K.J, Holmes, A., Poline, J.B., Price, C.J., and Frith, C.D., 1996, Detecting activations in PET and fMRI: Levels of interference and power. *Neuroimage* 4, 223-235

[77] Weisskoff, R.M., Baker, J., Belliveau, J., Davis, T.L., Kwong, KK., Cohen, M.S. and Rosen, B.R. 1996, Power spectrum analysis of Functionally weighted MR data: What's in the Noise?, ISMRM conference P7

[78] Baker, J.R., 1997, HST Thesis: physiological fluctuations in functional magnetic resonance imaging signals

[79] Wu, D.H., Lewin, J.S., and Duerk, J.L. 1997, Inadequacy of motion correction algorithms in functional MRI: role of susceptibility-induced artifacts. *J of Magn. Reson. Imag.* **7**:365-370

[80] Lee, C.C. Jack, C.R.,Jr., Grimm, R.C., Rossman, P.J., Felmlee, J.P., Ehman, R.L., and Riederer. S.J., 1996, Real-time adaptive motion correction in functional MRI. *Magn. Reson. Med.* **36**:436-444

[81] Hu, X., and Kim, S.-G., 1994, Reduction of signal fluctuation in functional MRI using navigator echoes. *Mag. Res. Med.* **32**:495-503

[82] Hu, X. Le. T.H., Parrish T., and Erhard, P., 1995, Retrospective estimation and correction of physiological fluctuation in functional MRI, *Mag. Res. Med.* **34**:201-212

[83] Biswal. B., DeYoe E.A., and Hyde, J.S., 1996, Reduction of physiological fluctuations in fMRI using digital filters. *Magn. Resn. Med* **35**:107-113

[84] Loenneker, T., Hennel, F., and Hennig, J., 1996, Multislice Interleaved Excitation Cycles (MUSIC): An efficient gradient-echo technique for functional MRI. *Magn. Reson. Med.* **35**: 870-874

[85] Liu G., Sobering G., Duyn J., and Moonen C.T., 1993, A functional MRI technique combining principles of echo-shifting with a train of observations (PRESTO). *Magn. Reson. Med.* **30**:764-768

[86] Mansfield, P., Coxon, R., and Hykin, J., 1995, Echo-volumar imaging (EVI) of the brain at 3.0 T: first normal volunteer and functional imaging results. *J. of Comp. Assit. Tomogr.*. **19**: 847-852

[87] Boynton, G.M., Engel, S.A., Glover G.H., Heeger D.J., 1996, Linear systems analysis of functional magnetic resonance imaging in human V1, *J. of Neuroscience*, **16**:4207-4221

[88] Buckner R.L., 1998, Event-related fMRI and the hemodynamic response, *Human Brain Mapping*, **6**:373-377

[89] Fransson O., Kruger G., Merboldt, K.D., Frahm J., 1998, Physiological aspects of event related paradigms in magnetic resonance functional neuroimaging. *Neuroreport* **9**:2001-2005

[90] Jessen F., Erb, M., Klose, U., Lotze, M., Grodd, W., and Heun R., 1999, Activation of human language processing brain regions after the presentation of random letter strings demonstrated with event-related functional magnetic resonance imaging. *NeuroScie. Lett.*, **270**:13-16

[91] Friston K.J., Josephs, O., Rees G., Turner R., 1998, Nonlinear event-related responses in fMRI. *Mag. Res. Med.* **39**:41-52

[92] Burock M.A., Buckner R.L., Woldorff M.G., Rosen B.R., and Dale A.M. 1998, Randomized event-related experimental designs allow for extremely rapid presentation rates using functional MRI, *Neuroreport,* **9**:3755-3739

[93] Panych, L.P., Zientara, G.P., Saiviroonporn, P. Yoo, S.-S., and Jolesz, F.A. 1998. Digital wavelet-encoded MRI: a new wavelet-encoding methodology. *J of Magn. Reson. Imag.* **8**:1135-44

[94] Hoult, D.I., 1979, The solution of the Bloch equations in the presence of a varying B1 field - An approach to selective pulse analysis. *J. Mag. Reson.* **35,** 69-86

[95] Ailion, D.C., Ganesan, K., Case, A., and Christman, R.A., 1992, Rapid line scan technique for artifact-free images of moving object. *Magn. Reson. Med.* **10**:747-754

[96] Gudbjartsson, H., Maier, S.E., Mulkern, R.V., Morocz, I.A., Patz, S., and Jolesz, F.A., 1996, Line scan diffusion imaging. *Magn. Reson. Med.* **36**:509-519

[97] Morris, G.A. and Freeman, R., 1978, Slice selection in Fourier transform nuclear magnetic resonance. *J. Mag. Reson.* **29,** 433-462

[98] Heid, O., 1995, Fourier spliced pencil imaging, *in* "Proc. ISMRM, 3th Meeting, Nice, 1995" p. 488.

[99] Panych, L.P., 1996, Theoretical comparison of Fourier and wavelet encoding in magnetic resonance imaging. *IEEE Trans. Med. Imag.* **15**:141-153

[100] Hendrick, R.E., and Ulrick, R., "Image contrast and noise in magnetic resonance imaging, Second Ed." (D.D. Start, W.G. Bradley, Eds.), p 109-144, Mosby Year Book, 1992.

[101] Spiegel, M.R., "Theory and Problems of Probability and Statistics: Schaums' Outline Series", McGraw-Hill Book Co. New York, NY

[102] Butts, K., Riederer, S.J., Ehman, R.L., Thompson, R.M., and Jack, C.R. 1994, Interleaved echo planar imaging on a standard MRI system. *Magn. Reson. Med.* **31**:67-72

[103] Gudbjartsson, H. and Patz, S. 1995, The Rician distribution of noisy MRI data, *Magn. Reson. Med.* **34**:910-914

[104] Kyriakos, W.E., and Panych, L.P., 1990, Implementation of wavelet encoded MRI with large flip-angle RF pulses, *in* "Proc. SMRM, 11th Meeting, Vancouver, 1997," p. 1990.

[105] DeYoe, E.A., Neitz, J., Bandettini, P.A., Wong, E.C., and Hyde, J.S., 1992, Time course of event-related MR signal enhancement in visual and motor cortex, *in* "Proc. SMRM, 11th Meeting, Berlin, 1992," p. 1824.

[106] Locascico J.J., Jennings, P.J., Moore C.I., Corkin, S., 1997, Time series analysis in the time domain and resampling methods for studies of functional magnetic resonance brain imaging, *Human Brain Mapping*, **5**:168-193

[107] Gonen, O., Hu, J., Stoyanova, R., Leigh, J.S., and Goelman, G. 1995, Hybrid three dimensional (1D-Hadamard, 2D-Chemical Shift Imaging) phosphorus localized spectroscopy of phantom and human Brain. *Magn. Reson. Med.* **33**:300-308

[108] Yoo, S.-S., Guttmann, C.R.G., and Panych, L.P. "Feasibility of real-time event-related functional MRI" in *Proc. Intl. Soc. Magn. Reson. Med. 2000.*

[109] Kreis, R. 1997, Quantitative localized 1H-MMR spectroscopy for clinical use. *Prog. NMR Spectroscopy.* **32**:155-195

[110] Panych, L.P., Yoo, S.-S., and Zientara, G. "Real-time detrending of physiological noise from fMRI data" in *Proc. Intl. Soc. Magn. Reson. Med. 2000.*

[111] Yang, Q.X., Williams, G.D., Demeure, R.J., Mosher, T.J., and Smith, M.B., 1998, Removal of local field gradient artifacts in T2*-weighted images at high fields by gradient-echo slice excitation profile imaging. *Magn. Reson. Med.* **39**:402-409

[112] Yang, Q.X., Demeure, R.J., and Smith, M.B., 1999, Rapid whole-brain T2* echo planar imaging with removal of magnetic susceptibility artifacts. *Proc. of the ISMRM,* p537

[113] Abragam, A., 1961, "Principles of nuclear magnetism" *in International Series of Monographs on physics*, Oxford University Press, Oxford, UK.